Carbon Nanotube Based Stationary X-ray Tomosynthesis Scanner for Detection of Breast Cancer

Guang Yang

A dissertation submitted to the faculty of the University of North Carolina at Chapel Hill in partial fulfillment of the requirements for the degree of Doctor of Philosophy in the Department of Physics and Astronomy.

Chapel Hill
2008

Approved by

Advisor: Professor Otto Zhou

Committee: Professor Thomas B. Clegg

Committee: Professor David S. Lalush

Committee: Professor Jianping Lu

Committee: Professor Lu-Chang Qin

Abstract

Guang Yang

Carbon Nanotube Based Stationary X-ray Tomosynthesis Scanner
for Detection of Breast Cancer

(Under the direction of Professor Otto Zhou)

In this dissertation, my Ph.D. research during the past six years will be presented. My research mainly focused on design, fabrication and characterization of devices based on carbon nanotubes (CNT). Since the discovery of CNT in 1991, the research focus has gradually shifted from material synthesis and characterization to devices and applications. During early stages of my Ph.D. study, I worked on synthesizing CNT using laser ablation method, and fabricating CNT-AFM tips and magnetic wire MFM tips. During the second half of my Ph.D. study, my research focused more on design, fabrication, and testing the x-ray sources and imaging systems based on CNT, including both single-beam system (microCT) and multi-beam system (tomosysthesis). During the last two years, I worked on the project to develop a novel imaging system (Argus) using CNT x-ray source array for breast cancer detection. This is the first stationary digital breast tomosynthesis (DBT) imaging system in the world. My research result has shown great clinical potentials of these imaging systems using x-ray source based on CNTs.

This dissertation is composed by five chapters. In chapter one, the physics behind x-ray and field emission theory will be reviewed. Chapter two covers discovery, property and synthesis of CNT. Methods to fabricate CNT emitters and their emission property will also be introduced there. Single and multi beam x-ray sources and applications will be discussed in chapter three. The design and characteristic test results are presented. The application includes micro-CT, tomosynthesis and multiplexing. Chapter four is dedicated to the Argus system, the first stationary digital breast tomosynthesis imaging system. At last, conclusion is given in chapter five.

To my parents

Xiulan, and Hongbin

Acknowledgements

I am indebted to many people with whom I had the honor of working and without whom the completion of this dissertation would have been much more difficult. Dr. Otto Zhou's expertise and encouragement are always dependable during my entire doctoral study. I must also acknowledge to all of my committee members for their advice and guidance: Drs. Jianping Lu, David Lalush, Lu-Chang Qin, and Thomas Clegg.

I want to thank all my colleagues I have been working with. Dr. Jian Zhang passed me hands-on experience in system design and test. Ramya Rajaram has taken charge of the imaging reconstruction of all the systems I have worked on. Dr. Guohua Cao, Matthew McIntosh, Shabana Sultana, Tuyen Phan, Zhijun Liu are also key contributors for the tomosynthesis project. Colleagues I have been working with for other projects include Dr. Jie Tang, Dr. Huaizhi Geng, Dr. Lei An, Dr. Peng Wang, Dr. Yueh Lee, Rui Peng, David Bordelon, Xiomara Calderon, Christy Redmon, Dr. Yuan Cheng, Dr. Bo Gao, Qi Qiu. It has been a great honor for me to work with them during the past six years.

At last, I recognize that this research would not have been possible without the support from the following organizations: National Cancer Institute, NASA, Xintek, and the Office of Naval Research.

Table of contents

List of figures

List of tables

Chapter 1: Introduction and Background

1.1 Discovery of X-ray

X-ray was first discovered by William Roentgen (1845-1923), a physicist at Julius Maximilian University of Würzburg in Germany, on November 8, 1895. Roentgen was testing cathode rays[1] to see if they would pass through glass when he noticed a glow emanating from a chemically coated screen lying a few feet away. Roentgen named the unknown rays "x-ray" for he did not know what they were or where they came from. After immense work on it, Roentgen found out that x-ray could penetrate some substance but not others such as the bones. Roentgen was the first person to take an x-ray image, the hand of his wife (Figure 1-1). He did not patent his invention, so it was freely available to anyone who could use it and soon become valuable in scientific, medical and technical fields. In 1991, William Roentgen won Nobel Price for physics due to his pioneer work on x-ray.

Figure 1-1: The first x-ray image.

Bertha Roentgen's hand, the first x-ray image taken by human in 1895. Picture source: http://www.nlm.nih.gov/exhibition/dreamanatomy/da_g_Z-1.html

The discovery of x-ray attracted a lot of attention soon after for its great application potential. More than one hundred years later, x-ray technology has become a valuable tool in science, engineering and everyday life. In physics and chemistry studies, x-ray diffraction pattern can reveal the secret atomic structure of materials[2]; in astrophysics and cosmology, x-ray telescope captures the remote radiation residue from the very early stage of the universe[3]; in industry, x-ray detection is widely used to examine the crack and leakage; in medical physics, x-ray imaging technology is applied in area such as full body computed tomography and mammography[4]. In Figure 1-2, several typical applications are shown.

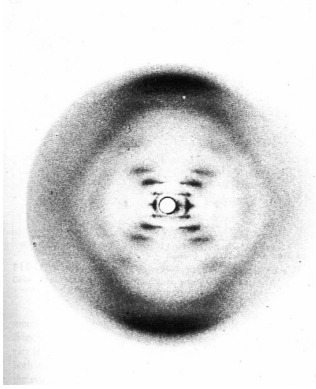

(a)

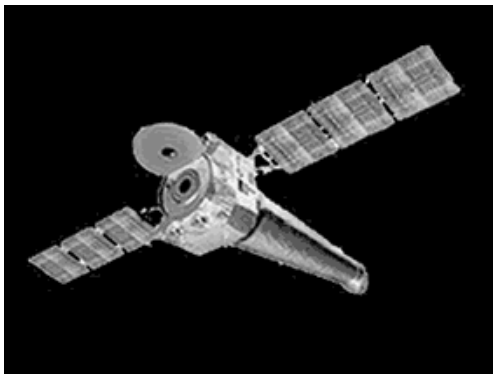

(b)

(c)

(d)

Figure 1-2: Applications of x-ray.

(a): The x-ray diffraction pattern of DNA by R. Franklin in the laboratory of M. Wilkins. Picture source: reference [5]. (b): Chandra X-Ray Observatory. This telescope is NASA's flagship mission for X-ray astronomy. Professor Lang uses Chandra in combination with radio telescopes to observe the Galactic Center. http://www.physics.uiowa.edu/graduate/images/chandra_280.gif. (c): X-ray airport screening machine. http://www.cdc.gov/niosh/topics/airportscreener/images/topicimg1.gif. (d): Commercial mammography machine (model MGU 100D) from Toshiba Medical. http://www.toshiba-medical.co.jp/.

1.2 Basics of X-ray Radiation

X-ray is fundamentally electromagnetic radiation. The basic properties are the same as visible light, ultraviolet, infrared and other similar types of radiant energy. The common electromagnetic spectrum is listed in Table 1-1. The energy of x-ray normally ranges from 10^2 to 10^6 eV. The nearby radiation with lower energy is ultraviolet, while the one with

higher energy is gamma ray. Due to the energy range of x-ray radiation, normally it arises when a stream of fast-moving electrons suddenly undergoes a reduction in speed (or experiences acceleration). A typical x-ray spectrum from a commercial x-ray tube is shown in Figure 1-3. As illustrated, there are two kinds of radiation in the spectrum: Bremssstrahlung radiation (background) and characteristic radiation (peaks).

Table 1-1: Electromagnetic wave spectrum.

Source: reference [1].

Electromagnetic wave spectrum

Energy (eV)	Frequency (Hz)		Wavelength (m)
4×10^{-11}	10^{4}		10^{4}
4×10^{-10}	10^{5}	AM radio waves	10^{3}
4×10^{-9}	10^{6}		10^{2}
4×10^{-8}	10^{7}	Short radio waves	10^{1}
		FM radio waves and TV	
4×10^{-7}	10^{8}		10^{0}
4×10^{-6}	10^{9}		10^{-1}
4×10^{-5}	10^{10}	Microwaves and radar	10^{-2}
4×10^{-4}	10^{11}		10^{-3}
4×10^{-3}	10^{12}	Infrared light	10^{-4}
4×10^{-2}	10^{13}		10^{-5}
4×10^{-1}	10^{14}	Visible light	10^{-6}
4×10^{0}	10^{15}	Ultraviolet light	10^{-7}
4×10^{1}	10^{16}		10^{-8}
4×10^{2}	10^{17}		10^{-9}
4×10^{3}	10^{18}	X-ray	10^{-10}
4×10^{4}	10^{19}		10^{-11}
4×10^{5}	10^{20}		10^{-12}
4×10^{6}	10^{21}	Gamma ray	10^{-13}
4×10^{7}	10^{22}	Cosmic ray	10^{-14}

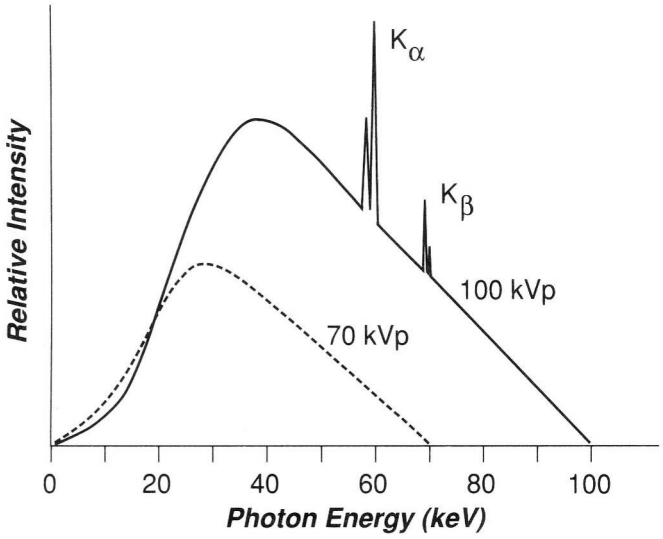

Figure 1-3: Typical x-ray spectrum of a tungsten-target tube.

At 100 kVp anode voltage, the characteristic peak is more visible. Picture source: reference [6].

1.2.1 The Bremsstrahlung Radiation

Figure 1-4 shows the schematic of the Bremsstrahlung radiation. When a fast-moving electron approaches a positive nuclear field of an atom, the electron is deviated from its original path due to the electromagnetic force. The electron is decelerated during the process, so it loses part of its kinetic energy which becomes the output energy of x-ray radiation. The Bremsstrahlung radiation is heterogeneous; in other words, it is non-uniform in energy and wavelength because the amount of deceleration varies among electrons. It composes the smooth radiation in a typical x-ray radiation.

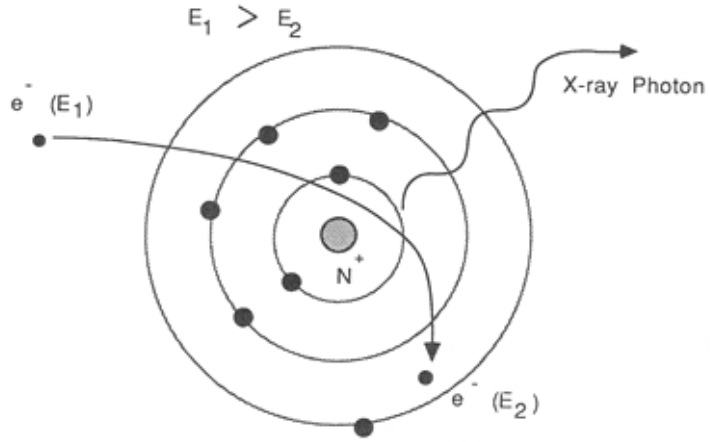

Figure 1-4: Schematic of Bremsstrahlung radiation.

The incident high energy electron experiences severe deceleration when it approaches the nucleus. The energy lost is transformed into Bremsstrahlung x-ray radiation. Picture source: reference [1].

1.2.2 The Characteristic Radiation

There is possibility that a fast-moving electron interacts with an inner orbital electron. If the energy of the incident electron is higher than the binding energy of the orbital electron, the orbital electron can be ejected to be a free electron as shown in Figure 1-5. Within 10^{-8} second, the vacancy is filled by an electron from outer orbits. In such a case, characteristic radiation is produced. The energy values of the characteristic radiation are predetermined by the atomic structures, and can be calculated by modern quantum mechanics. In the x-ray spectrum, they show as sharp peaks. Some of the characteristic x-ray energies for tungsten and molybdenum are listed in Table 1-2. Particularly in diagnostic range, characteristic

radiation constitutes 30 percent of total emission while the Bremsstrahlung radiation contributes 70 percent[7].

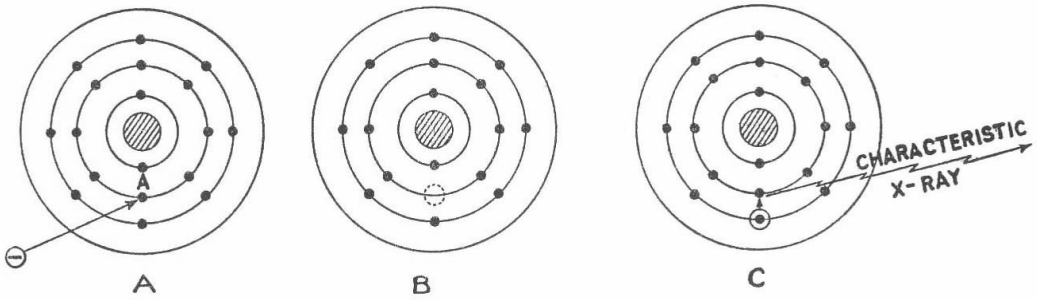

Figure 1-5: The production of characteristic x-ray.

In A, high energy incident electron collides with inner-shell electron. In B, a "hold" has been formed. In C, an out-shell electron fills in the "hold", which produces the characteristic x-ray. Picture source: reference [7].

Table 1-2: Characteristic energy values for tungsten and molybdenum.

Source: reference [1].

Tungsten (W)		Molybdenum (Mo)	
Line	*Energy (keV)*	*Line*	*Energy (keV)*
$K\beta_2$	69.081	$K\beta_{31}$	19.602
$K\beta_1$	67.244	$K\alpha_1$	17.479
$K\beta_3$	66.950	$K\alpha_2$	17.375
$K\alpha_1$	59.321		
$K\alpha_2$	57.984		

1.3 The Production of X-ray

As discussed in previous section, two components are required to generate x-ray radiation: a source of charged particles (normally electrons) and a means of accelerating or decelerating them[8]. The first man-made x-ray radiation was generated by apply a high

voltage across a cathode ray tube. This is still the fundamental technology of most modern x-ray tubes, although they are more functional and dedicated. Other methods to generate x-ray radiation, such as synchrotron x-ray source, have also been built recently. They show variety of advantages, however, they only contribute a small portion to x-ray applications due to the engineering difficulties.

1.3.1 The Conventional X-ray Tubes

The conventional x-ray tube is by far the most widely available x-ray source. The basic diagram is shown in Figure 1-6. The whole thing is sealed inside a glass tube under high vacuum. The filament is heated to over 1000˚C to produce electrons. This is so-called thermionic emission, and the mechanism will be discussed later. High voltage is applied on the stationary anode, while the heat is conducted away from the target into the massive copper block. A focusing cup is often included in many commercial x-ray tubes. The anode surface and the stream of electrons are not perpendicular. The anode is normally tilted 6 to 20 degrees, known as anode or target angle. When electrons bombard the anode, x-ray radiation is generated. Control and cooling components are also built-in for most commercial x-ray tubes.

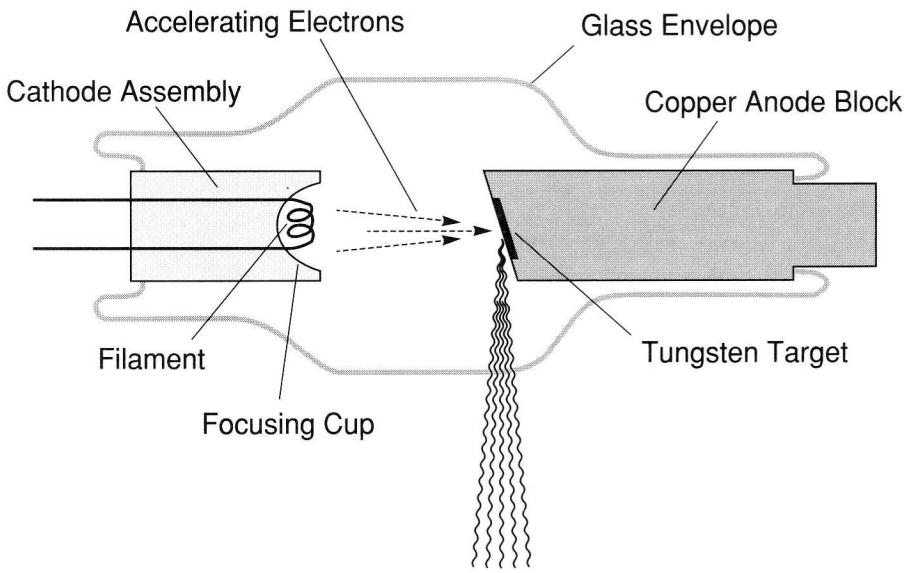

Figure 1-6: Stationary anode diagnostic x-ray tube.

Picture source: reference [6].

1.3.2 The Heel Effect

As illustrated in Figure 1-6, the x-ray radiation is predominantly in the direction about perpendicular to the electron projection[6]. A more detailed intensity distribution is shown in Figure 1-7. The x-ray beams closer to the direction of the anode have to travel longer inside the target, so are absorbed more. This phenomenon is also called “heel effect”. This effect is important in the design of the anode. A thick target perpendicular to the electron beam would absorb most of the x-ray photons; while large tilt angle gives bigger effective focal spot size (to be discussed in next section).

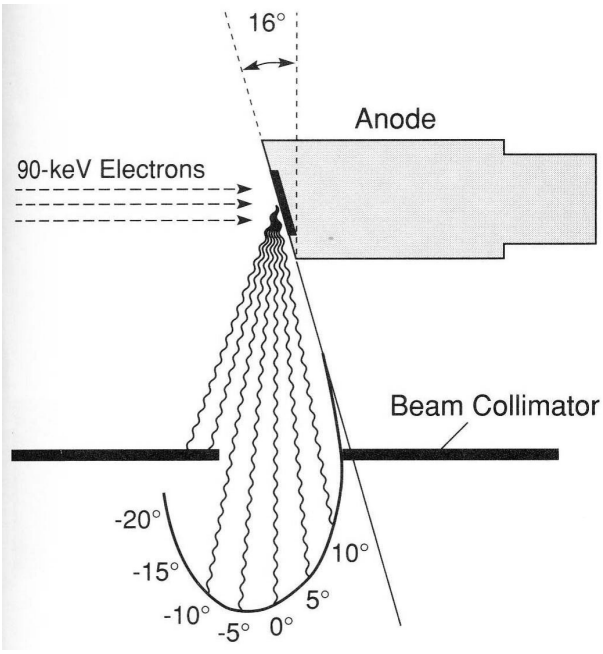

Figure 1-7: Schematic of heel effect.

Polar diagram of x-ray intensity as a function of emission angle, where the zero-degree direction is perpendicular to the incident electron stream. For 16-degree tilted angle, the maximum intensity is emitted at about -5 degrees. Picture source: reference [6].

1.3.3 The Effective Focal Spot Size

Due to the tilted angle, if all electrons are constrained inside a square area, the apparent or effective focal spot is rectangular as illustrated in Figure 1-8 (a). One benefit is that along one direction the effective focal spot size is much smaller (factor of $\tan\theta$, where θ is the tilted angle) than the original electron stream. So, if the electron stream is confined as a vertical line, as in Figure 1-8 (b), a square effective focal spot can be obtained. This is also called line focusing, a common technique applied in many designs of x-ray tubes[6, 9].

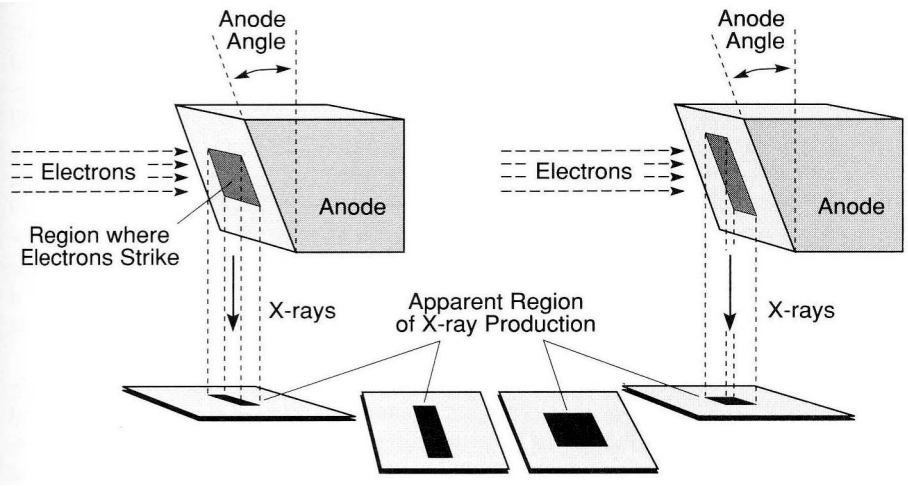

Figure 1-8: Line focusing effect.

(a): Square electron source produces rectangular apparent x-ray focal spot. (b): To obtain square apparent x-ray, the electrons should be constrained to an area long and narrow. Picture source: reference [6].

1.3.4 The Low Efficiency of X-ray Production

When electrons inside the x-ray tube collide with the anode, the kinetic energy is transformed into forms of energy including x-ray radiation. For an x-ray tube working at constant voltage *kVp* and current *mA*, the total power consumption of the x-ray tube is:

$$power = kVp \cdot mA$$

Equation 1-1

However, normally more than 99% of the power is converted into heat on the anode. For the strength of the electromagnetic interaction between an incoming electron and the nucleus is proportional to the charge of the nucleus, the efficiency should be proportional to the atomic number Z of the anode material[6]. The empirical result is:

$$efficiency = 10^{-6} Z \cdot kVp$$ **Equation 1-2**

This relation can also be calculated by quantum mechanics. This is one important reason why most commercial x-ray tubes use tungsten or other high Z value materials as anodes. The large amount of heat is one of the challenges in designing high power x-ray tubes.

1.3.5 Transmission Targets

Besides the normal tilted solid target, transmission target[10] has also been studied. The transmission targets are normally made of two layers: the base layer and the top layer. The base layer is either material with high heat conductivity, such as graphite and copper, or low Z material, such as aluminum. The thickness of the base layer is usually several hundred micron meters. The function of base layer is to support the top layer and at the same time to conduct the heat away. In the advanced design, cooling fluid can also be capsuled inside the base layer. The top layer, or the characteristic layer, is used to generate the desired characteristic x-ray and is in micron meter range in thickness. Without the tilted angle, the line focusing does not apply here. Due to the small volume, the heat dissipating rate is also lower than reflection target. These two factors limit the maximum x-ray power of the tubes using transmission targets. However, the transmission targets are more suitable for x-ray source array designs.

1.3.6 Synchrotron X-ray Source

With the development of high energy physics, a new type of x-ray source, synchrotron x-ray, became available. As discussed early in this chapter, when charged particles experiences deceleration or acceleration (either moving in a circle or straight line), x-ray radiation is generated. As illustrated in Figure 1-9, if the speed of charged particles is close to the speed of light, the emitted radiation is confined in a small angle[11].

Compared to traditional x-ray source, synchrotron x-ray source has many advantages[12, 13]:

- Small angle distribution.
- Super high brightness: about hundreds of thousands times higher than conventional x-ray tubes.
- Pulsed x-ray radiation: x-ray with desired temporal structure can be generated.
- High spatial resolution: can be as small as sub-micron meter or even nanometer.
- Large energy range: the radiation covers a wide range of energy.
- Tunable parameters: when used with mono-chromator, the output x-ray can be confined in a small range around desired energy.

The advent of synchrotron radiation has opened up comprehensive opportunities for the science and technology. However, the generation of synchrotron x-ray needs high energy physics facility to accelerate the electrons. The high cost and low availability limit the feasibility of synchrotron x-ray for general applications.

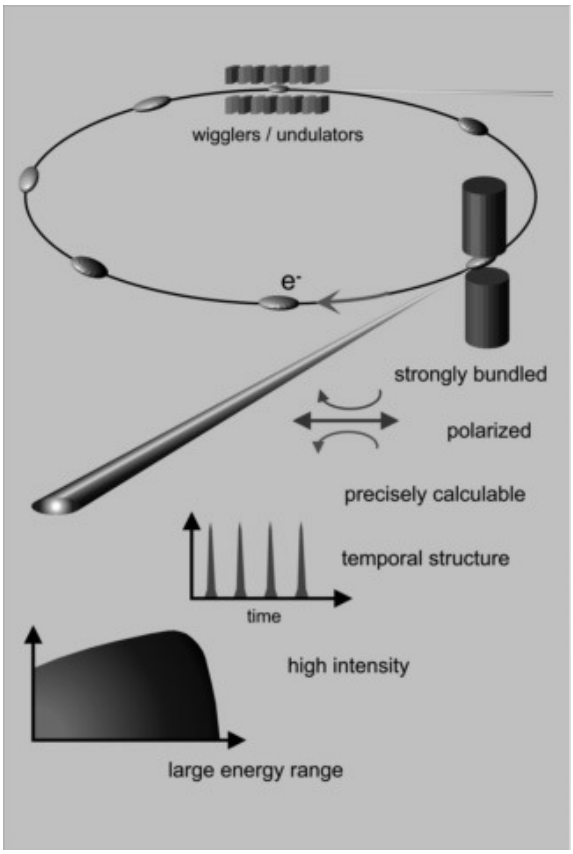

Figure 1-9: Schematics of generation of synchrotron x-ray radiation and its properties.
Picture source: http://www.bessy.de/guided_tour/en.02.sr.php?docs=2

1.4 The Interaction of X-ray with Matter

There are many ways by which x-ray or electromagnetic radiation in general can interact with matter. Depending on the energy of incoming radiation and the physical properties of the matter, some interactions are much more dominant than others[1, 6]. For x-ray photons with-in diagnostic energy (typically tens of keV to hundreds of keV), two kinds of interactions are of the most interest: photoelectric effect and Compton scattering. Other types of event mainly occur either at lower energy range such as coherent or at higher energy range such as pair production and photodisintegration.

1.4.1 The Photoelectric Effect

The schematic of photoelectric effect is shown in Figure 1-10. In this event, the energy hf_{in} of the incident photon interacting with the electron must exceed the value of its binding energy E_b. Part of the energy is expended in overcoming the binding energy of the electron to its atom, while the rest becomes the kinetic energy of the outcome photoelectron.

$$hf_{in} = E_b + KE_e$$ **Equation 1-3**

In diagnostic radiology, most interactions between x-ray photons and bones, and between x-ray photons and the image receptor, are by means of the photoelectric effect.

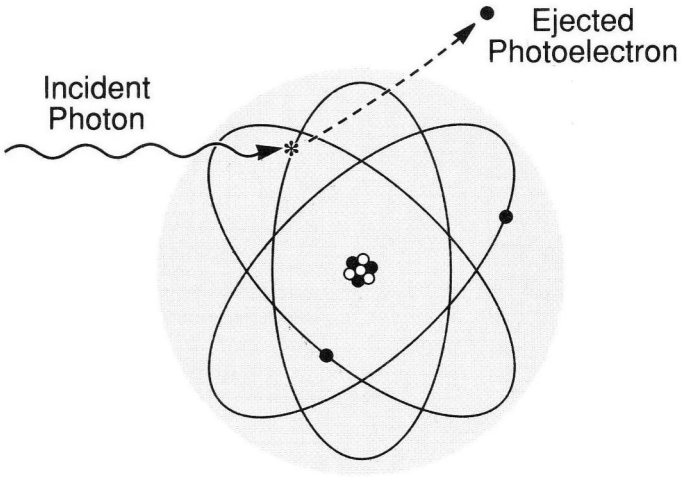

Figure 1-10: Schematic of photoelectric event.

All energy of the incident photon is transferred to the ejected photoelectron. Picture source: reference [6].

1.4.2 The Compton Scattering

Within diagnostic energy, the Compton scattering is the most dominant interaction. Both the photoelectric effect and Compton scattering come from the interaction between the incident x-ray and the orbital electron. In the latter case, however, part of the energy is taken away by the lower energy scatter photon as illustrated in Figure 1-11. Compton scattering tends to occur between higher-energy photons and atoms with relatively weakly bound electrons. The binding energy may be ignored in most calculations. Conservation of energy can be expressed as:

$$hf_{in} = hf_{scat} + KE_e$$

Equation 1-4

Most interactions between diagnostic x-ray photons and soft tissue are Compton events. This often represents noise on the x-ray images and degrades the overall image quality. Some special techniques, such as anti-scattering grid, have been developed to reduce the side effect of Compton scattering.

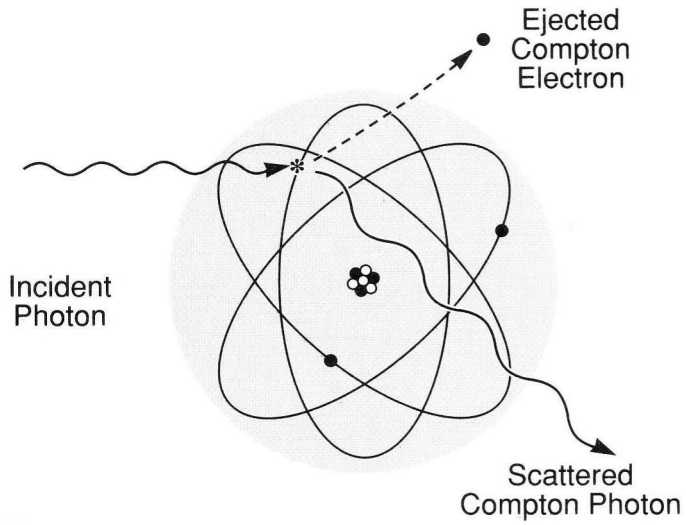

Figure 1-11: Schematic of Compton scattering.

Part of the energy of the incident photon is expended to free the electron, while the rest becomes the energy of scattered Compton photon. Picture source: reference [6].

1.5 The Attenuation Coefficients

Due to the various interactions between x-ray photons and matter, some of the x-ray radiation is absorbed when passing through a body of matter, as illustrated in Figure 1-12. In other words, the x-ray is "attenuated". The lost of the radiation is proportional to the incoming value for a thin layer. The constant of proportionality, denoted μ, is called the linear attenuation coefficient:

$$\Delta n = -\mu \cdot n \cdot \Delta x$$

Equation 1-5

After integration, the expression becomes:

$$I = I_0 e^{-\mu x}$$

Equation 1-6

where I is the outcome energy which is proportional to x-ray photon number n, and I_0 is the incident radiation energy.

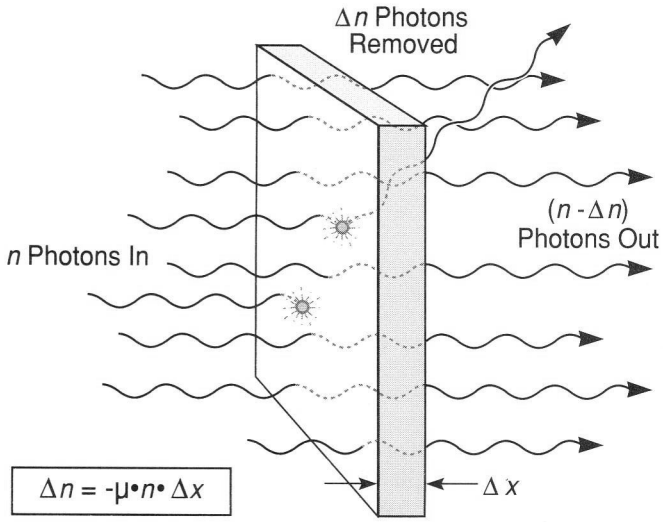

Figure 1-12: Absorption of x-ray.

n photons incident on a slab of material of thickness Δx. The absorbed and scattered photons, Δn, are proportional to n and Δx. Picture source: reference [6].

The attenuation coefficient is a function of photon energy, material type, and material density. In Figure 1-13, the coefficients for lung, muscle, bone, aluminum and lead are shown. Lung and muscle are almost identical in chemical composition. The threefold difference is due to the three time difference in density. The coefficients tend to increase with effective atomic number. Lead is a common material for x-ray radiation shielding.

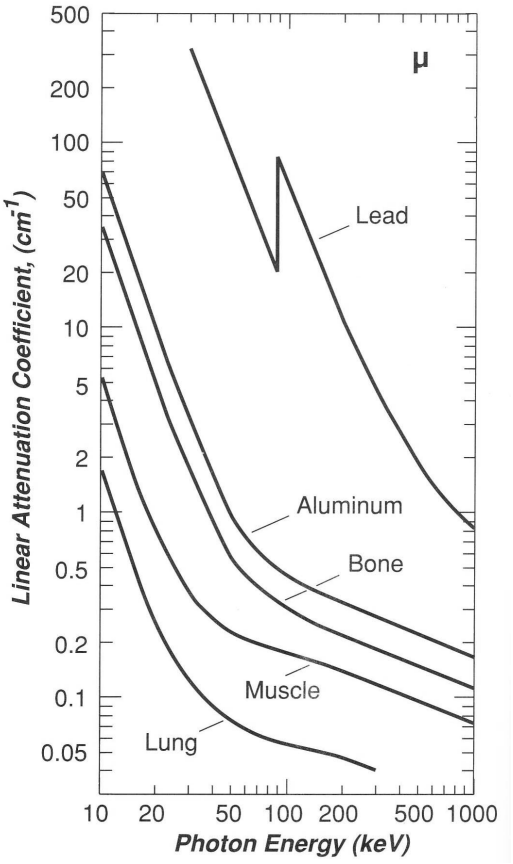

Figure 1-13: Attenuation coefficients for several materials.

Picture source: reference [6].

As discussed in previous session, two interactions, photoelectric effect and Compton scattering, contribute to the majority of adsorption in diagnostic energy range. The attenuation coefficient can also be separated into two parts:

$$\mu = \tau + \sigma$$

Equation 1-7

where τ and σ are the attenuation coefficients for the photoelectric effect and Compton scattering, respectively. τ and σ are functions of the density of the material and the photon energy:

$$\tau = \rho \cdot Z^3 \cdot E^{-3}$$ **Equation 1-8**

$$\sigma = \rho \cdot \rho_e \cdot E^{-1}$$ **Equation 1-9**

where ρ is the density, Z is the atomic number, E is the photon energy and ρ_e is the electron density of the material[6].

The linear attenuation coefficient is proportional to the density. It is convenient to define another mass attenuation coefficient, which is a constant of the material:

$$\mu / \rho = \tau / \rho + \sigma / \rho$$ **Equation 1-10**

The mass attenuation coefficients of soft tissue and lead are show in Figure 1-14.

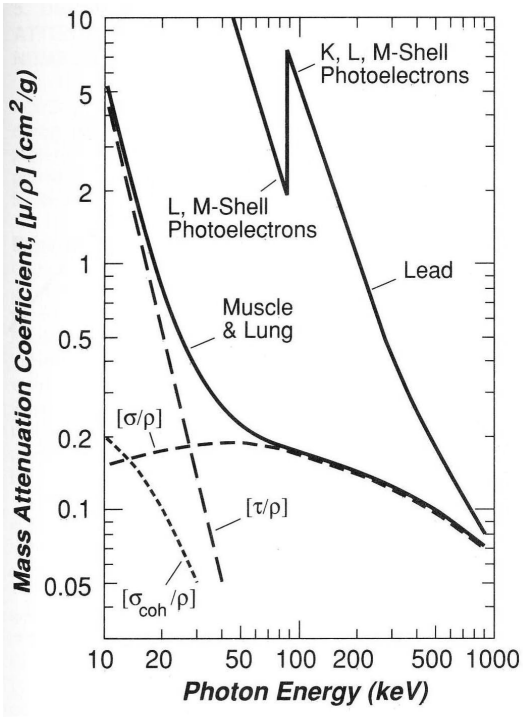

Figure 1-14: Mass attenuation coefficient of soft tissue and lead.

For muscle and lung, the coefficient is made of two parts: the photoelectric and the Compton scattering attenuation components. Other contributions, such as the coherent scattering term, are relatively small. Picture source: reference [6].

All of the above discussions are based on monochromatic x-ray radiation. In the real cases, x-ray radiation is mostly heterogeneous. The attenuation coefficient depends on the incident photon energy, and decreases as the energy increases. At a result, when a heterogeneous x-ray beam passes through a body of material, low energy photons are absorbed more. The transmitted x-ray contains more high energy photons. This is so-called "beam hardening" effect.

1.6 The Detection of X-ray

After an x-ray beam passes through a body of interest, there is still remaining radiation depending on the thickness of the body. The output x-ray contains useful information and need to be detected before further analyses. There are several ways [7] to detect x-ray, though may not measure it.

1. Photographic Effect: x-ray can affect a photographic emulsion so that it can be developed chemically.

2. Fluorescent Effect: x-ray can cause certain materials to glow in the dark, including zinc cadmium sulfide and calcium tungstate.

3. Ionizing Effect: x-ray can ionize gases and discharge certain electrical instruments such as the electroscope.

4. Physiologic Effect: x-ray can redden the skin, destroy tissues, and cause genetic damage.

5. Chemical Effect: x-ray can change the color of certain dyes.

Glass photographic plates coated with an emulsion sensitive to light were the main method to record x-ray images. Nowadays, modern x-ray films have become the dominant method for diagnostic x-ray detection. This technique has many advantages, such as low cost and high spatial resolution. X-ray films are composed of the base and the emulsion. There are three main types of x-ray films in medical radiography: screen film, direct-exposure film, and mammography film, while screen film is the most popular one.

In recent years, with the development of micro fabrication and high speed computers, the digital x-ray detectors became available. Compared to the old techniques, digital detectors have these advantages:

- Easier to store and transfer images;
- Lower noise;
- Wider dynamic range;
- Easier post-imaging analysis.

Several commercially available types[14] of digital x-ray detector are shown in Figure 1-15.

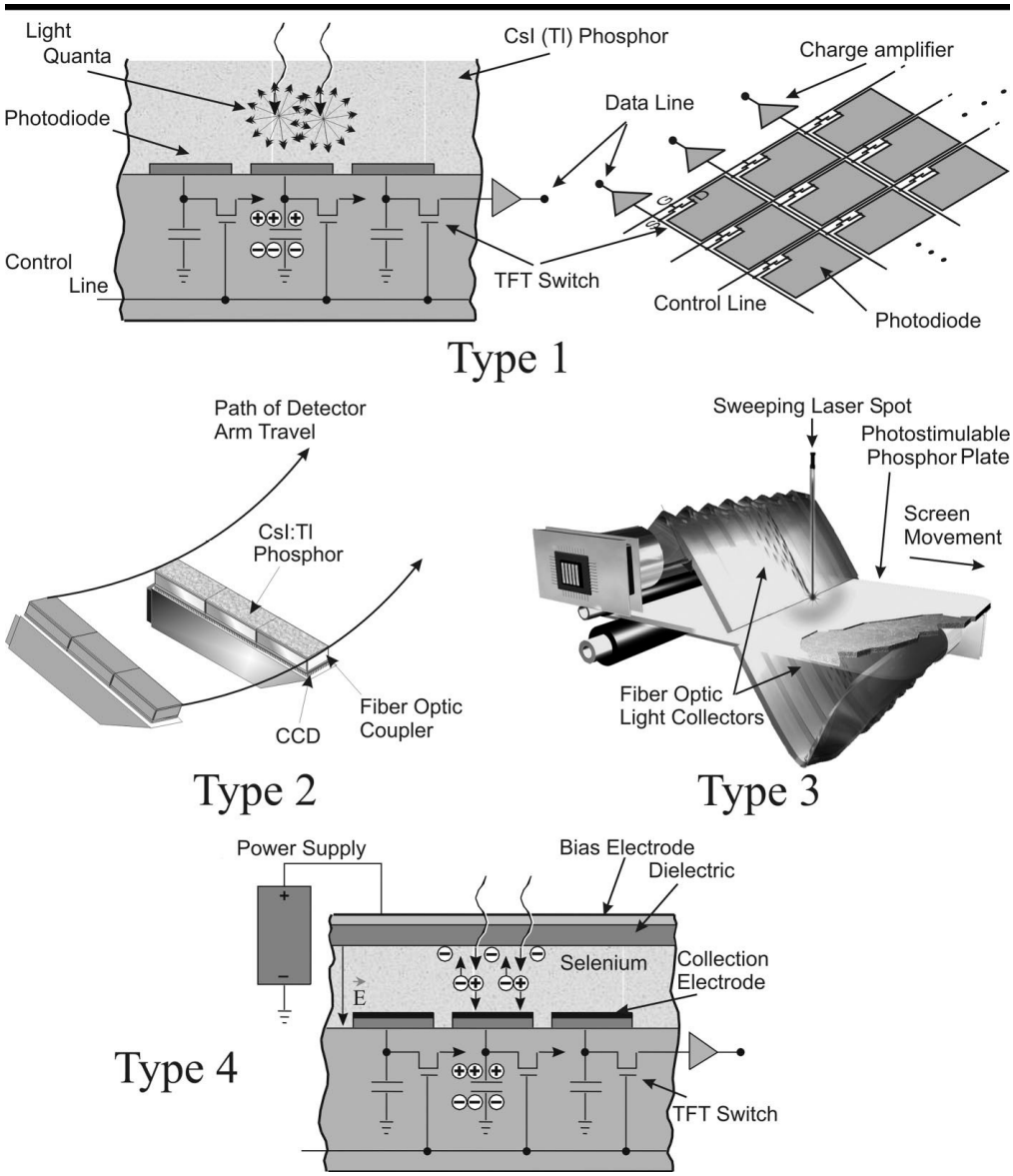

Figure 1-15: Four types of digital x-ray detector.

Type 1: cesium-iodide (CsI) phosphor on a flat panel composed of amorphous silicon and containing a large matrix of photodiodes with thin-film transistors (TFT) for readout. Type 2: CsI phosphor coupled to charge-coupled device (CCD) arrays. The long narrow detector array and a collimated x-ray beam scan across the body of interest to acquire the image. Type 3: photostimulable phosphor plate with a dual-sided reading system. Type 4: amorphous selenium, direct-conversion, flat-panel detector containing an array of electrodes and thin-film transistor switches for readout. Picture source: reference [14].

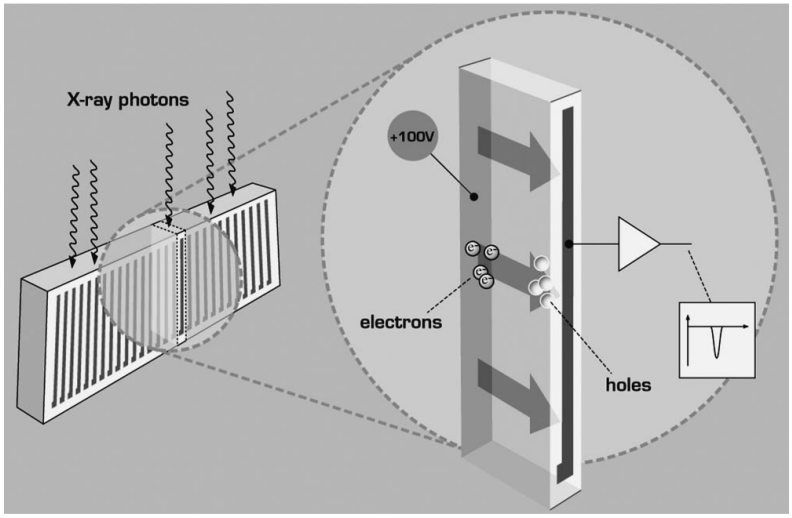

(a)

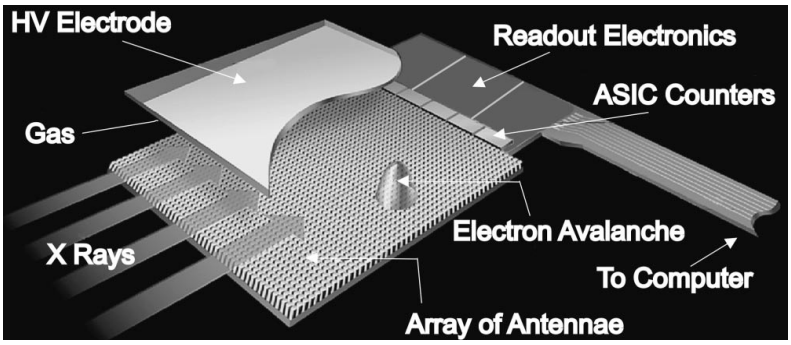

(b)

Figure 1-16: Two types of linear quantum-counting x-ray detectors.

(a): Silicon strip system by Sectra. (b): High pressure gaseous ionization detector by X-Counter. Picture source: reference [14].

For all the detectors discussed in Figure 1-15, the absorbed x-rays either directly or indirectly produce electric charges and the charge is accumulated to produce a signal measurement. The variation in the amount of charge production per x-ray contributes to the noise in the signal. In addition, high-energy x-rays are weighed more for they can produce more charges. The high-energy x-rays providing the lease image contrast due to their high penetration. To solve these two issues, the so-called "Quantum Counting Detectors" have

been developed[14], and two types of them are shown in Figure 1-16. Instead of accumulating charges from numerous x-rays, the absorbed x-ray quanta are counted, no matter the energies or how much charges they deposited on the detectors.

1.7 X-ray Source Based on CNT

Over the past century, although x-ray technology has evolved dramatically, the way to generate x-ray has not changed much. In many applications, including medical imaging, conventional x-ray sources are not sufficient for all purposes. The future x-ray source should have high spatial and temporal resolution, as well as small physical size. A new kind of x-ray source, field emission x-ray source based on CNT, has been developed recently. This x-ray source has sub-micro second temporal resolution, and can be miniaturized easily. Several imaging systems based on it have been built. In the next several chapters, I will introduce my research on x-ray sources and imaging systems based on this technology.

Chapter 2: CNT and Field Emission Electron Source

2.1 Basics about CNT

2.1.1 Discovery of CNT

Carbon is one of the elements scientists have known and studied first. Graphite and diamond both belong to the carbon family. The discovery of fullerenes in 1985[15] opens the door to a great variety of hollow, closed carbon structure. Carbon nanotubes, as the fourth crystalline form of carbon, were first observed in 1991 by Sumio Iijima[16]. The samples were created by a direct-current arc discharge between carbon electrodes immersed in argon, a technique that had been used to mass-produce the already known fullerene molecules. The TEM images (Figure 2-1) show the new concentric shell structure of carbon. For the number of shell are more than one, they are named multi-walled carbon nanotubes (MWNTs). Soon after the discovery, the carbon nanotubes attracted lots of attention for its unique structure. Different synthesis techniques were developed and the mechanical, electronic, thermal and chemical properties were simulated and measured. Two years later, single-walled carbon

nanotubes (SWNTs) were discovered by Iijima[17] and Bethune[18] independently. The SWNTs have only one carbon shell and have smaller diameters (~1 nm) in general.

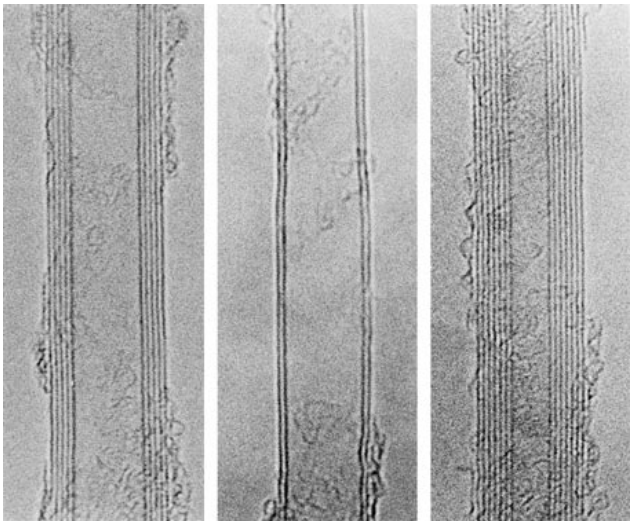

Figure 2-1: TEM images of carbon nanotubes.

The first high-resolution transmission electron microscopy (TEM) images showing cylindrical molecules with five, two and seven concentric walls (from left to right). Picture source: reference [16].

2.1.2 The Structure of CNT

To explore the properties of carbon nanotubes, it is necessary to understand their unique structure. MWNTs are essentially concentric SWMTs, so we can start with the simple case. A SWNT can be considered as a single layer of a graphite crystal rolled up into a seamless cylinder, usually with a small number (normally 10 to 40) of carbon atoms along the circumference and a long length (micro meters) along the axis[19]. A carbon nanotube can be defined by its chiral vector:

$$Ch = na_1 + ma_2 = (n, m)$$ **Equation 2-1**

It is often described by the pair of indices (n, m) that denote the number of unit vectors na_1 and ma_2 which compose the chiral vector. As shown in Equation 2-1, the chiral vector connects two crystallographically equivalent sites on a two-dimensional grapheme sheet. If we connect sites *O* and *A*, and sites *B* and *B'*, a nanotube can be constructed. The vectors OA and OB define the chiral vector and the translational vector T of the nanotube, respectively.

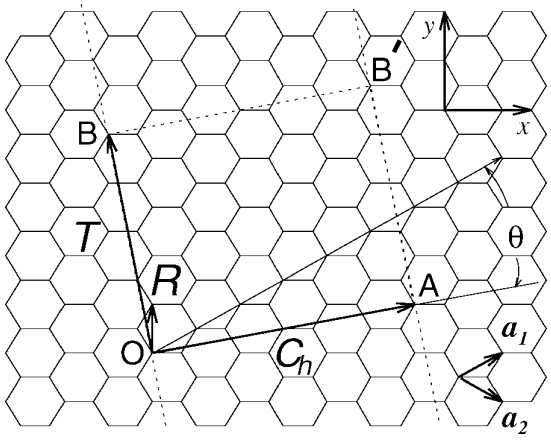

Figure 2-2: From graphite to carbon nanotubes.

Unrolled honeycomb lattice of a nanotube. A (4,2) nanotube can be constructed by joining the line *AB'* to the line *OB*. Picture source: reference [20].

From Figure 2-2, we can also see that there is a certain angle θ, the chiral angle, defined by the chiral vector and the a_1 direction (also known as zigzag direction). The so-called zigzag and armchair nanotubes correspond to θ=0° and θ=30°, respectively. All other nanotubes (0°<θ<30°) are called chiral tubes. The nanotube diameter can be given in terms of the indices (n, m):

$$d_t = C_h / \pi = \sqrt{3} a_{c-c} (m^2 + mn + n^2)^{1/2} / \pi$$ **Equation 2-2**

where $a_{c\text{-}c}$ is the nearest-eighbor C-C distance (1.421Å for graphite sheet). The chiral angle can be given by:

$$\theta = \tan^{-1}\left[\sqrt{3}m/(m+2n)\right] \qquad \textbf{Equation 2-3}$$

So, a nanotube can be specified by either the (n, m) indices or d_t and θ, equivalently.

The nanotubes can be either open-ended or close-ended. For close tubes, fullerene structures are needed at both ends, as illustrated in Figure 2-3. From this point of view, closed nanotubes can also be derived from the bucky-ball molecule by adding belts of atoms[21].

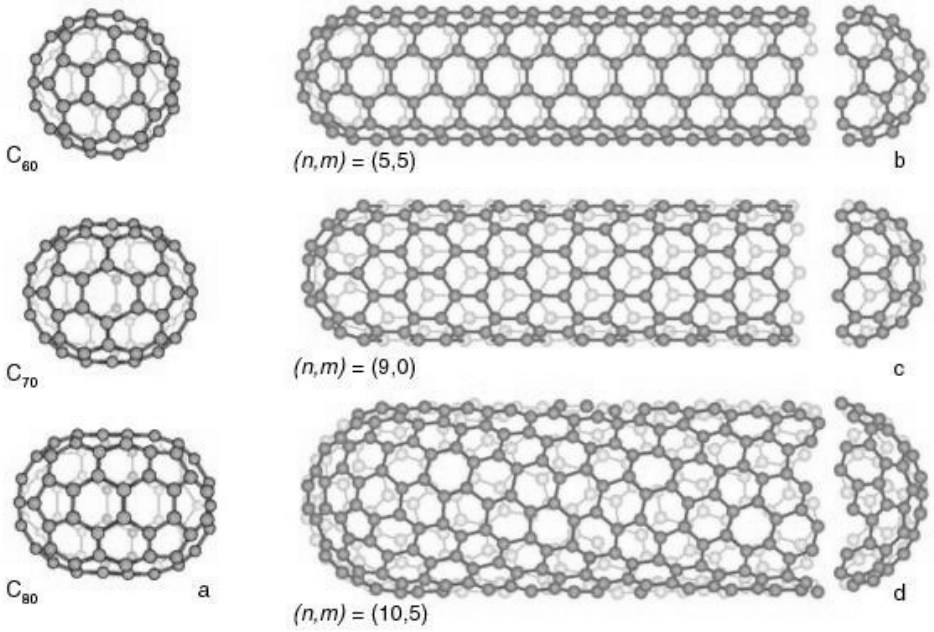

Figure 2-3: Relation between buckyball and carbon nanotubes.

(a): Alternative way to construct nanotubes from buckyball. (b), (c), and (d): Zigzag, armchair, and chiral nanotubes, respectively. Picture source: reference [21].

2.1.3 Properties of CNT

The unique structure, single element composition, and many possible combinations of the indices pair make the properties of CNT very unusual. Many exceptional properties, including electronic, mechanical, thermal, and chemical ones, have been explored both theoretically and experimentally during the past 15 years.

Although grapheme is a zero-gap semiconductor, both theoretical[22-24] and experimental[25] results have proved that carbon nanotubes can be either metals or semiconductors with different energy gaps, depending sensitively on the diameter and helicity of the tubes (i.e., on the indices pair). The SWNTs obey the rules as follow: (*n, n*) tubes are metallic; (*n, m*) with $n-m=3j$, where j is a nonzero integer, are very tiny-gap semiconductors due to curvature effect; and all others ($n-m=3j\pm1$) are large-gap semiconductors. As the tube diameter d_t increases, the band gaps of the large-gap and tiny-gap decrease as order of $1/d_t$ and $1/d_t^2$, respectively. Practically, the energy gap in the tiny-gap variety would be so small that at room temperature the thermal energy is sufficient to excite electrons from the valence to the conduction band[20]. Hence, all the nanotubes with $n-m=3j$ can be considered to be metallic. Electronic densities of states for three typical nanotubes are shown in Figure 2-4. If the distribution of the indices pair is random, one third of the nanotubes would be metallic. The carbon nanotubes can be used as junctions between

metal-semiconductor, semiconductor-semiconductor, and metal-metal. Although several methods have been developed to separate these two kinds of nanotubes, none of them has been completely successful so far. MWNTs may have different electronic properties from shell to shell.

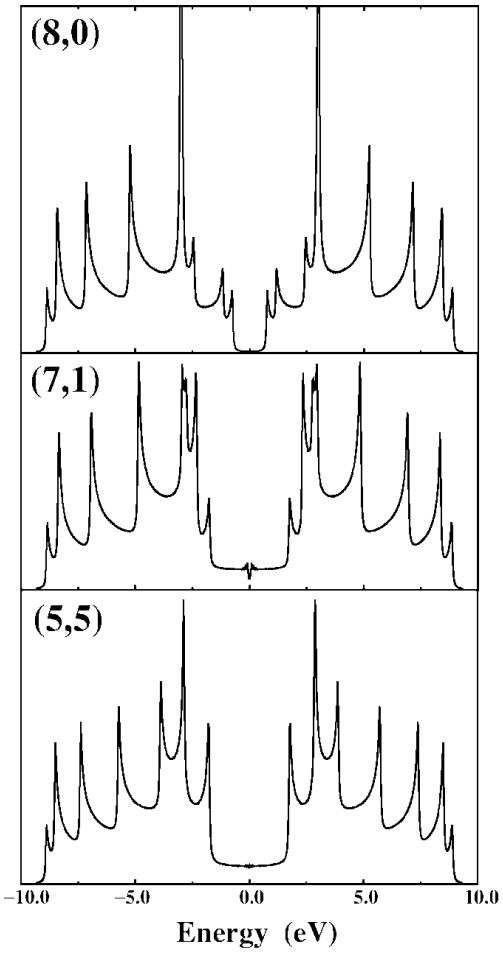

Figure 2-4: Electronic densities of states (DOS) of carbon nanotubes.

The (5,5) armchair nanotube is metallic due to symmetry. The (7,1) chiral nanotube has a tiny gap due to curvature effect, however, displays a metallic behavior at room temperature. The (8,0) zigzag tube is a semiconductor with large gap. Picture source: reference [26].

Because the carbon-carbon bond in the grapheme layer is one of the strongest chemical bond in nature, carbon nanotubes are expected to have exceptional mechanical

properties. Both theories[27] and experimental results[28, 29] show that carbon nanotubes have large Young's modulus up to 1.8 TPa. On the other hand, carbon nanotubes buckle rather than break like other materials with high Young's modulus. The buckling process is reversible. This phenomenon has been shown under atomic force microscopy (AFM) measurement[30].

At temperatures above 1000˚C and below room temperature, the linear dependence of specific heat and thermal conductivity has been reported[31]. The thermal properties have not been as extensively studied as electrical and mechanical properties, partly due to the difficulties in measurement on single carbon nanotube level. With the help of micro-fabrication, more about the thermal properties will be revealed.

2.1.4 Applications of CNTs

Although early research about carbon nanotubes was focused on syntheses and characterization, the investigations of application development have dramatically increased during the past decade. The extraordinary mechanical properties, unique electrical properties along with chemical and thermal stability make CNTs suitable for many applications[32]. Some of the applications are shown in Figure 2-5.

- Scanning probe microscopy: the small tip diameter, large aspect ratio, and large young's modulus give the CNT-equipped AFM and SPM tips ability to detect sub-nanometer feature and deep trenches.

- Nano-electronics: semiconductor nanotubes can be used for metal-semiconductor (Schottky) diodes, PN junction diodes, and field-effect transistors (FETs), whereas metal nanotubes can be used for single-electron tunneling transistors.

- Field emission: the large aspect ratio and unique electrical properties make CNTs the ideal field emitters. Potential applications include vacuum microelectronics, microwave amplifiers, field emission displays, and x-ray tubes.

- Chemical, physical, and biological sensors: the small size, large surface to volume ratio, and unique one dimension structure make CNTs the ultimate sensors which can potentially improve sensitivity, lower detection limit, reduce sample amount, and increase detection speed.

- Composites: carbon nanotubes enhanced composites are a near-term application and some of them have been commercialized. The examples include conducting polymers, multifunctional polymer composites, conducting metal matrix composites, and higher fracture-strength ceramics.

- Other applications: noticeable other applications include integrated circuit manufacturing, catalyst support and adsorbents, storage/intercalation of hydrogen.

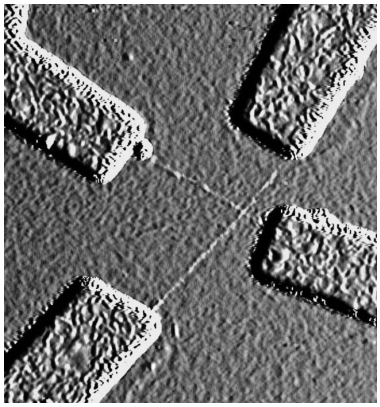
(a)

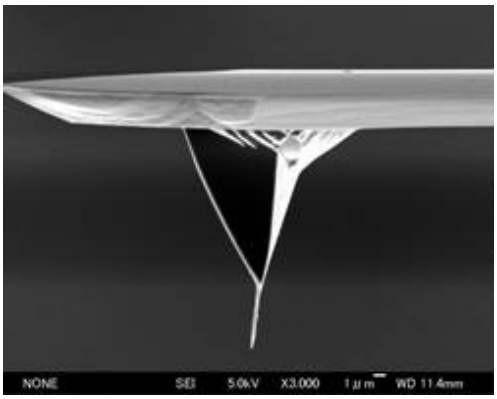

(b)

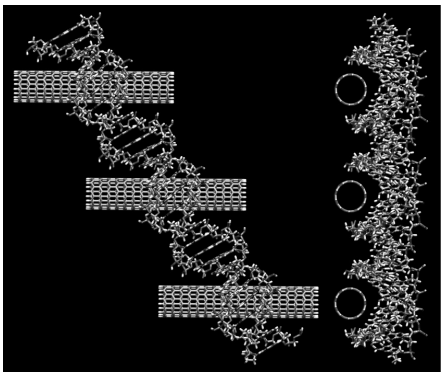
(c)

(d)

Figure 2-5: Applications based on CNTs.

(a): CNT microelectronic circuit. Picture source: reference [33]. (b): AFM tip equipped with CNT. (c) DNA interaction with CNTs. (d): Field emission display based on CNT. Picture source: Motorola research.

2.2 Field Emission Theory

Electron sources are the basic component in many scientific and industrial apparatus and applications. Field emission and thermionic emission are two of the most popular methods to generate electron sources. The mechanisms of the two emissions are both based on the free electron theory of metals proposed by Sommerfeld[34] in 1928.

2.2.1 Electron Emission from a Metal Surface

Consider a semi-infinite metal occupying the half space from z=-∞ to z=0. According to the free electron theory, an electron inside the metal sees a constant zero potential. The potential on the vacuum side is determined by several factors. The Fermi energy, denoted as E_F, can be calculated by quantum mechanics. At zero temperature, a certain minimum energy, normally called work function ϕ, must be applied before an electron can be "free" from the metal. According to classical electrostatics, an electron situates at a finite distance from the plane surface of a perfect conductor experiences an attractive force by an "image" positive charged particle: $-e^2/4z^2$, where the z axis points outwards from the metal. So, the potential energy of an electron on the vacuum side is given by:

$$V(z) \approx E_F + \phi - e^2/4z \qquad \textbf{Equation 2-4}$$

According to the microscopic studies of the potential barrier at metal-vacuum interface, Equation 2-4 is only valid for z>3Å. In the free-electron theories of electron emission, it is assumed that Equation 2-4 remains valid up to a point z_c such that $V(z_c) = 0$. When an external electric field F is applied to the surface, a new term -eFz (F>0) should be added on the right side of Equation 2-4. In summary, the potential experienced by an electron in a semi-infinite metal-vacuum field is given by:

$$\begin{aligned} V(z) &= E_F + \phi - e^2/4z - eFz \quad && \text{for } z > z_c \\ &= 0 && \text{for } z < z_c \end{aligned} \qquad \textbf{Equation 2-5}$$

In Figure 2-6, the potential barrier with a typical value of $E_F + \phi$ and under an applied field is shown. The peak value of the potential occurs at:

$$z_m = (e/4F)^{1/2} = 1.9/F^{1/2}\ \mathring{A} \qquad (F \text{ in } V/\text{Å}) \qquad \textbf{Equation 2-6}$$

with the value:

$$V_{\max} = E_F + \phi - (e^3 F)^{1/2} = E_F + \phi - 3.79F^{1/2} eV \qquad \textbf{Equation 2-7}$$

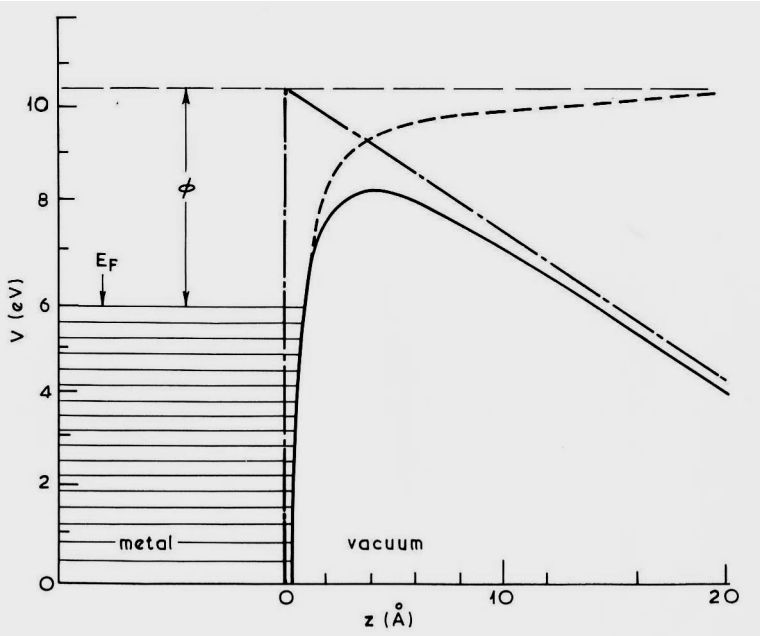

Figure 2-6: Penetration of the potential barrier at applied electrical field.

The potential barrier seen by an electron in a field emission experiment (solid line). The contributions of the image potential and of the applied field ($F=0.3V/\text{Å}$) are shown by the broken and the broken-solid line, respectively. Picture source: reference [34].

Now, let's consider the emission current based on the free-electron theory. Let W be the normal energy defined by $W = \frac{\hbar^2 k_z^2}{2m}$. We can assume (this is justified because the electric field is negligible inside the metal) that the number of electrons with normal energy between

W and $W+dW$ impinging on the surface barrier from the metal is practically identical with its equilibrium value given by:

$$N(W,T)dW = \frac{mdW}{2\pi^2\hbar^3}\int_W^\infty f(E)dE$$
$$= \frac{mk_BT}{2\pi^2\hbar^3}\ln\left[1+\exp\left(-\frac{W-E_F}{k_BT}\right)\right]dW \qquad \textbf{Equation 2-8}$$

where $f(E)$ is the probability of an electron state with energy E being occupied, T denotes the temperature, and other parameters are constants.

So, the current density under applied field F, i.e., the number of electrons emitted per unit area per unit time multiplied by the magnitude of the electronic charge, is given by:

$$J(F,T) = e\int_0^\infty N(W,T)D(W)dW \qquad \textbf{Equation 2-9}$$

where $D(W)$ is the transmission coefficient defined by the current density of transmitted wave over the value of incident wave. The integration can be separated into two parts by

$$W_l = V_{\max} + \left(1-\frac{1}{\sqrt{2}}\right)(e^3F)^{1/2} \qquad \textbf{Equation 2-10}$$

where $V_{\max}$ is defined as Equation 2-7. For the two parts, different approximations can be taken. Hence, we can get:

$$J(F,T) = \frac{emk_BT}{2\hbar^3\pi^2}\left\{\int_0^{W_l}\frac{\ln\{1-\exp[-(W-E_F)/k_BT]\}dW}{1+\exp[Q(W)]} + \int_{W_l}^\infty \ln\left[1+\exp\left(-\frac{W-E_F}{k_{BT}}\right)\right]dW\right\}$$

Equation 2-11

where $Q(W)$ is determined by $D(W,F) = \{1+\exp[Q(W)]\}^{-1}$.

2.2.2 Field Emission

Under typical field emission conditions ($\phi \approx 4eV$ and $F \approx 0.4V/\overset{o}{A}$), the second integral contributes a negligible amount to the current density and the integrand in the first integral vanishes except in the immediate neighborhood of the Fermi level. Therefore, we can drop the second integral and replace the limits in the first integral by -∞ and +∞, respectively. For typical values of the parameters ($\phi > 3eV$ and $F < 0.6V/\overset{o}{A}$), we have $\exp[Q(W)] >> 1$. So we can obtain:

$$J(F,T) = \frac{emk_BT}{2\hbar^3\pi^2}\int_{-\infty}^{+\infty}\exp[-Q(W)]\ln\left[1+\exp\left(-\frac{W-E_F}{k_BT}\right)\right]dW \qquad \textbf{Equation 2-12}$$

Since most of the contribution comes from the immediate neighborhood of the Fermi level, we can take the Taylor expansion of the first two terms around E_F:

$$-Q(W) = -b_0 + c_0(W-E_F) - f_0(W-E_F)^2 + \cdots \qquad \textbf{Equation 2-13}$$

where b_0, c_0, and f_0 are functions of F, ϕ, E_F, and W. Keeping only the first two terms, we can get:

$$J(F,T) = \frac{emk_BT}{2\pi^2\hbar^3}e^{-b_0}\int_{-\infty}^{+\infty}e^{c_0(W-E_F)}\ln\left[1+\exp\left(-\frac{W-E_F}{k_BT}\right)\right]dW \qquad \textbf{Equation 2-14}$$

The integral in Equation 2-14 can be evaluated analytically, and the result is:

$$J(F,T) = \frac{e^3F^2}{16\pi^2\hbar\phi t^2(y_0)}\frac{\pi c_0k_BT}{\sin(\pi c_0k_BT)}\exp\left[-\frac{4}{3e}\left(\frac{2m}{\hbar^2}\right)^{1/2}v(y_0)\frac{\phi^{3/2}}{F}\right] \qquad \textbf{Equation 2-15}$$

where y_0, $t(y)$, and $v(y)$ are functions of F, ϕ, E_F, and W. The detail expression can be found in reference [34].

It can be proved that Equation 2-15 is a valid approximation when the following two conditions stand:

$$\phi - \left(e^3 F\right)^{1/2} > \pi^{-1}\left[\frac{\hbar^4}{m^2 e^2}\right]^{1/4} (eF)^{3/4} + k_B T\left(1 - c_0 k_B T\right)^{-1} \qquad \textbf{Equation 2-16}$$

$$1 - c_0 k_B T > \left(2 f_0\right)^{1/2} k_B T \qquad \textbf{Equation 2-17}$$

From Equation 2-16 and Equation 2-17, the field emission region can be determined as a function of F and T for $\phi = 4.5eV$ (Figure 2-7).

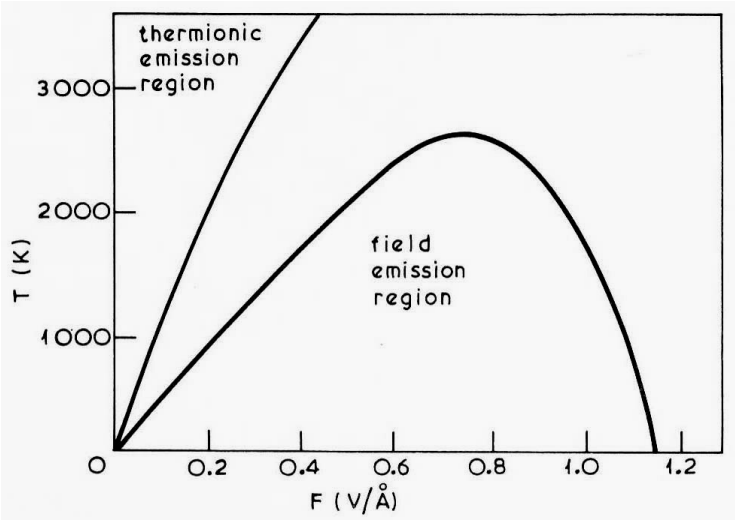

Figure 2-7: Field emission and thermionic emission regions.

Field emission and thermionic emission regions of temperature and applied field for a 4.5 eV work function. Picture source: reference [34].

At low temperature, i.e., when $\pi c_0 k_B T << 1$, Equation 2-15 can be further simplified to the form of the famous Fowler-Nordheim equation (Fowler and Nordheim, 1928; Nordheim, 1928):

$$J(F) = A' F^2 \exp\left(-B' \phi^{3/2} / F\right) \qquad \textbf{Equation 2-18}$$

where

$$A' \equiv e^3 \Big/ \left[16\pi^2 \hbar \phi t^2 \left(\frac{(e^3 F)^{1/2}}{\phi} \right) \right] \qquad \textbf{Equation 2-19}$$

$$B' \equiv \frac{4}{3e} \left(\frac{2m}{\hbar^2} \right)^{1/2} v\left(\frac{(e^3 F)^{1/2}}{\phi} \right) \qquad \textbf{Equation 2-20}$$

This is one of the most important equations in electron emission theory and has found many and varied applications. It is also noticeable that if one plots $\ln(J/F^2)$ versus $1/F$, the corresponding curve is a straight line, known as the Fowler-Nordheim (FN) plot.

One thing deserves mention is that the F is the local field around the emission area. In real case (Figure 2-8), the value is related to the macro applied field:

$$F = \beta V / d \qquad \textbf{Equation 2-21}$$

where V is the total voltage drop between anode and cathode, d is the distance between two electrodes, and β is known as the field enhancement factor which is determined by the cathode geometry. According to electrostatic theory it can be easily proved that the sharper the tip, the larger the field enhancement factor, and the lower applied voltage required to obtain the same field emission current. Combining the equations above, for a sharp tip emitter with emission area A, we can get:

$$I = JA = aV^2 \exp(-b\phi^{3/2}/V) \qquad \textbf{Equation 2-22}$$

where the constants a and b are defined by:

$$a = 1.42 \times 10^{-6} A\beta^2 \exp(10.4/\phi^{1/2}) / d^2\phi \qquad \textbf{Equation 2-23}$$

$$b = 6.44 \times 10^7 \phi^{3/2} d / \beta \qquad \textbf{Equation 2-24}$$

The plot $\ln(I/V^2)$ versus $1/V$ is also a straight line for field emitters, and this curve is also called Fowler-Nordheim (FN) plot.

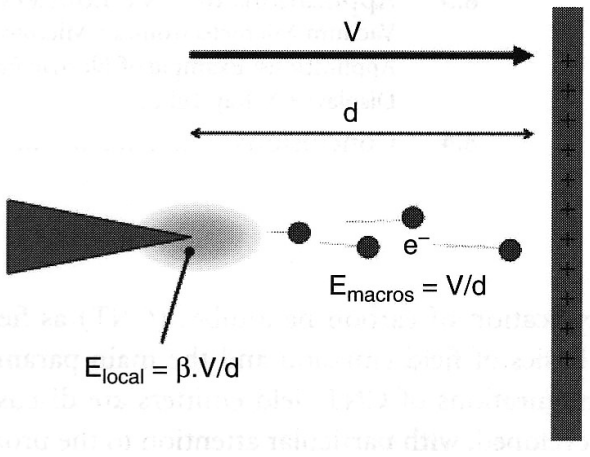

Figure 2-8: Schematic of a real field emitter.

The local field is enhanced by a certain factor called "field enhancement factor". Picture source: reference [32].

2.2.3 Thermionic and Intermediate Emission

At high temperature and weak applied field, most of the contribution to the integral in Equation 2-14 comes from a small region of energy at the top of the surface potential barrier. So, different approximation should be taken instead of the approach of field emission calculation. Here, $N(W,T)$ and $D(W,T)$ can be replaced using the expansions around $W \approx V_{\max}$. The integral can be calculated analytically:

$$J(F,T) = \frac{em(k_B T)^2}{2\pi^2\hbar^3}\left(\frac{\pi t h_0}{\sin \pi t h_0}\right)\exp\left[-\frac{\phi - (e^3F)^{1/2}}{k_B T}\right] \qquad \textbf{Equation 2-25}$$

where

$$h_0 \equiv \left(\frac{F\hbar^4}{m^2 e^5}\right)^{1/4}\frac{(e^3F)^{1/2}}{\pi k_B T} \qquad \textbf{Equation 2-26}$$

The conditions to make it valid are:

$$\ln\left[(1-h_0)/h_0\right]-\frac{1}{h_0(1-h_0)}>-\pi\left(\frac{me}{\hbar^2}\right)^{1/2}(eF)^{-3/4}\left[\phi-(e^3F)^{1/2}\right] \qquad \textbf{Equation 2-27}$$

$$\ln\left[(1-h_0)/h_0\right]-\frac{1}{1-h_0}>-\pi\left(\frac{me^3}{\hbar^2}\right)^{1/4}(eF)^{-1/8} \qquad \textbf{Equation 2-28}$$

The thermionic emission region determined by these two conditions is shown in Figure 2-7 for $\phi=4.5eV$. For very weak applied field, i.e., $\pi h_0 << 1$, Equation 2-25 can be further simplified to the well-known Schottky formula (Schottky, 1914; 1919; 1923):

$$J(F,T)=A_R T^2\exp\left[-\frac{\phi-(e^3F)^{1/2}}{k_B T}\right] \qquad \textbf{Equation 2-29}$$

where

$$A_R\equiv\frac{emk_B^2}{2\pi^2\hbar^3}=120A\cdot cm^{-2}\cdot\deg^{-2} \qquad \textbf{Equation 2-30}$$

According to Schottky formula, if we plot $\ln(J)$ versus $F^{1/2}$, we should obtain a straight line, known as Schottky lines.

Electron emission at intermediate region is often referred to as thermal-field emission (TF emission). Starting from Equation 2-11 and without those approximations, scientists have developed the analytical result of the current density with sufficient accuracy for any values of temperature and applied field. Those results reduce to Equation 2-15 and Equation 2-25 in the field emission and thermionic emission regions, respectively. Detailed expression can be found in reference [35].

2.2.4 Ideal Field Emitters

Field emission theory has been established for more than half a century; however, the applications are still limited compared to thermionic emission. Part of the reason is due to the lack of the field emitters with stable performance and low cost. According to the field emission equation, there are two parameters which affect the emission current: the work function and the applied field. The work function is determined by the atomic structure of the material and can be altered a little by chemical methods. On the other hand, the local field highly depends on the structure of the emitters. As discussed earlier in this chapter, it can be easily proved that the longer the tip and the smaller the diameter, the larger the field enhancement factor. For emitters made of same material, the larger the field enhancement factors, the lower the threshold voltage to emit electrons.

According to these theories, sharp field emitting microstructures (Figure 2-9) were proposed by Spindt in the form of micro-machined miniature tips[36]. However, the spindt-type emitters suffer from the low stability and limited lifetime for the cathodes (normally sharp metal tips) are vulnerable to heat, chemical reaction and ion bombardment[37]. The arcing damage to the spind-type tip is schematically shown in Figure 2-10. The field enhancement factor is dramatically lower after arcing.

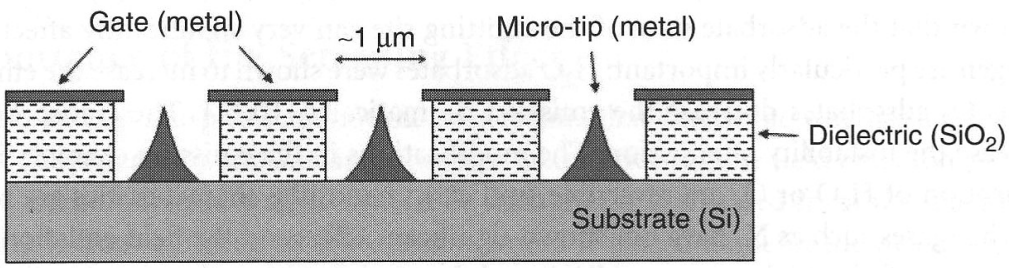

Figure 2-9: Schematic structure of a micro-machined array of Spint-type tips.
Picture source: reference [32].

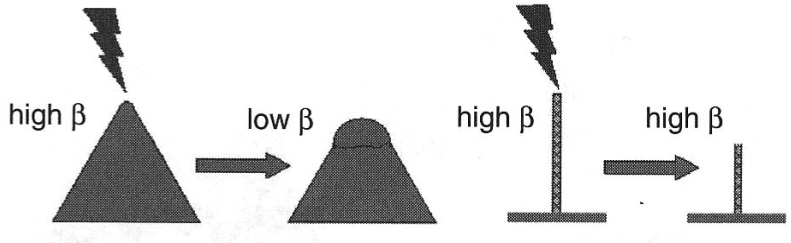

Figure 2-10: Schematics of arcing damage to field emitters.
Left: Spindt-type emitters. Right: CNT emitters. Picture source: reference [32].

Soon after the discovery of carbon nanotubes, scientists noticed that CNTs are the ideal emitters. The field enhancement factor is extremely large (in the order of thousands or tens of thousands) thanks to the small diameter and long aspect ratio. CNT emitters are also very stable due to the strong mechanical strength, and the inert thermal and chemical property. As illustrated in Figure 2-10, the arcing damage to the CNT emitters is small for the field enhancement factor does not degrade as much as the Spindt-type emitters. Up to date, stable emission current up to $4A/cm^2$ has been achieved using CNT emitters fabricated at UNC. Table 2-1 lists the threshold filed for some common emitters.

Table 2-1: Threshold field for common emitters.	
Cathode Material	Threshold Field (V/μm) for 10 mA/cm2
Mo tips	50-100
Si tips	50-100
p-type diamond	160
Defective CVD diamond	30-120
Amorphous diamond	20-40
Cesium-coated diamond	20-30
Graphite powders	10-20
Nano-diamond	3-5 (unstable > 30 mA/cm2)
Carbon Nanotubes	1-2 (stable >4000mA/cm2)

The field of potential applications of CNT based field emission is extremely wide. Any system that uses an electron source could potentially host a CNT field emission device. CNT emitters are best suited for portable devices and applications which need fast switching or ultrahigh frequency modulation. Among all the applications, field emission display and field emission x-ray tube are the most promising.

A variety of electron sources based on CNT have been fabricated. In our group, three types of sources are of most interest: micro field emission electron cathode (point electron source), macro field emission electron cathode (area electron source) and patterned (1D or

2D) electron cathodes. They are designed for different applications. During my doctoral study, I focused on point and area electron sources. In the last section of this chapter, I will discuss the point electron source based on CNT.

2.3 Point Electron Source Based on CNT

Point electron source based on CNT normally consists of only one or a few CNTs. In-situ scanning electron microscope (SEM) results have shown a stable emission current of 0.1-1μA from an individual single-wall carbon nanotube (SWNT). A recent report demonstrates that the CNT field emitter has a narrower spatial distribution and thus has higher brightness compared to the state-of-the-art LaB_6 and Schottky electron sources[38]. This property is desirable for precision vacuum electron devices such as the field emission electron gun used in electron microscope.

However, efficient and reliable method for fabrication of CNT point emitter is challenging. Direct growth of CNTs at predetermined locations has been demonstrated using chemical vapor deposition (CVD) techniques[39-41]. This approach requires selective deposition of nanometer to micrometer catalysts and a high reaction temperature. In general, it lacks control of the length, orientation and number of the CNTs grown. In laboratory experiments, the CNTs can be manually attached to a sample holder coated with adhesives

by a trial-and-error process[42-44]. A different approach is applied here to fabricate CNT-based point electron source.

2.3.1 Cathode Fabrication

Dielectrophoresis is a powerful technique that can manipulate and assemble small objects into predetermined patterns by the interaction between the external electrical field and the induced dipole moments[45]. This technique has been applied to different systems[46, 47]. It has been shown that CNTs can be assembled into sub-micrometer diameter fibrils with controllable lengths by the dielectrophoresis method[48]. Based on the same technique, point electron source can be fabricated by mounting very short CNT bundles on pre-formed tungsten tips.

SWNT bundles, produced by the laser ablation method in our group, were first purified and etched to either ~0.5μm or ~2μm in bundle length by an oxidation process [49] by Huaizhi Geng. Prior experiments have shown that the processed materials maintain the basic characteristics of the nanotubes and are hydrophilic due to the presence of the COOH functional groups [50, 51]. MWNTs produced by the plasma CVD method were used without further processing. The nanotubes were dispersed in de-ionized water with the aid of sonication. The tungsten tips are formed by etching the commercial tungsten wire with

0.5mm in diameter in 2M NaOH solution at 5V bias. By controlling the cut-off time, we can obtain tungsten tips with sub-micron meter diameter.

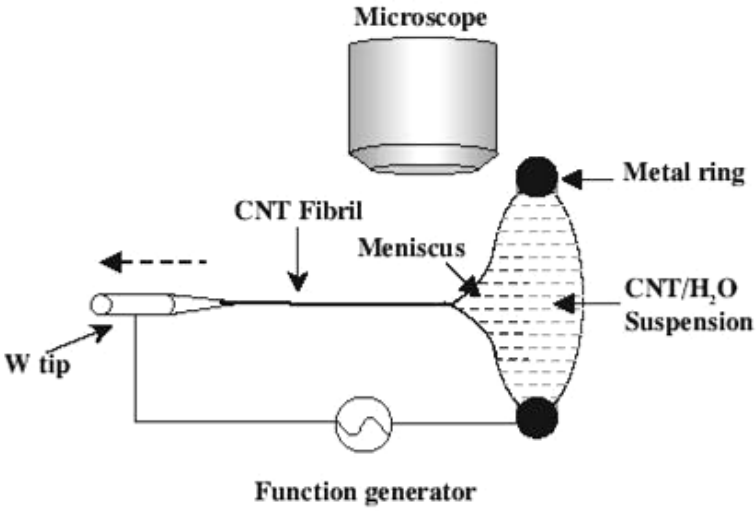

Figure 2-11: Schematic of the dielectrophoresis setup.

The first group of CNTs adhered to the apex of the W tip and became the new outermost surface of the electrode where the next CNT precipitated. By gradually withdrawal of the W electrode from the liquid a continuous fibril was formed.

The experimental set-up comprises two electrodes, a chemically etched tungsten wire and a metal holder, mounted on separate translation stages under an optical microscope, as shown in Figure 2-11. An AC field of 10V at 2 MHz was applied between the tungsten wire and the metal holder which contained the nanotube/water suspension. In Figure 2-12, the computer simulations using commercial software show that the polarized CNTs were attracted to the tungsten tip where the electrical field gradient is high when the permittivity of the medium is lower than the value of the nanotubes. To draw a continuous tip, the tungsten

wire was translated horizontally to contact the surface of the suspension and was gradually withdrawn under the electrical field until a nanotube tip with a desired length was formed on the apex of the tungsten wire.

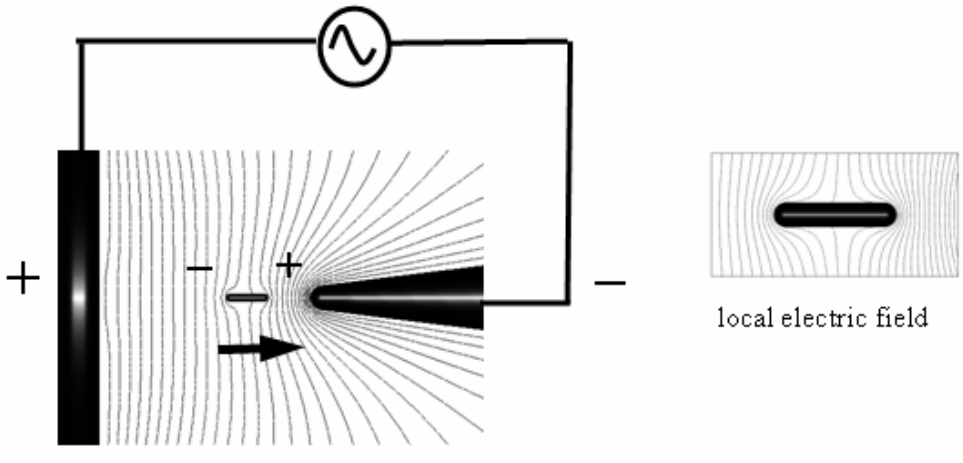

Figure 2-12: Illustration of the dielectrophoresis assembly process.

The electrical field distribution shown was simulated by a commercial package (LorentzE V6.0). The polarized CNTs in water were first aligned along the field direction due to the torque acting upon the induced dipole. When the permittivity of the object is larger than that of the medium the result shows a positive dielectrophoresis force driving the nanotubes towards the high field region which is consistent with the theory [45].

Thirteen samples were fabricated under same conditions for this study. The length of the CNT tip was controlled by the travel distance of the W tip under an AC field. Figure 2-13 (a) shows the scanning electron microscope (SEM) image of one sample. The individual nanotubes and the tip are aligned along the electrical field direction which is along the cone axis of the W tip. Figure 2-13 (b) is the histogram obtained from measuring the angle formed by the CNT tip and the W wire. All the tips are confined within a 12˚ cone angle. The very

end of the fibril comprises only a single carbon nanotube bundle. At the CNT/metal interface, entangled nanotubes adhere on the surface of the W wire and coagulate into a thin fibril with only a few nanotubes in the radial direction, as shown in Figure 2-13 (c) for a MWNT tip.

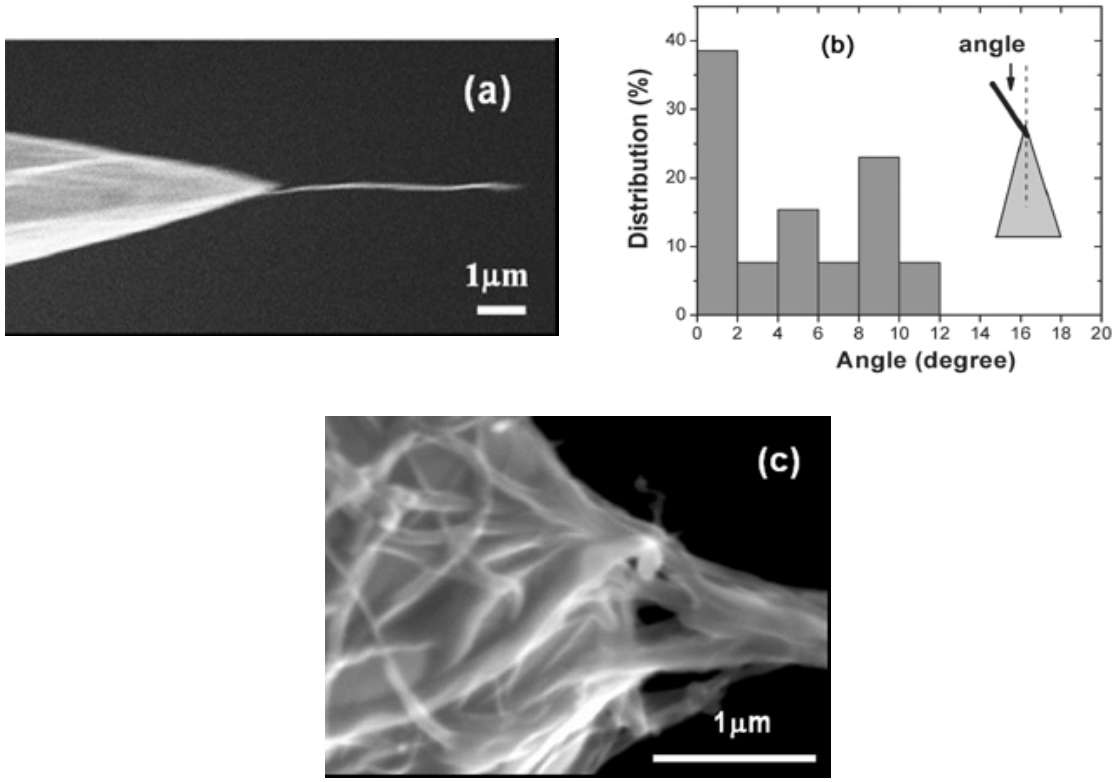

Figure 2-13: Images of SWNT-tungsten tip.

(a): An SEM image of a typical SWNT-tungsten tip fabricated by the dielectrophoresis method. One end of the SWNT bundle anchored on the apex of the W wire. (b): The histogram obtained from measuring the angles between the CNT tips and the W wires. All the tips are confined within a 12^{o} cone angle. (c): At the CNT/metal interface, entangled nanotubes adhered on the surface of the W wire and coagulated into a thin fibril with only a few nanotubes in the radial direction.

2.3.2 Field Emission Characteristics

To measure the electron field emission characteristics, we used a customized device with a CNT tip mounted on a micrometer head as the cathode and an opposing metal plate as the anode. The distance between the two electrodes was adjusted by translating the micrometer head and was fixed to ~200μm (estimated from the image taken using a CCD camera connected to a microscope). The set-up was placed inside a vacuum chamber at base pressure of $5x10^{-7}$ Torr.

The total emission current from the CNT tip was collected as a function of the applied voltage. Figure 2-14 and inset show the result of a SWNT tip with a ~50nm tip diameter. The emission current-voltage characteristics exhibited the classic Fowler-Nordheim curve with a linear relation between $\ln(I/V^2)$ and $1/V$. The emission current reached 5 μA at less than 1000V applied voltage which gives an estimated current density of $2.5x10^5 A/cm^2$.

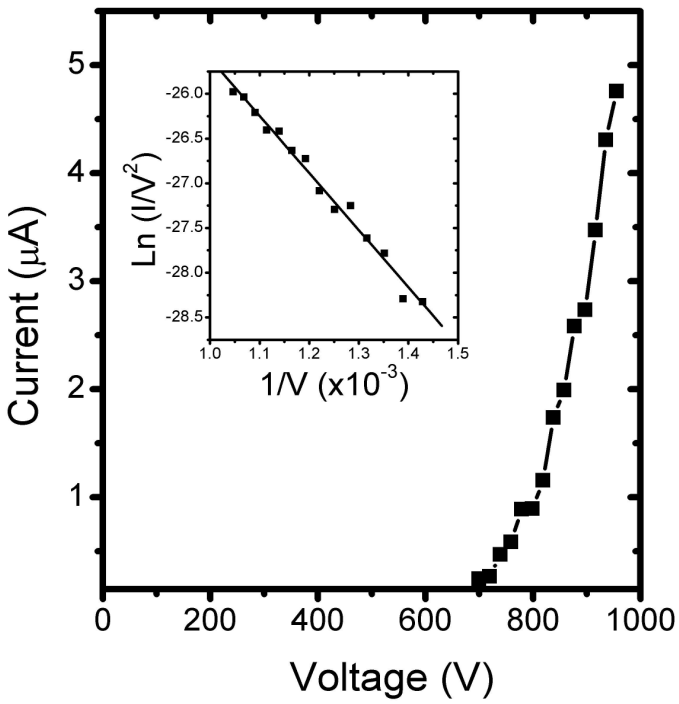

Figure 2-14: Electron field emission properties of CNT emitters.

Electron field emission properties of SWNT tip measured using point-plane geometry at 10^{-7} torr base pressure. The emission current-voltage characteristics exhibited the classic Fowler-Nordheim type behavior with a linear relation between $\ln(I/V^2)$ and $1/V$.

The emission stability was measured by monitoring the variation of the emission current with time for 10 hours continuously in D.C mode at a fixed voltage. Figure 2-15 shows the data from a SWNT tip (~50nm in diameter) measured sequentially at three different voltages. The emission current was stable at 1μA and 2.8μA when the applied voltage was fixed at 800V and 1000V, respectively, with no overall decay of the emission current. With a ballast resistor in series with the cathode, the local current fluctuation was calculated to be 5% at 1μA and 2.5% at 2.8μA. The emission current from the same sample reached 5.5μA when the voltage was further increased to 1200V, but was then suddenly dropped to zero after one

hour. No current was detected afterwards even at a higher voltage. SEM examinations revealed catastrophic failure from fracture of the W wire and disappearance of the entire CNT tip as shown in Figure 2-15 inset. It is attributed to resistive heating at the W and CNT interface.

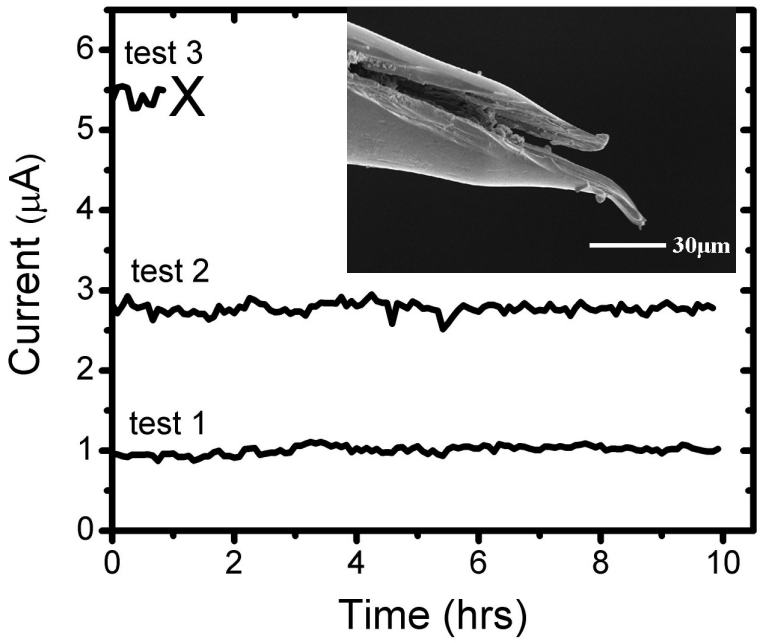

Figure 2-15: Stability measurement of SWNT-tungsten tips.

Measurement was carried out sequentially at 1μA, 2.8μA and 5.5μA when the applied voltage was fixed at 800V, 1000V and 1200V, respectively. The emission was stable at 1μA and 2.8μA for up to 10 hours before the failure appeared at 5.5μA. The inset is the SEM image of the W tip measured after failure showing fracture of the W wire and disappearance of the CNT tip.

To record the emission pattern from the CNT tip the metal anode used in the above measurements was replaced with a phosphor-coated ITO (indium-tin-oxide) glass. The image formed on the phosphor screen by the emitted electrons was recorded by a CCD camera placed outside the vacuum chamber. Figure 2-16 shows the emission images obtained from a

MWNT tip. A single emission spot was observed in all operating voltages, consistent with the SEM results which showed that there is only one close-packed CNT tip anchored on each tungsten wire. At 1400V the diameter of the bright spot on the phosphor screen is about 200μm which gives a beam divergence angle of 50˚. The large spread angle results from the electrical field distribution in the point-plane geometry rather than the intrinsic divergence angle of the field emission electrons from the nanotubes.

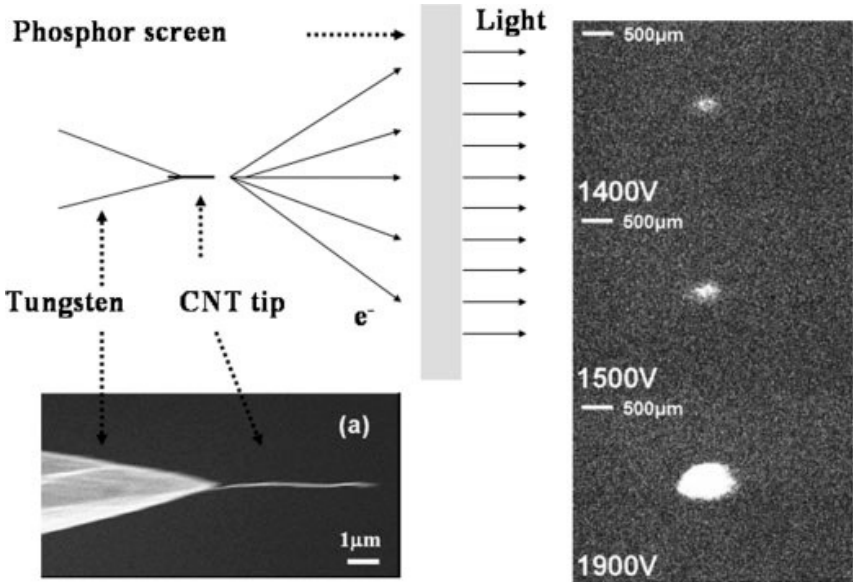

Figure 2-16: The emission patterns from a MWNT-tungsten tip at different applied voltages.

A single emission spot was observed in all operating voltages. The large divergence angle (50^{o} at 1400V) is due to the electrical field distribution in the point-plane geometry rather than the intrinsic divergence angle of the field-emitted electrons from the nanotubes.

Chapter 3: FE X-ray Source and Application

Since 2000, several research centers across the world started the investigation of the feasibility of field emission x-ray source using carbon nanotubes. As one of the pioneer centers, our group first generated x-ray using CNT cathode in 2002. Since then, we have made lots of improvement in terms of x-ray tube current, stability, and lifetime. In this chapter, I will introduce the area electron source and single beam x-ray tube. In the second half of this chapter, the result of the prototype multi-beam x-ray source is discussed.

3.1 Area Electron Source Based on CNT

Although point electron source has shown great potential for applications such as TEM guns[52], the emission current is not high enough for applications such as X-ray imaging due to the limited number of CNT emitters. For X-ray imaging devices, such as mammography and CT, a x-ray source with current of 30-100mA [53] is required. To obtain higher current, more CTN emitters are needed. In our group, we used electrophoresis deposition (EPD) method for fabrication of area electron sources.

3.1.1 Area CNT Cathode Fabrication

Among all the methods to synthesis CNTs, we choose chemical vapor deposition (CVD) over others for the large production rate. By changing the synthesis parameters, CVD method can yield single-walled, double-walled, and multiple-walled CNTs with high purity. As we discussed in Chapter 2, the thinner CNTs have larger field enhancement factor. On the other hand, if the CNTs are too thin, the stability and life time are degraded. Overall, the double-walled and few-walled CNTs give the best performance. Most area cathodes are made of them.

The raw CNT material is cut to length of 10-20μm using the same sonication method introduced in Chapter 2. Two types of solutions, CNT solution and glass solution, are produced by following recipes, respectively:

CNT : ethanol : H_2O : $MgCl_2$ = 6mg : 400ml: 8ml : 2mg

SCB-13 : Fe : $MgCl_2$: ethanol : H_2O = 400mg : 120mg : 16mg : 400ml : 8ml

where SCB-13 is the commercial glass power. After sonication, the magnesium chargers will bundle with glass particles or the CNTs. Immersing two electrodes in the solution, under the guidance of applied field, the chargers will move to the negative electrode, which is the cathode to deposit CNTs. To achieve better bonding between cathode substrate and CNTs, a

glass layer is coated first. After electrophoresis deposition, the cathodes are further annealed in vacuum chamber at temperature close to the transaction temperature of glass particles.

To define the size and shape of the cathode, we need to open the area for CNT deposition and block the rest. For the first generation cathode, we used shadow masks and cylindrical metal substrates (Figure 3-1). This method works well for cathode size down to 1mm.

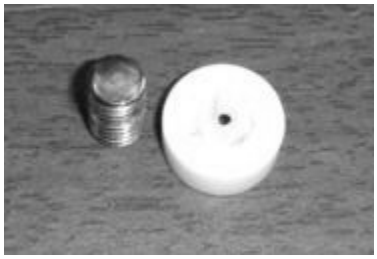

Figure 3-1: Cylindrical metal substrate and shadow mask made of Teflon.

3.1.2 CNT Cathode on Silicon Wafer

For applications such as micro focus x-ray tube, we need to define the size and shape of the cathode precisely. The shadow mask method often yields irregular CNT pattern around the edge. To solve this issue, the second generation cathodes are deposited on silicon wafers with help of photolithography techniques.

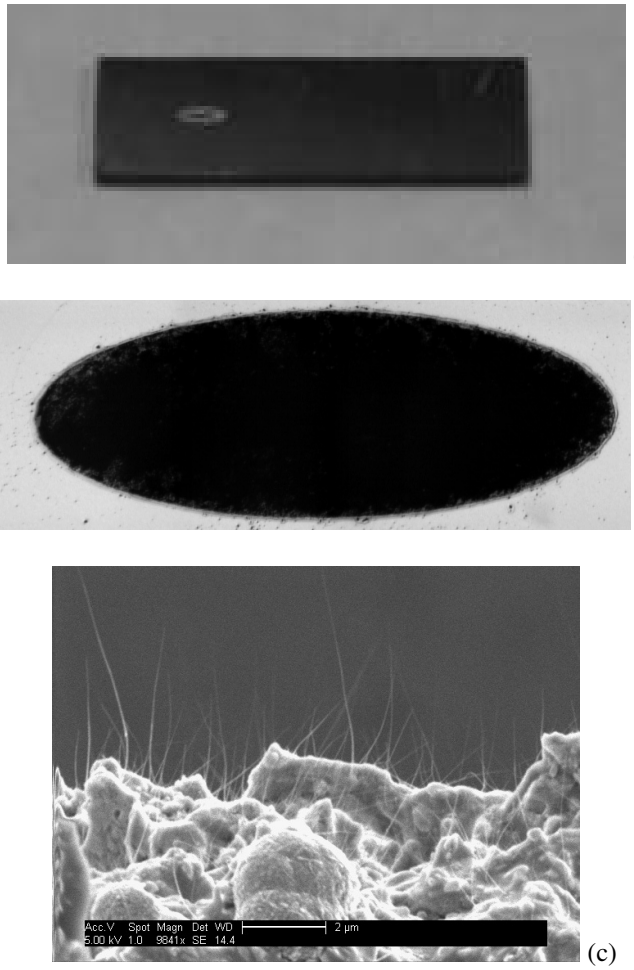

Figure 3-2: Images of cathodes on silicon wafer.

(a): One cathode on silicon wafer. The wafer size is 0.3" by 1". (b): Optical microscope image of the area containing CNTs, area size is 0.72mm by 2.5mm. (c): SEM image of the cathode after annealing and taping.

To fabricate the cathodes, we first spin-coat the SU-8 photoresist (the process can be found at www.microchem.com) thin layer on the silicon wafers. The wafers are then exposed to a UV light with pre-designed pattern. After development, only areas to deposit CNTs are open, other places are covered by SU-8 layer. For SU-8 is not soluble in ethanol, the photoresist layer serves as the mask during the EPD process. Figure 3-2 shows the wafer

cathode sample and the area containing CNTs. The CNT deposition area is well defined as seen in the optical zoom-in image. The SEM image shows that the cathode morphology is close to the ideal field emitters discussed in Chapter 2.

The standard silicon wafers are in round shape. In our facility, we are capable to fabricate wafers up to 3" in diameter. To fully utilize the wafers, we designed a pattern which contains 10 cathodes as shown in Figure 3-2. Before the electrophoresis deposition, we use the dicing saw to cut the wafer. To enhance the conductivity between the silicon wafer and the CNT emitters, a thin metal layer (normally Molybdenum) is sputtered on the silicon wafer before the photolithography. In short, the steps to fabricate the cathodes on silicon wafer are listed:

- Sputter metal layer on silicon wafer;
- Coat SU-8 photoresist pattern on silicon wafer;
- Cut silicon wafer;
- Electrophoresis deposition;
- Lift-off (remove SU-8 photoresist layer);
- Anneal and activate.

By using the photolithography technique, the cathode area is well defined. The field emission performance still has fluctuation. Figure 3-3 illustrates the field emission curves of

three random cathodes with the same size. To generate 1mA current, the voltage difference is about 200V.

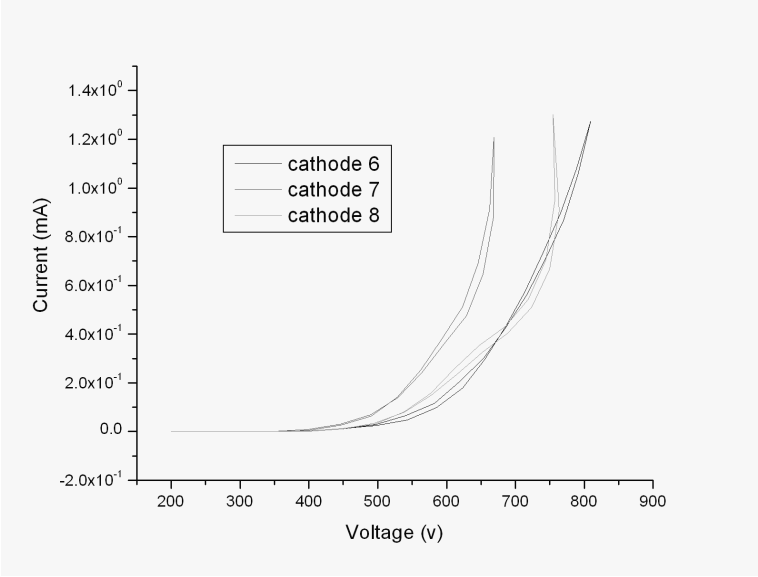

Figure 3-3: Field emission curves of three typical cathodes.

3.1.3 Parallel Fabrication

To further improve the production rate, we developed parallel fabrication process. Silicon wafers with 5μm silicon dioxide layer are chosen as the substrate. Figure 3-4 shows a sample containing three cathodes on the same wafer. The procedure is as follow:

- Coat SU-8 photoresist pattern for metal contact;
- Sputter metal;
- Lift-off photoresist;
- Cut wafer at desired dimensions;

- Coat SU-8 photoresist pattern for EPD;
- Electrophoresis deposition;
- Lift-off photoresist;
- Anneal and activate.

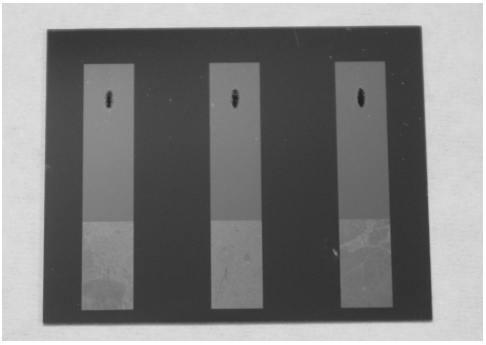

Figure 3-4: Single sample wafer containing three cathodes.

Parallel fabrication method needs two lithography steps; however, multiple cathodes are produced at once. Parallel fabrication suits the best for applications require multiple cathodes within a compact space. The consistency of the field emission performance between cathodes is better for the EPD conditions are exactly the same. Glass substrates can substitute silicon wafer to lower the cost and to provide better insulation.

3.2 Single Beam X-ray Source and Application

3.2.1 First X-ray Source and Imaging System

The first x-ray source and the imaging system in our group were built in 2002[54] by my colleagues. The schematic is shown in Figure 3-5. The x-ray source is housed inside a vacuum chamber under $1X10^{-7}$ Torr. The components are CNT cathode (on metal substrate), metal mesh gate, and tilted anode. The x-ray is switched by controlling the potential between the cathode and the mesh gate. The x-rays passing through the beryllium window are used for imaging. A hand phantom image is shown in Figure 3-6.

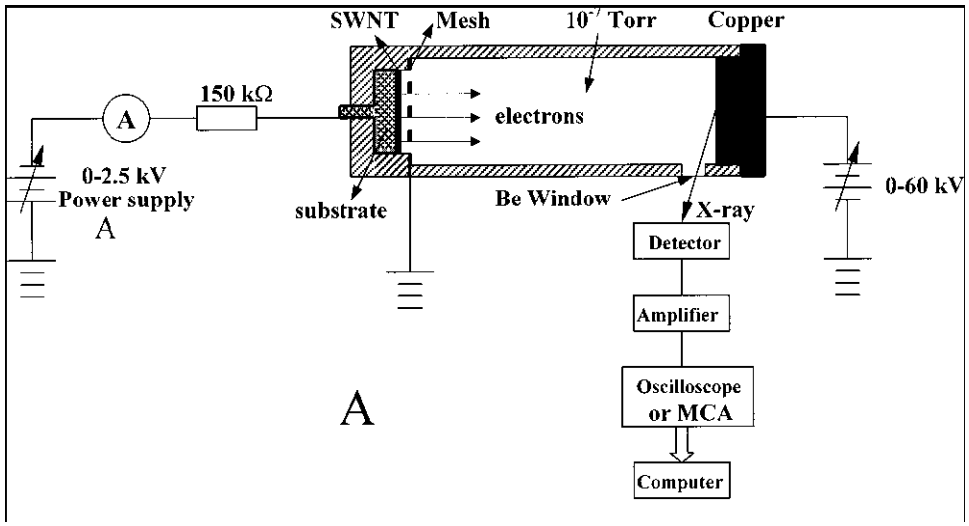

Figure 3-5: Schematic of the first imaging system using X-ray source based on CNTs.

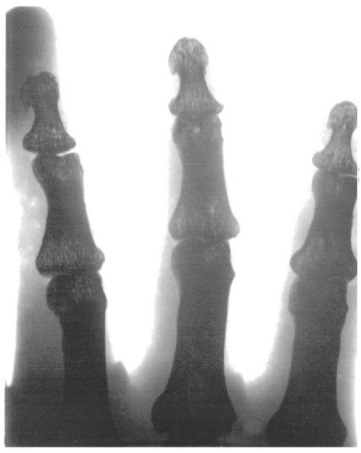

Figure 3-6: Image of a hand phantom using x-ray source based on CNTs.

Compared with conventional x-ray sources with thermionic cathodes, the CNT based x-ray source has several intrinsic advantages: (a) the source can be easily miniaturized; (b) it has high temporal resolution (up to 20 kHz has been demonstrated); (c) long lifetime and low cost due to low operating temperature.

3.2.2 Micro Computed Tomography Based on Micro-focus Tube

High-resolution x-ray micro computed tomography (micro-CT) is now routinely used for in vivo imaging in preclinical cancer studies of small animal models[55, 56]. The imaging quality of the micro-CT system is mainly determined by the spatial and temporal resolution of the x-ray source, the system geometry and the detector resolution. Our second generation x-ray source is developed mainly for the application in micro-CT.

The major improvement of the second generation source is due to the focusing electrodes. The x-ray focal spot is usually reduced by focusing the emitted electrons that impinge on the anode. Comparing to the electrostatic focusing[57], magnetic lenses offer lower aberrations and better focusing properties[58, 59]. However, the magnetic focusing unit is usually awkward in size and requires complex power control unit. In contrast, electrostatic focusing only requires one or more simple metal electrodes and can be easily miniaturized. Up to two electrostatic electrodes have been integrated into the second generation x-ray source based on CNTs while two-electrode design yields the best focusing result.

The detailed drawing with the design and the dimensions of the focusing lenses is shown in Figure 3-7. Focusing electrodes 1 and 3 were made of planar metal diaphragms. The central focusing electrode 2 was in the shape of a truncated cone, which played the role of harnessing the divergence of electrons coming out of the gating grid, and thereby pre-focusing the electrons into more parallel shape before they reach the final focusing electrode. Theoretical simulation results indicate that asymmetrical Einzel-type lenses with a middle conical electrode with a cone angle of $2 \tan^{-1}(1/2)$ possess the smallest spherical aberration in focusing electrons[60]. In the present design, focusing electrode 1 was placed at the same potential as the gate electrode, and focusing electrodes 1, 2, and 3 have independently

controllable potentials. This is different from the original design of the Einzel lenses which apply the same potential for focusing electrodes 1 and 3.

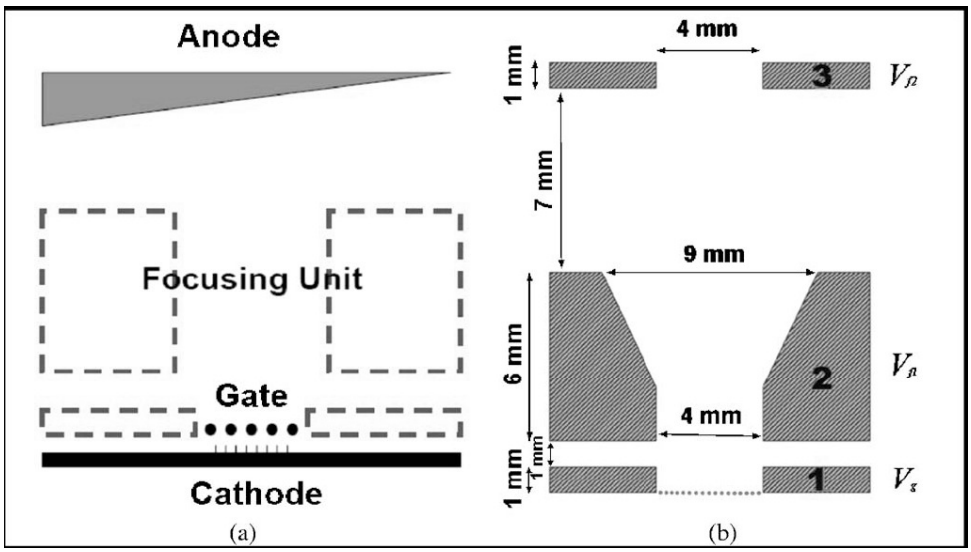

Figure 3-7: Schematic of field emission x-ray source based on CNTs.

(a): Schematic of a carbon nanotube based microfocus x-ray source that consists of cathode, gate, focusing electrodes, and anode. (b): Cross-sectional view of the focusing unit of the x-ray source.

The design of the focusing lenses was optimized by simulating the trajectory of the field emitted electrons through the combined electrical fields among electrodes using a commercial software package Lorentz-E. Figure 3-8 shows the relation between the cathode diameter and the focal diameter of the electron beam on the anode obtained from the simulation. The result reveals that the focusing system is very linear in focusing electrons emitted from cathodes with the diameter ranging between 0.1 and 2mm. The insets of Figure 3-8 (a) show the profiles of the simulated electron trajectories. In the simulation, the cathode was grounded and the anode voltage was set at 40 kVp. Based on experimental result, a

divergence angle of 4° was applied for electrons passing through the gating grid. Simulation results showed that a demagnification of about 6 was achieved in the current x-ray tube design. The linearity of the designed focusing system provides flexibility in varying the size and geometry of the x-ray focal spot.

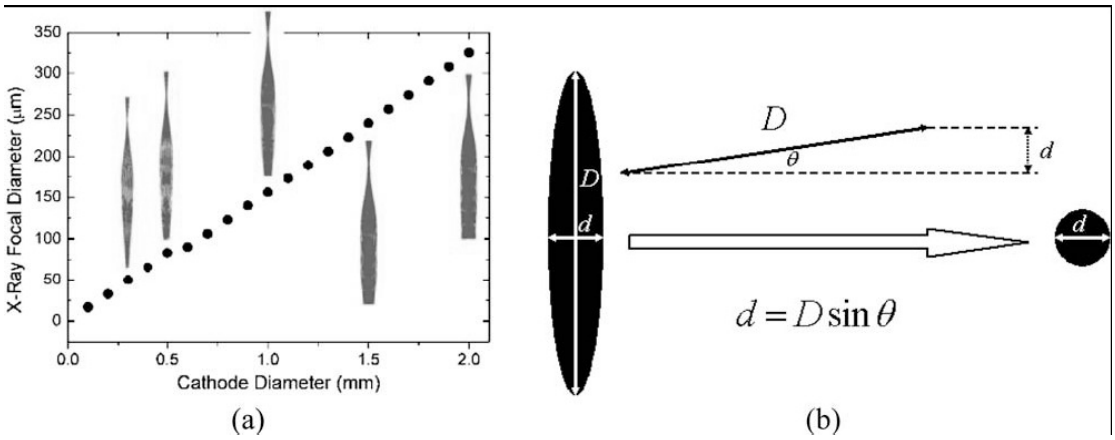

Figure 3-8: Simulation of focal spot sizes of different cathode geometries.

(a) Electron optics simulation results demonstrating the linearity and magnification of the X-ray focusing system using the modified asymmetrical Einzel lenses. Insets show the electron trajectories for selected cathode diameters. (b) Schematic illustrating the formation of an isotropic effective focal spot on the projected plane with the anode take-off angle of θ.

An elliptical shaped CNT cathode was used to achieve an isotropic effective focal spot size as schematically shown in Figure 3-8 (b). The cathode was fabricated using silicon wafer for well defined CNT deposition area. The x-ray focal spot size was measured following the European standard (EN 12543-5)[61], where the resolution is obtained based on the line profiles of the transmitted x-ray intensity of a 1mm diameter tungsten wire phantom in two orthogonal directions. The x-ray image is captured using a flat panel detector (Hamamatsu C7921CA-02) with 50μm resolution. To satisfy the conditions set by the standard, the wire

and flat panel detector were placed 12 and 120 cm apart from the x-ray source, respectively. The potentials applied to focusing electrodes 2 and 3 were adjusted to optimize the focusing effect. The best result was obtained when the two potential were at 350V and 2100V, respectively, which is consistent with the simulation results. The measurements also showed that changing the gate voltage did not cause any significant change of the focal spot size (less than 1%). This is important for practical device applications because over the lifetime of the x-ray tube the gate voltage will increase to maintain the constant emission current/flux.

The x-ray projection image of the tungsten wire phantom measured after optimizing the focusing optics is shown in Figure 3-9 (a). The diameter of the x-ray focal spot was calculated to be 30±5μm from the line intensity profiles of the cross wire shown in Figure 3-9 (b). The focal spot demagnification factor is about 5, which is calculated from the ratio of the cathode size (150μm) and the true focal spot diameter. This is consistent with the value predicted in the simulation. No change in the focal spot size was observed during the course of the imaging experiments (~20 h). The resolution of this isotropic x-ray source was further demonstrated by imaging a modulation transfer function phantom as shown in Figure 3-9 (c), where a geometrical magnification of 1.6 was used. Resolution up to 13 lp/mm was clearly resolved as seen in the inset of Figure 3-9 (c). By setting the anode voltage at 40 kVp and using an exposure of 0.1mAs/image, an adult mouse injected with barium contrast agent before sacrifice was imaged in our CNT based micro-CT scanner. The source to object and

source to detector distances were set at 20 and 32 cm, respectively, which results in a geometrical magnification of 1.6 for mouse imaging. Figure 3-9 (d) shows a projection image of the mouse, where the aorta of the heart is clearly revealed as pointed by the arrow.

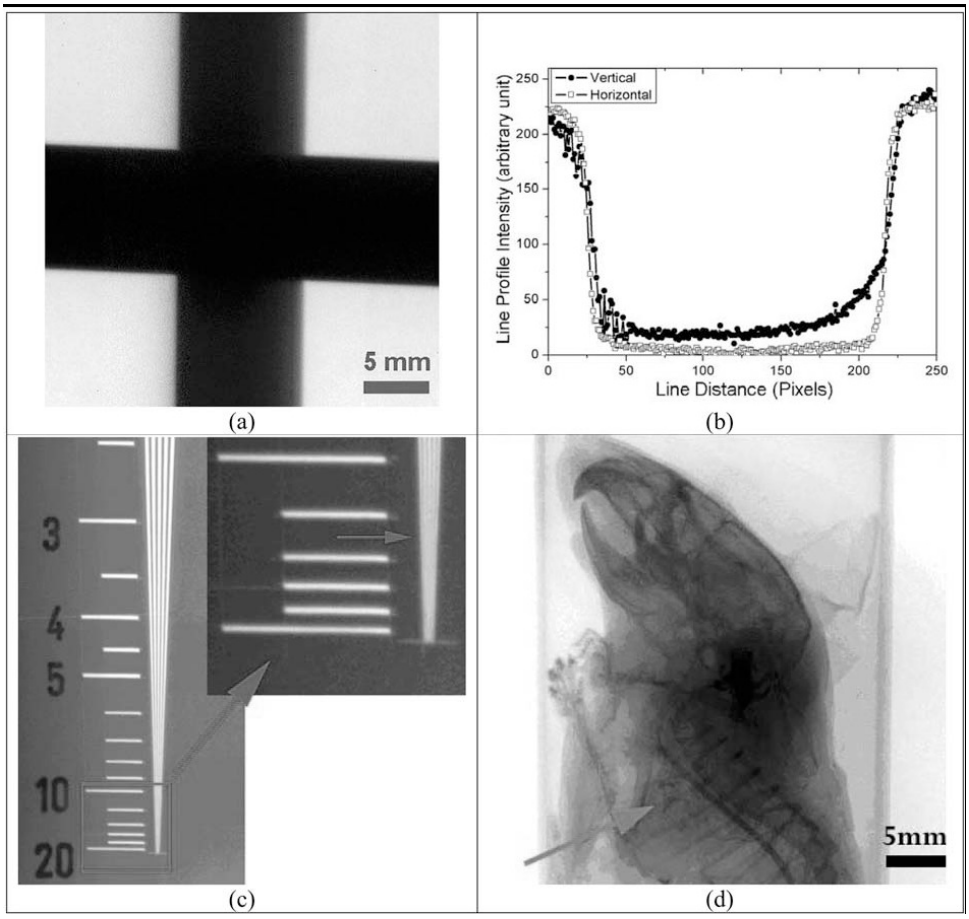

Figure 3-9: Calibration and imaging test of single beam x-ray source based on CNTs.

(a): X-ray projection image of a 1mm tungsten wire phantom. (b): The line intensity profiles crossing the horizontal and vertical tungsten wire in (a). The focal spot was measured to be about 30 μm. (c) X-ray projection image of the Cardinal Health phantom. Resolution up to 13 lp/mm was resolved. (d): Projection image of a sacrificed mouse injected with contrast agent. The arrow points to the aorta of the mouse heart.

In summary, the micro-focus x-ray source with high spatial resolution, temporal resolution, and stable emission has been demonstrated. The system performance is

comparable to micro-CT imaging protocols with a fixed-anode thermionic x-ray source operating at similar resolution[62]. Although x-ray tubes with an effective focal spot size of less than 10μm are now commercially available, in practice the imaging resolution is constrained by motion-induced blur in live objects. For un-gated micro-CT imaging of live mice, prior experiments have shown that the imaging artifacts due to respiratory and cardiac motions may completely obscure the anatomical details within the region of lung and heart[63]. Motion-induced artifacts can be reduced by gating the x-ray exposure in synchronization with physiological signals. Thanks to the high temporal resolution, the CNT based field emission x-ray tube has intrinsic advantages over the conventional x-ray tubes with thermionic cathodes for gated micro-CT imaging. We expect that the gated micro-CT scanner based on the CNT field emission x-ray source will further increase the system performance.

3.3 Multi-Beam Field Emission X-ray Source

In many x-ray imaging applications, such as computed tomography[64] and tomosynthesis[65], multiple projection images from different angles are required to reconstruct the three-dimensional object. In most of the current tomographic scanners, a single x-ray tube is mechanically rotated around an object (or rotate the object while keep the

x-ray tube stationary) to collect the multiple projection images. The mechanical movement is the bottle neck of the image acquisition process.

To improve the imaging speed, several novel x-ray source designs have been proposed and some have been tested. One is the electromagnetically scanned x-ray source used in the ultra-fast Electron Beam CT scanner[66] and some PCB inspection systems. In this case, like the design of a cathode-ray-tube, an electromagnetic field steers the electron beam to different locations on the x-ray anode to produce a scanning x-ray beam[67, 68]. Such x-ray tubes are in general large and costly. The range of viewing angles is limited by the efficiency of the electromagnetic field to bend the high energy electrons. An alternative method to generate a scanning x-ray beam is to use as many cathodes as the number of x-ray focal points required, where each cathode sends an electron beam to the corresponding focal point it directly faces. The design of a multi-beam x-ray source with multiple thermionic cathodes was disclosed in the patent literature[69]. However, the only devices following this design are the dynamic spatial reconstructor[70] built by Mayo clinic in 1980s. Due to the difficulties of packaging and controlling the thermionic cathode array, only two DSRs are built so far and are not suitable for clinical applications. On the other hand, the field emission x-ray source based on CNTs can be easily miniaturized. Based on the single beam introduced in last section, we built the first multiple beam field emission x-ray sources (MBFEX).

3.3.1 MBFEX Design

The MBFEX source comprises a field emission cathode with a linear array of five CNT field emission cathodes, focusing electrodes, and a molybdenum anode, as illustrated in Figure 3-10 (a). The entire setup was housed in a vacuum chamber with a 4" diameter beryllium x-ray window at a base pressure 10^{-7} Torr. Detailed structure of each individual x-ray unit was shown in Figure 3-10 (b). The cathodes are on metal cylindrical substrates by electrophoresis using CNTs synthesized at Xintek. All the gate electrodes were electrically connected. One active electrostatic focusing electrode was placed between the gate electrode and the anode for each pixel. Each emitting pixel was connected to the drain of an n-channel MOSFET (metal oxide semiconductor field effect transistor), the source of which was grounded. The gate of the MOSFET was connected to the output of a digital I/O board which can provide 5V DC voltage signal.

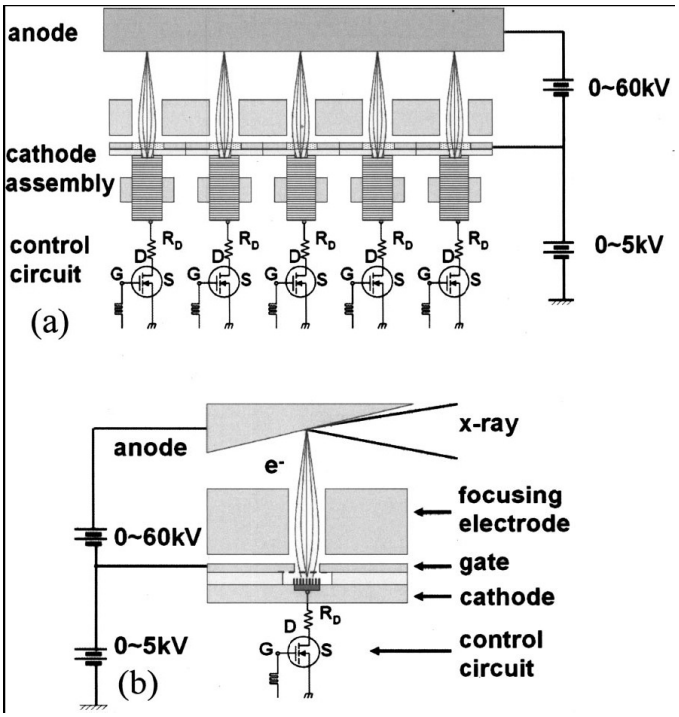

Figure 3-10: 5-beam x-ray source array.

(a): A schematic of the multi-beam x-ray source with a field emission cathode that contains five emitting pixels and a Mo target at 10^{-7} Torr pressure. The pixels were evenly spaced with a center-to-center spacing of 1.27 cm. Each pixel is capable of emitting 1 mA current. The anode voltage is set at 40 kV. The gate voltage varies depending on the flux required. Switching the x-ray beam from each pixel is controlled by sweeping a 5 volt DC pulse through the MOSFET. (b): Each emitting pixel comprises 1.5 mm diameter CNT film coated on a metal substrate, a 150-μm thick dielectric spacer, an extraction gate, and a focusing electrode.

3.3.2 MBFEX System Performance

The field emission characteristics of the individual pixels were measured under the triode mode in the x-ray chamber. The measured threshold field for 1mA/cm^2 current density is between 2.3-3.1 V/μm. Emission current density of ~1A/cm^2 was achieved at higher fields. To minimize the current fluctuation and decay, and to reduce pixel to pixel variation, an

electrical compensation loop was incorporated to automatically adjust the gate voltage to maintain a constant pre-set emission current. Figure 3-11 (a) shows the experimentally measured emission currents and the corresponding gate voltages from the five pixels recorded over 30 minutes period under the constant current mode (100% duty cycle). The set emission current was 100A and anode voltage was 40 kV. No arcing was observed after initial conditioning.

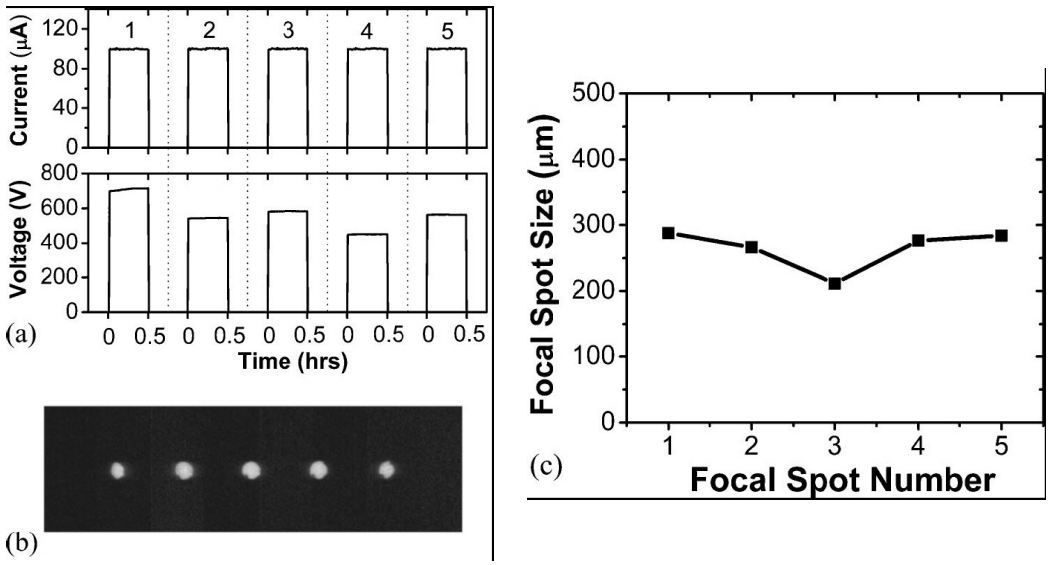

Figure 3-11: Calibration of 5-beam x-ray source array.

(a): Emission current measured from the five pixels recorded over 30 minutes period under the constant current mode using 100% duty cycle. The set emission current was 100 μA and the anode voltage was 40 kV. (b): Pin-hole measurement showed five evenly spaced focal spots on the target. (c): The focal spot size was determined based on the European Standard EN 12543-5. All of the five focal spots are in the range between 200 μm to 300 μm in diameter under same focusing voltage V_f=900 V.

The x-ray focal spots from the five pixels on the cathode were recorded by pinhole measurement and are shown in Figure 3-11 (b). Due to the large diameter (>1mm) of the pinhole used in the experiment the actual focal spot sizes can not be extracted from the

image. However it does show that the five focal spots are evenly spaced on the target surface. The noncircular shape of the spots on each end is due to the oblique projection angle of the corresponding pixel. The focal spot sizes were determined by measuring the radiographs and analyzing the intensity distribution of a thin metal wire in two orthogonal directions. The measured actual focal spots (diameter on the anode) are plotted in Figure 3-11 (c) for voltages V_f=900 V.

To generate x-ray radiation, a constant DC voltage (40-60 kVp) was applied to the anode and a variable DC voltage (<1kV) was applied to the gate electrodes. The MOSFET circuit, as illustrated in Figure 3-10, was used to switch on and off the emission current from the individual pixels. To activate a pixel, a 5V signal was applied to open the channel of the corresponding MOSFET such that the cathode formed a complete electrical circuit with the gate electrode. Electrons were emitted from this activated pixel when V_g was larger than the threshold value for emission. They were accelerated by the V_a and bombarded on a directly opposing area on the anode to produce x-ray radiation. Other pixels would not emit electrons because of the open circuit. To generate a scanning x-ray beam from different origins on the target, a pulsed controlling signal with pre-determined pulse width was swept across the individual MOSFETs. At each point, the channel was “opened” to generate an electron beam from the particular pixel which produced an x-ray beam from the corresponding focal point on the target.

3.3.3 Imaging Test

Projection images of a phantom placed 15 cm away from the effective focal spots were taken from different projection angles using this MBFEX source. The phantom was a blade from a surgical scalpel placed behind a metal rod. V_a was fixed at 40 kV. A digital area x-ray detector (Hamamatsu C7921) running at 16 frame/second was used to record the image. The phantom to detector distance was 10 cm. The five pixels were turned on sequentially for 5 seconds each. The gate voltage was adjusted to maintain a 25 μA emission current from each pixel. The detector was on during the entire process. Figure 3-12 shows the five projection images of the object phantom formed by the x-ray beams from the corresponding focal points. As expected, the blade invisible in the central projection image (image 3) was clearly identified from other viewing angles due to the spatial extension of the cathode array. Here the acquisition time is only determined by the required x-ray exposure time since no mechanical motion is needed and the electrical switching time is negligible.

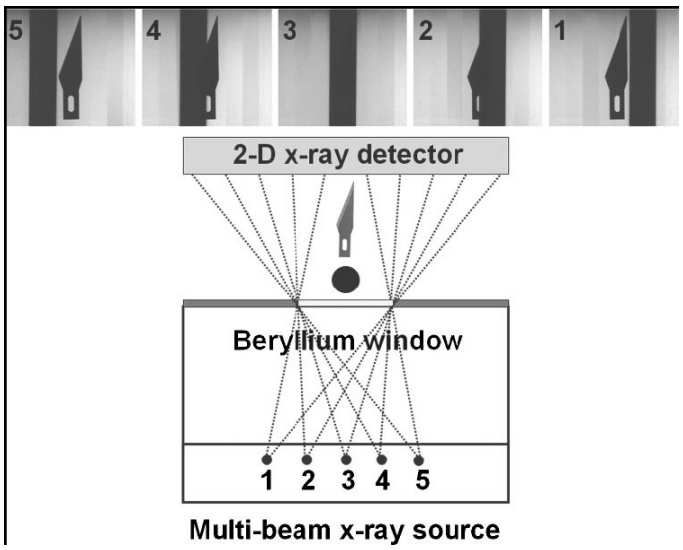

Figure 3-12: Imaging test using 5-beam x-ray source array.

Five projection images of the same blade-metal rod phantom from different viewing angles were taken by the MBFEX. The digital 2D X-ray image sensor (Hamamatsu C7921) has a 1056x1056 photodiode array with 50x50 μm pixel size. It was operated at 16 frames-per-second (fps) with 4x4 binning. The imaging conditions are: 40 kVp anode voltage, 25 μA tube current, and 5 second exposure time. The source to object distance is 15 cm and the blade is placed close to the x-ray detector.

Another set of projection images of a computer board was taken to demonstrate potential tomosynthesis applications. Figure 3-13 (a) shows one of the five projection images, which is a superimposed image of several overlapped circuit planes. Original projection images were processed using mathematical algorithms developed for multilayer tomosynthesis[2]. From the tomosynthesis images in Figure 3-13 (b) and (c), it is very clear that different layered structures have been separated. In Figure 3-13 (c), the original thick wire shown in the Figure 3-13 (a) was blurred out and structures underneath that wire clearly showed up. However, only limited geometrical resolution in the direction of x-ray beam, called axial resolution, can be achieved due to the fact that there are only five scanning

beams providing limited viewing angle. The axial resolution can be further improved with increasing projection angle and number of scanning beams.

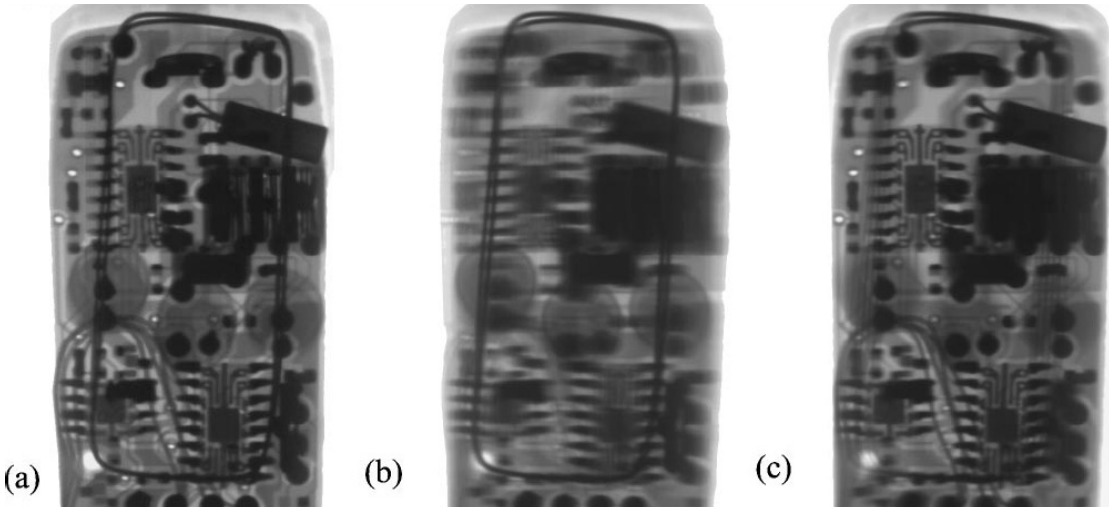

Figure 3-13: Tomysynthesis test using 5-beam x-ray source array.

(a): One projection image of a computer board containing several overlapped circuit planes. (b) & (c): Two reconstructed tomosynthesis images showed different layers of the circuit board. It is very clear that the original thick wire on the top layer of the circuit board was removed in Fig. (c). Limited axial resolution is due to the fact that there are only five scanning beams providing limited viewing angle.

3.4 Multiplexing Using MBFEX

Using the MBFEX sources, multiple x-ray images can be obtained without mechanical movement. However, those images are still taken sequentially. If projection images from different sources can be captured simultaneously, the imaging process will be greatly shortened. Multiplexing technique[71], as demonstrated in communication devices and certain analytical instruments[72, 73], can dramatically speed up the signal transfer process. However, this technique has not been applied to x-ray radiography, partly due to limitations

of the x-ray source technology. Here in this section, the multiplexing x-ray imaging technique will be demonstrated by using the MBFEX.

3.4.1 Orthogonal Frequency Division Multiplexing (OFDM)

The experiment was carried out using the orthogonal frequency division multiplexing (OFDM) algorithm[74] in a configuration illustrated in Figure 3-14. The x-ray source comprises a linear array of nine field emission cathodes. Activation and modulation of the x-ray radiation were achieved by programming the input voltage pulse train applied to the gate of the MOSFET circuit connected to the cathode. The radiation from a particular pixel was switched on and off when the input at the corresponding MOSFET gate was 5V and 0V, respectively.

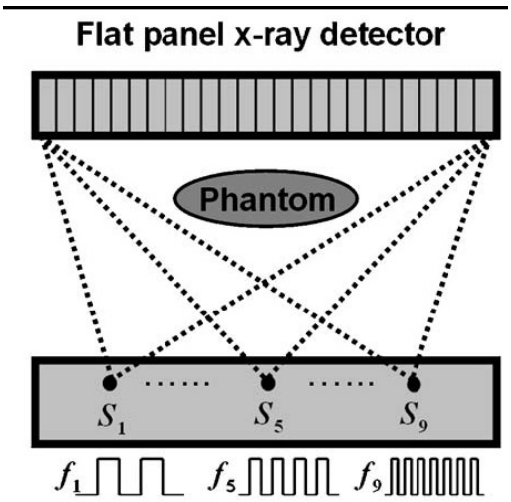

Figure 3-14. Schematic of the multiplexing imaging.

The imaging and data processing procedures are illustrated by the flow chart in Figure 3-15. Let's start with the simplest case with two x-ray sources. The two sources are tuned to produce x-ray with different frequencies: f_1 and f_2. The detector captures a serial of multiplexed images with certain frame rate. These images contain information from both sources. To obtain the information from single source (projection image only using one source), the de-multiplexing process is needed. This is a pixel based process. For a certain pixel on the detector, the intensity profile in time domain is first extracted. The power spectrum of the district Fourier Transform is simply the summation of the spectrums of two sources. The power spectrum value on each of the separated curve at frequency f_i is the square of the intensity value of the projection image. After repeat the calculation for all pixels, we can reconstruct the two projection images.

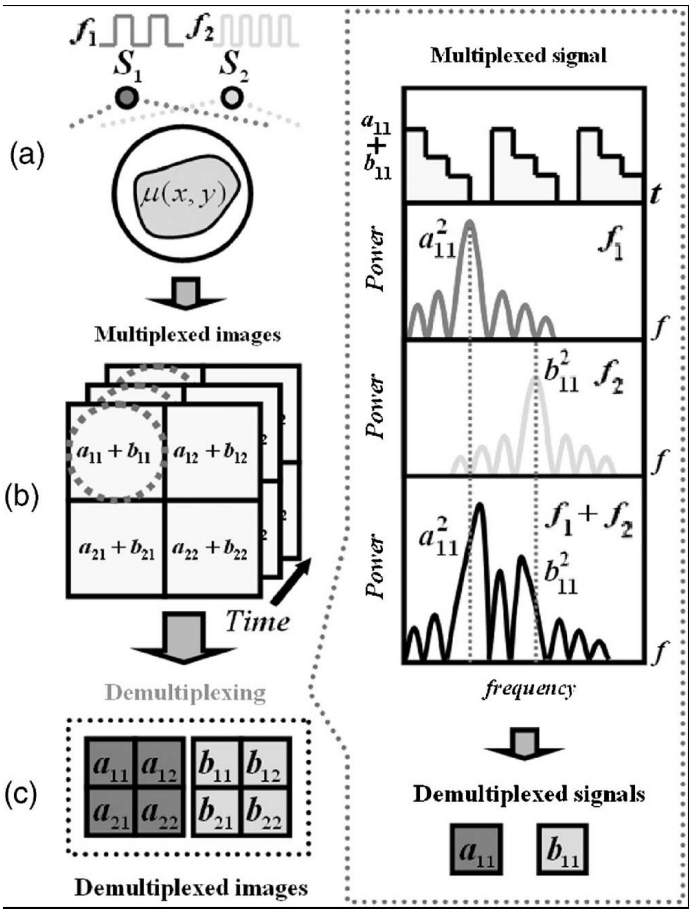

Figure 3-15: The flow chart for the OFDM radiography experiment.

(a): The two incident x-ray beams have two distinct pulsing frequencies, f_1 and f_2. They transmitted through the phantom and formed a multiplexed x-ray signal including both frequency components. (b): The multiplexed images were recorded by a single flat panel x-ray detector which collects the transmitted x-ray intensity as a function of time over certain period T. (c): DFT algorithm is used to de-multiplex the composite x-ray signals recorded by a pixel. The projection images can be achieved by repeating the de-multiplexing procedure for all the pixels.

It is noticeable that the only required information for reconstruction is the value at frequencies f_i. However, overlapping intensity contributions from the primary and higher harmonics of the input signals and their ripples in the Fourier spectrum introduce imaging artifacts due to inter-channel interferences. This is called "crosstalk" between sources. By carefully choosing the system parameters, including frequencies and total frames, the

crosstalk can be reduced to zero. So, we can reconstruct the projection images only from the original power spectrum. In our system, the reduction of crosstalk is realized by orthogonal frequency division multiplexing (OFDM).

All the x-ray pixels were activated simultaneously for 10 seconds with every beam illuminated the entire object, as illustrated in Figure 3-16 (a). Each x-ray beam has a square waveform with a 50% duty cycle and a unique frequency f_i. The choice of f_i was complicated by several factors that affect the imaging quality. Although sampling at twice the Nyquist frequency can ensure the correct measurement of f, the detector frame rate (f_d) needs to be sufficiently faster than the highest pulsing frequency f_{max} to obtain the correct waveform. In the present experiment, the detector works at 16 fps (f_d >10 f_{max}). The crosstalk was eliminated by setting the bandwidth $f < 2f_{\min}$ (the second order harmonic is zero for 50% duty square wave) and by using nine orthogonal frequencies[71] in the range between 0.5 Hz and 1.3 Hz with an interval of 0.1 Hz. The frequency increment is determined by $1/T$. The simulated result in Figure 3-16 (b) shows that the crosstalk is essentially zero.

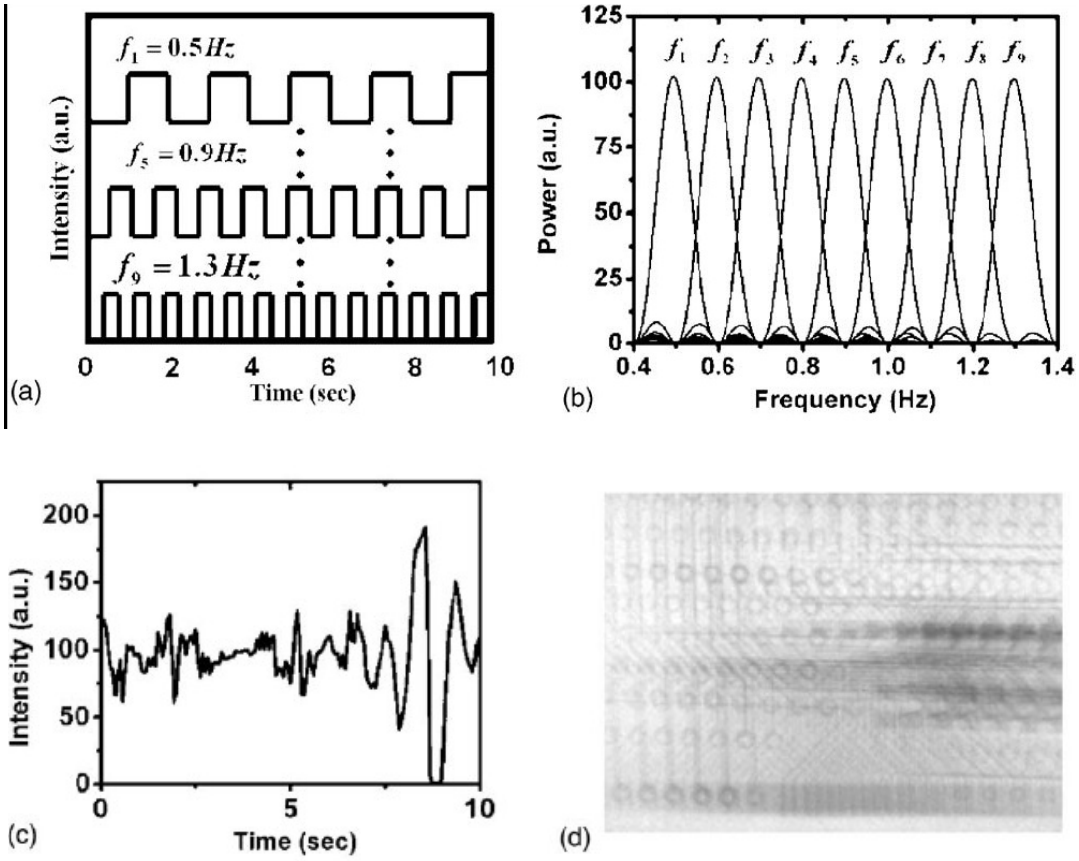

Figure 3-16: Intensity at time domain and frequency domain.

(a): Schematic showed that nine x-ray pixels were running at frequencies ranging from 0.5 Hz to 1.3 Hz with 0.1 Hz frequency separation. (b) In frequency domain, the simulation demonstrated that, at the central frequency of each subcarrier, there is no crosstalk from other subcarriers due to the orthogonality of the signals. (c): The transmitted X-ray intensity vs. time curve recorded on one detector pixel. (d): One frame of a normal multiplexed X-ray image of the computer board.

3.4.2 Imaging Results

A computer board was imaged using the OFDM method. The transmitted x-ray intensities (I) were recorded as a function of time (t). A total of 160 multiplexed images were collected in 10 seconds. Due to the large number of overlapping waveforms, the *I vs. t* curve

of each detector pixel appears to be random, as the example shown in Figure 3-16 (c). Figure 3-16 (d) illustrates one frame of the multiplexed images, which shows no apparent information of the object being imaged as expected due to superposition of projections from the different angles.

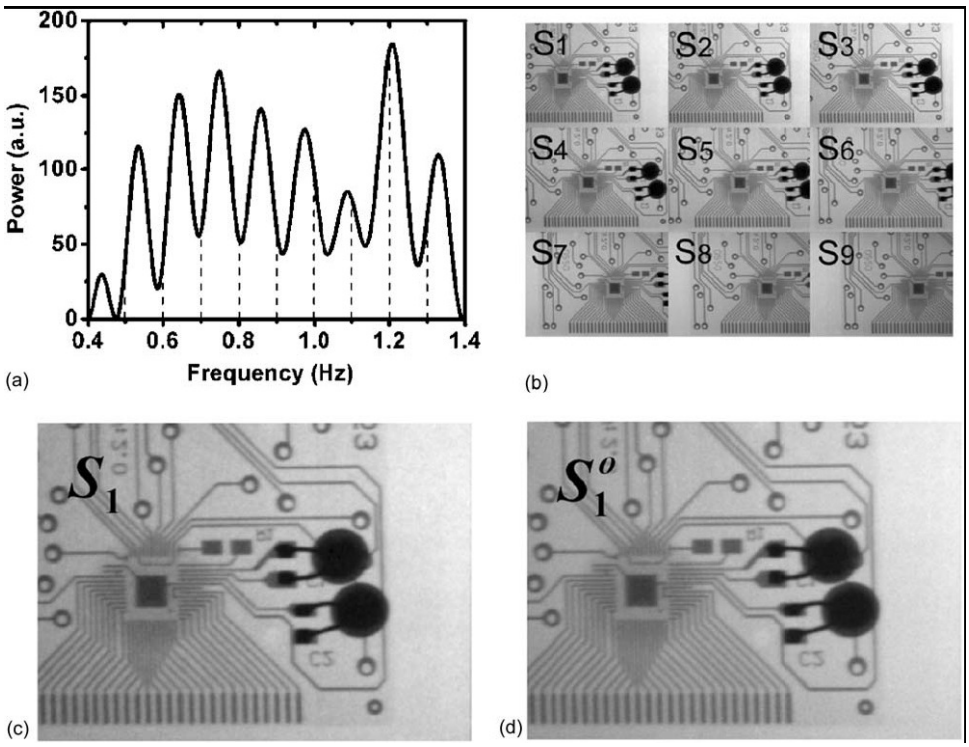

Figure 3-17: Multiplexing imaging reconstruction.

(a): The DFT based algorithm was applied for de-multiplexing. (b): Nine de-multiplexed images corresponding to nine frequency channels were obtained by the OFDM scheme showing the circuit board from different viewing angles. (c): One of the de-multiplexed images of the circuit board from the x-ray pixel S_1. (d): A projection image taken using only the x-ray pixel S_1 with the same dose and geometry as in (c). The difference between the two images is visually negligible.

Although structures were observed in the corresponding power spectrum (Figure 3-17 (a)) from Discrete Fourier Transform (DFT), the peak positions were not related to the

frequencies of the input signals. By de-multiplexing the x-ray signals pixel by pixel across the entire detector, clear projection images of the object from the 9 viewing angles were extracted and are shown in Figure 3-17 (b). No visible imaging artifact was observed.

To assess the quality of the images obtained by multiplexing, a de-multiplexed image S_1 (Figure 3-17(c)) was compared to a reference image $\boldsymbol{S}_1^o$ (Figure 3-17(d)), which was taken using the same x-ray pixel under the same imaging conditions (kVp, mAs, and geometry) without using multiplexing/de-multiplexing technique. The two images appear to have the same contrast and spatial resolution. No visual difference was detected. More quantitative analysis shows that the intensity deviation between the two sets of data was less than 3%. The difference can be attributed to the intensity fluctuation of the x-ray beams which is estimated to be around 1%, drifting of the detector sampling rate (around 0.1 fps) and insufficient data sampling due to the limitation of the x-ray detector. Separate simulation has shown the improvement of the image quality with increased detector sampling rate.

3.4.3 Further Discussion

Compared with sequential imaging, multiplexing generates more scattered photons because multiple x-ray beams illuminate the sample simultaneously. The contribution of the scattered photons from different x-ray beams, however, can be separated in the de-

multiplexing process because they have the same modulation frequencies as their corresponding primary beams. As a result, the additional scattering intensity does not contribute to the noise level in the de-multiplexed images. In practice, however, the use of multiplexing requires redesign the anti-scattering grid which is commonly and effectively used in many medical imaging systems.

The multiplexing imaging speed in this study is limited by the maximum frame rate of the area detectors which are usually less than 50 fps at present. In the present experiment using the OFDM scheme the imaging time for the nine projections was 10 seconds. If sequentially taking one image at a time, it would require a total of 45 s with the same x-ray peak power at 100% duty cycle (5 s per image for the same x-ray dose). In general a factor of $N/2$ (N=total number of images) increase in the speed can be achieved using the OFDM scheme. This becomes significant when N is large. As an example, clinical CT scanners acquire ~1000 images per gantry rotation. On the other hand, if the total imaging time and x-ray dose are kept the same as used in the sequential process, then the x-ray peak power, i.e., the tube peak current, can be reduced by a factor of $N/2$ by multiplexing because the exposure time per image is now longer.

Chapter 4: Digital Breast Tomosynthesis Using Multi-Beam X-ray Source Array

4.1 Background

Breast cancer is one of the leading killers for women. In 1998, about 179,000 women in the U.S. were diagnosed with breast cancer and 43,500 women died of the disease[75]. Approximately, 12% of women in the U.S. develop breast cancer during their lifetime and 30%-40% of whom die of it[76]. Although tremendous research has been done, the causes of breast cancer are still largely unknown. Due to this reason, means to prevent breast cancer is not available currently. However, several techniques have been developed and approved effective in early detection of breast cancer. Among them, mammography, the most effective one, has been shown to reduce the mortality by 30%-50%[77].

4.1.1 Screen-Film Mammography

Screen-film mammography was first developed in 1960s and is still the most popular type of mammography devices. As defined by the name, screen-film mammography utilizes

films to acquire the x-ray images. A commercial mammography device made by GE is shown in Figure 4-1. The device contains three parts: the x-ray generator, the breast compress plates, and the film plate. Due to the low contrast feature of the breast, a low-energy x-ray spectrum is preferred. A typical x-ray tube for mammography runs at 26-30kVp with molybdenum anode. Additional molybdenum filtration may be added. The breast under examine is normally compressed to spread the tissues apart and to reduce the patient movement. To improve image quality, an anti-scattering grid may be used. Projection images from one or more angles are taken for screening or diagnosis.

Figure 4-1: Screen-film mammography device made by GE.
Picture source: General Electric website.

As a fully developed technique, screen-film mammography has many advantages comparing to other new techniques, such as MRI and ultrasound:

- Low cost.
- High spatial resolution: over 20 lp/mm.
- Convenient display using view-box technology.

However, in screen-film mammography, the film must act as the x-ray detector, as well as the image storage and display device. The inefficient accessibility is a huge disadvantage as other technologies advanced, such as image display and digital file transferring. The dynamic range and the contrast characteristics also need to be improved.

4.1.2 Full Field Digital Mammography

Full field digital mammography has been the trend to replace the screen-film mammography in recent years. Digital mammography has shown better performance for women younger than 50 and women with dense breasts[78]. Digital flat panel x-ray detectors instead of screen-films are used to capture the x-ray images. Different types of detectors, such as CCD based and amorphous selenium direct conversion detector, have been applied in digital mammography devices. Digital detectors generally have wider dynamic range. When stored in computer memory, the images can be processed and displayed simultaneously. Post-exposure imaging process can optimize the image contrast and quality. Remote diagnosis and computed-aided diagnosis are also possible with digital mammography. Up to date, more than 10% mammography devices in the U.S. are digital models.

4.1.3 Digital Breast Tomosynthesis

Even with recent advances in mammography, the false diagnosis rate is still about 20%. This includes both false negative (cancer not detected) and false positive (patients will be call-back for extra mammography examines). The main reason of false diagnosis is the overlapping tissues. Conventional mammography projects the 3D breast into a 2D image. When tumors and normal breast tissues superimpose on the image, false negative diagnosis may occur. The false diagnosis rate can be significantly reduced by acquiring 3D information of the breast. Two methods based on digital tomography have been proposed: breast CT and digital breast tomosynthesis (DBT), while the latter is more promising.

Up to date, three types of DBT systems by GE[79], Siemens[53], and Hologic[80] are under investigation. All three systems are based on full field digital mammography systems. The gantry rotates 15 to 50 degrees around the breast while 11 to 49 projection images are taken. Figure 4-2 shows the schematic of the designs. Due to the limited angle coverage, only in-plane (parallel to detector) images at different depths are reconstructed. The axial resolution is about 1mm and the in-plane resolution is 100μm or so.

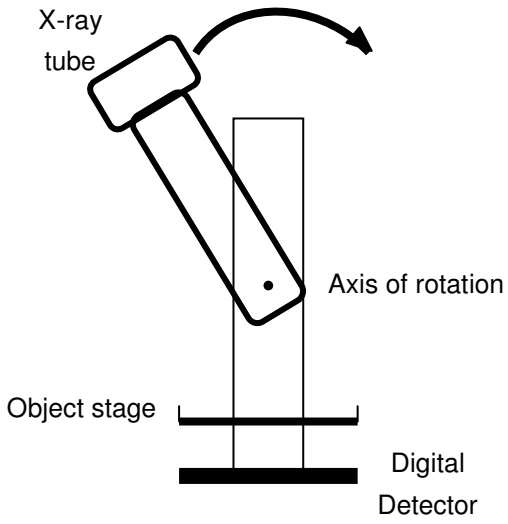

Figure 4-2: Schematic of DBT system based on full field digital mammography devices.

These three DBT systems based on rotating gantry design have shown great potentials. However, several potential problems can not be resolved easily. The imaging time (7s to 40s) is longer than regular mammography (about 1s). This produces more patient motion blur and degrades the overall image quality. A typical imaging timing diagram of DBT systems using rotating gantry design is shown in Figure 4-3. The x-ray radiation only takes a small portion (<10%) of the total imaging time. The bottle neck to reduce the total time is the physical rotation of the gantry. However, a gantry with faster rotation speed will not only dramatically increases the total cost of the system, but also induces a larger x-ray focal spot size.

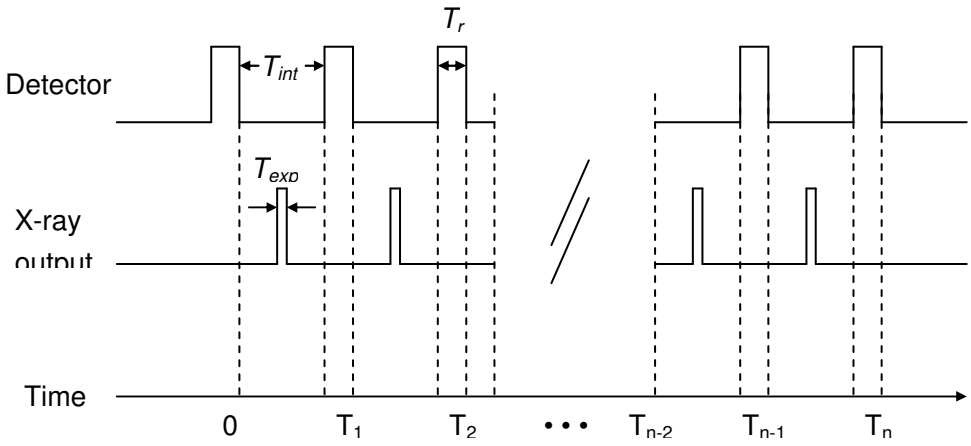

Figure 4-3: Imaging timing diagram of a typical DBT system.

X-ray exposure, T_{exp}, occurs within the integration window, T_{int}.

Currently, the DBT systems use the common C-arm gantry. Two rotation protocols have been developed. GE adapted the step-and-shoot method, which requires full stop of the gantry before each image acquisition. In this design, the gantry experiences high acceleration and deceleration in each imaging cycle, and tremendous gantry vibration is induced. Siemens and Hologic designed the continuous rotation method, which maintains constant rotation speed while x-ray images are taken. This design enlarges the effective focal spot size along the gantry rotation direction by about 1mm and the image quality is degraded. The schematic of the enlarged focal spot size is illustrated in Figure 4-4.

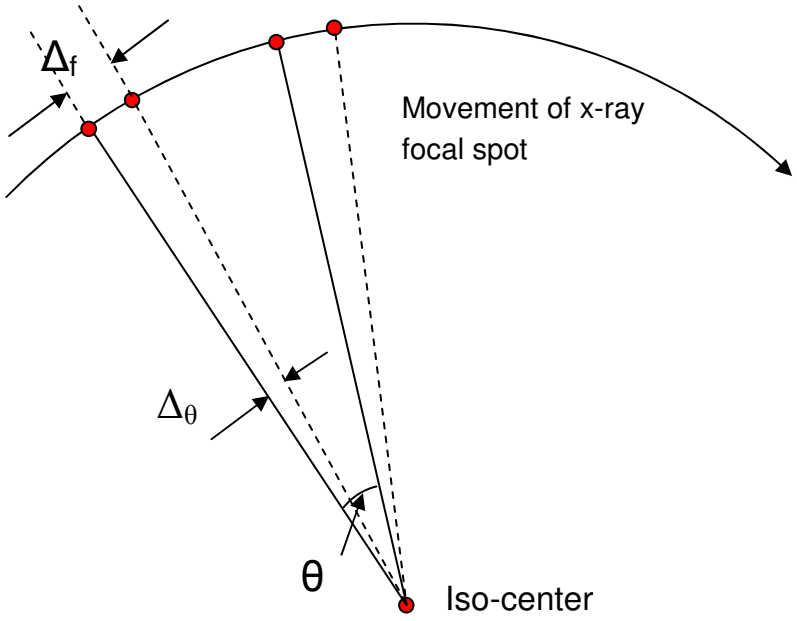

Figure 4-4: Focal spot blurring due to gantry rotation.

Based on Siemens system (Imaging mode: full resolution without lag correction). Between nearest views, the gantry rotates angle of $\theta=2°$. The gantry rotation is $\Delta_\theta=0.08°$ during each x-ray exposure. The x-ray focal spot blurring due to rotation is $\Delta_f=0.8$mm.

As the gantry rotation speed and the x-ray power reach their limit, the room to reduce the total imaging time and to improve image quality is small. Alternatively, if the x-ray images can be acquired without gantry rotation, the imaging time could be reduced. The concept of non-rotating gantry medical imaging systems using spatially distributed x-ray sources have been proposed and some developed including the Dynamic Spatial Reconstructor (DSR) developed at the Mayo Clinic [70], the electron-beam CT (EBCT) [81], and scanning beam digital x-ray (SBDX) [82, 83], as illustrated in Figure 4-5. The DSR system uses ~30 individual x-ray tubes mounted on a gantry around a patient to collect the

images. Although high temporal resolution has been demonstrated for cardiac imaging, the cost, size, and maintenance related issues make the design prohibitive. Recently a dual source CT scanner was introduced by Siemens which uses two individual x-ray tubes that rotate simultaneously to speed up the imaging speed. Both the EBCT scanner and the SBDX tube use an electromagnetic field to steer the electron beam to different spots on the x-ray target to produce a scanning x-ray beam, very much like the design of a cathode-ray-tube. Such x-ray tubes are in general large and have a limited range of viewing angles due to the difficulty in steering the high energy electron beam.

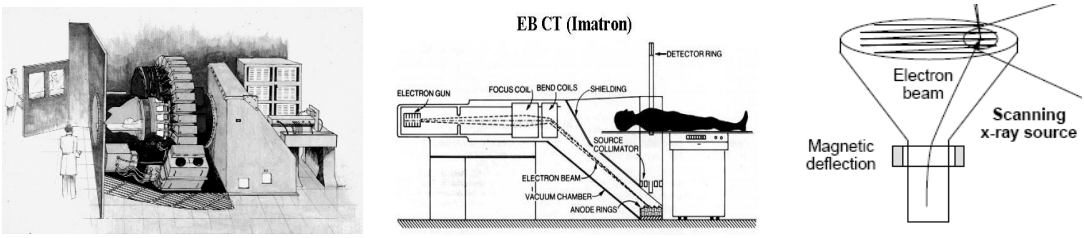

Figure 4-5: Imaging systems using spatially distributed x-ray sources.

Left: Schematic of Dynamic Spatial Reconstructor. Middle: Schematic of electro-beam CT. Right: Schematic of scanning beam digital x-ray source.

As discussed in last chapter, our MBFEX sources have excellent spatial and temporal resolution and are easy to miniaturize. The MBFEX source is ready for stationary tomosynthesis applications. The stationary digital breast tomosynthesis system can be built based on the multi-pixel field emission x-ray source.

4.2 Compact Stationary DBT System

The nine-beam system introduced in last chapter is capable of breast tomosynthesis imaging. The whole imaging system is composed by the nine-beam x-ray source, an area x-ray detector, and a computer to synchronize the x-ray source and the detector and to save the projection images. The system schematic and imaging results are shown in Figure 4-6.

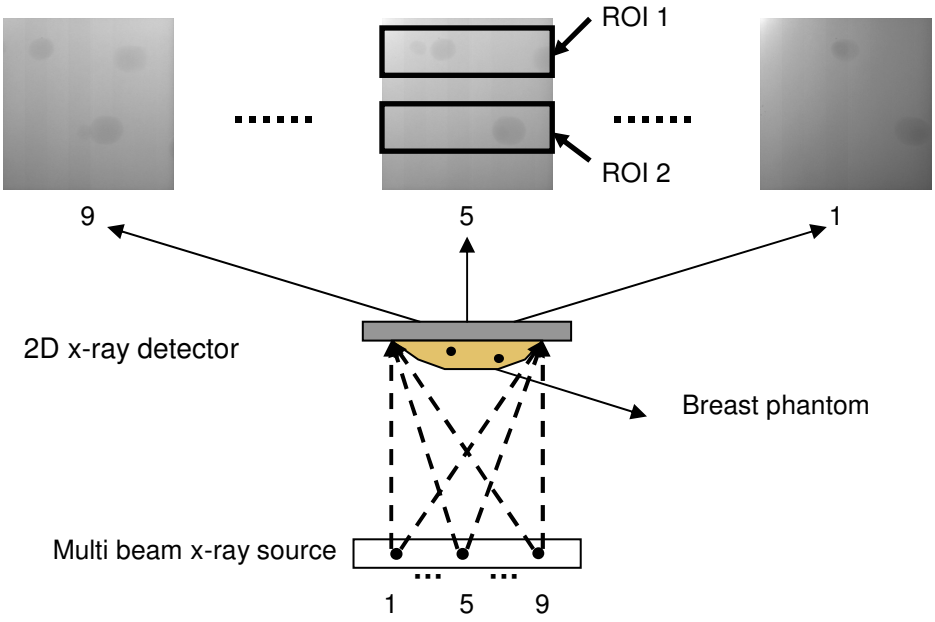

Figure 4-6: Schematic of the compact DBT system and imaging results.

A full size stereotatic needle biopsy tissue equivalent breast phantom with masses and micro-calcifications is imaged using this system. Due to the 5-cm FOV of the detector, only a portion of the phantom is imaged. The nine x-ray sources are 1.14cm apart and the source-to-detector distance is 19.3cm. The angle coverage is about 25 degrees. An iterative

reconstruction technique based on the ordered subsets convex (OSC) algorithm (Maximum Likelihood) was applied to resolve slices at different depths. 200 pixels in the z-direction were extracted from the raw data to form nine projection images of dimension 1032x200 and the reconstruction was done using a grid of dimension 50x1032x100 with non-cubic voxels of size 1mm x 0.1mm x 0.1mm.

Two regions of interest illustrated in Figure 4-6 with overlapping masses are reconstructed. The reconstructed results (Figure 4-7) clearly show that three masses are located at 1.0, 1.5, and 2.5cm in ROI 1, while other two masses are located at 1.0 and 2.5cm in ROI 2. It is of interest that the two masses in ROI 2 overlap in the conventional projection image (refer to Figure 4-6), but are well separated in the reconstructed slice images.

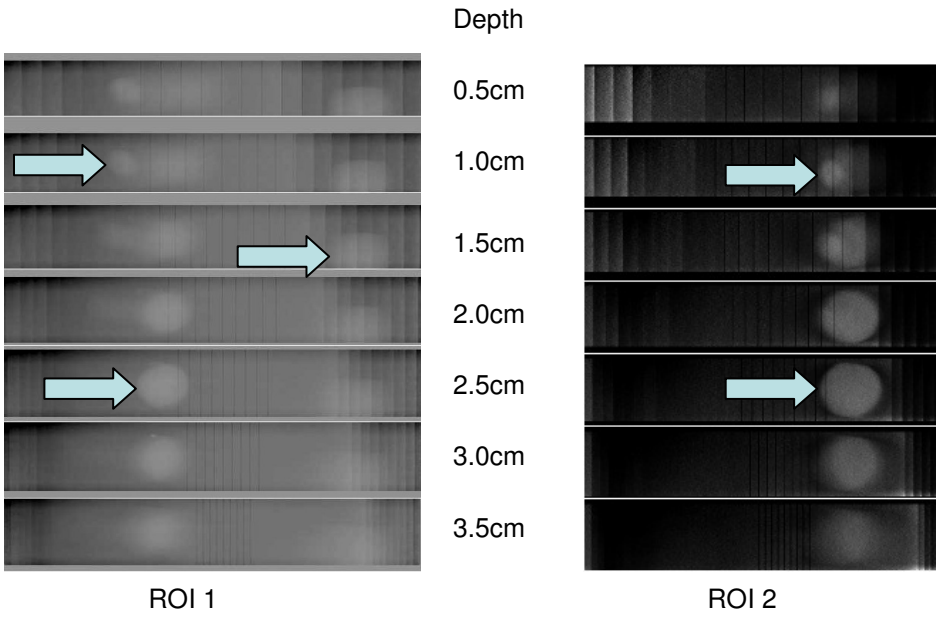

Figure 4-7: Reconstructed slice images of two regions of interest.

Although the preliminary result showed great potential, there is still room for improvement. The geometry of the system is compact compared to regular mammography devices. More importantly, the field of view can not cover the whole breast. A full scale system using the CNT x-ray source array is needed in order to obtain fair comparison with other prototype systems.

4.3 Argus – System Design

4.3.1 System Overview

The Argus system is designed to be a stationary full field digital breast tomosynthesis system based on CNT field emission x-ray source array. The whole system is composed by a 25-pixel x-ray source array based on CNT, a flat panel x-ray detector, and a work station to control the detector and the x-ray source. The system geometry is comparable to regular mammography devices. The schematic of the system geometry is shown in Figure 4-8. The flat panel detector is Varian Paxscan 2520. The field of view is 19.5cm by 24.4cm, which ensures the capability of full field mammography. Under normal mode, the pixel pitch is 127μm and the readout time is 0.128s. In binning mode, the pixel pitch is 254μm and as a result the readout time is shortened to 0.032s. The distance between the phantom and the x-

ray source is chosen to be 64.52cm, which is comparable to other regular mammography devices. All x-ray pixels are placed linearly to reduce system complexity. The even-angle distribution is adapted, and the increment is set at 2 degrees which gives 48 degrees total angle coverage. In such a design, the distance between the nearest x-ray pixels varies from 2.25cm to 2.66cm, and the span of the x-ray source array is 57.45cm. The designed power output is 10mA per x-ray pixel. By eliminating the gantry rotation, the total imaging time is less than 9 seconds with a total x-ray flux of 80mAs and the detector is operated at 2 by 2 binning mode.

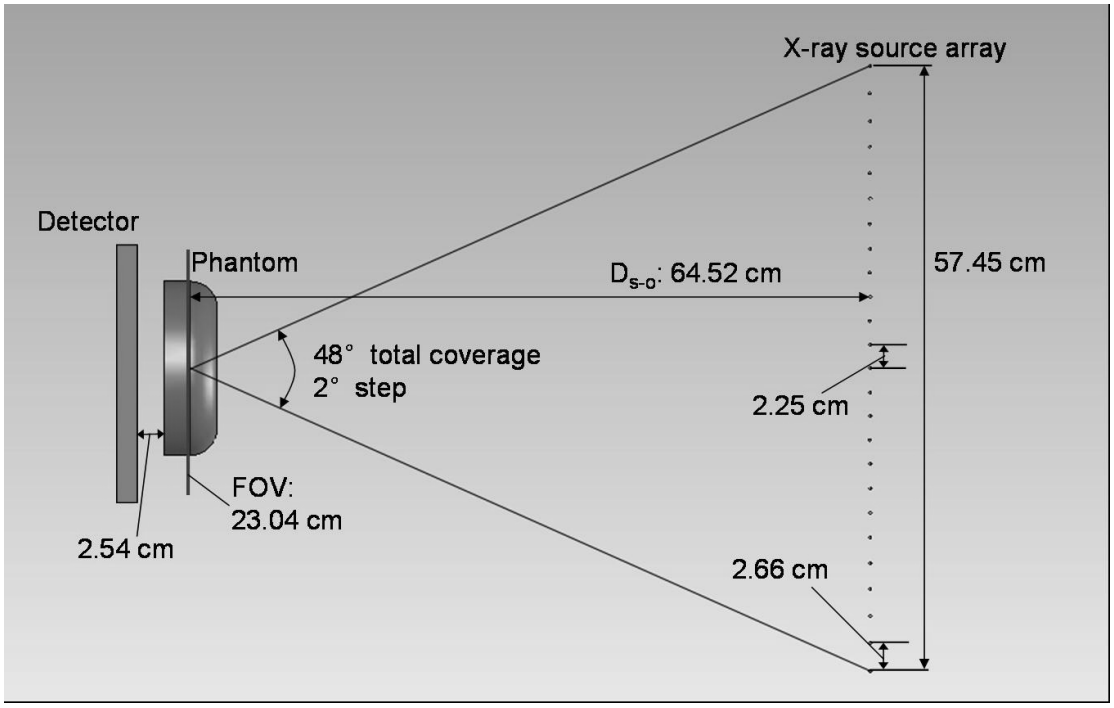

Figure 4-8: Schematic of system geometry of the Argus system.

4.3.2 X-ray Source Design

The key component of the Argus system is the 25-pixel x-ray source array. For easier fabrication and installation, the linear array design is chosen. The x-ray source is composed by two parts: the x-ray chamber and the in-chamber electronics. The CAD drawings of these two components are shown in Figure 4-9. The customized square x-ray chamber is fabricated by MDC Vacuum Inc. There are 25 1/2"-diameter holes on the front wall of the chamber to serve as x-ray windows. The positions are pre-determined by the system geometry. The iso-center of the system (also center of the breast phantom), the center of the x-ray window, and the corresponding x-ray focal spot are on a straight line. Foils made of low Z material, such as beryllium, are commonly used as x-ray windows. However, we chose molybdenum foils (30μm in thickness) for Argus, because they can function as x-ray filter (molybdenum target and filter are used widely in mammography to gain optimal spectra) as well as vacuum seals. The ports on the chamber are used for electronic connections.

The 25 identical x-ray units are mounted on a base at pre-determined positions so that the effective x-ray focal spots are at positions illustrated in Figure 4-8. The x-ray components are tilted towards the common iso-center. In other words, the line connecting the iso-center and the effective focal spot is also the central x-ray beam.

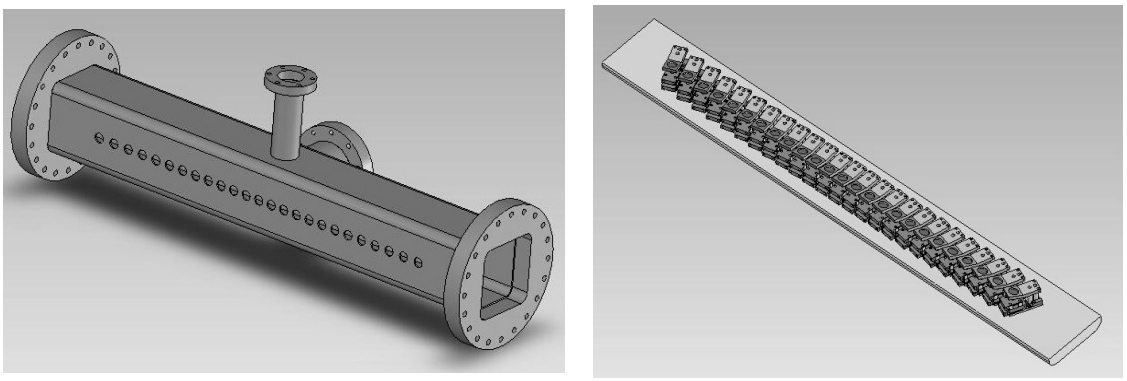

Figure 4-9: CAD drawing of x-ray source array.

Left: customized vacuum chamber with 25 x-ray windows (shown as holes). Right: 25 identical x-ray units on the base.

The detailed structure of the x-ray generation unit is shown in Figure 4-10. The cathodes are fabricated on Si wafer with a 0.72mm by 2.5mm elliptical deposition area of CNT. Tungsten mesh (100-mesh) is used as the gate to extract the electrons from the cathode. The diameter of the tungsten wire is 0.001", so the opening of the mesh is 81% of the total area. A piece of mica with 150-μm thickness is place between the cathode and the gate as the spacer. This design also includes two focusing electrodes of Einzel-type lenses[9]. Molybdenum is chosen to be the target material for optimal spectrum. The molybdenum is mounted on a copper supporting part for better heat dissipation. The take-off angle is 16 degrees. All of the gate, focusing 1, focusing 2, and anode electrodes are connected using metal wire. Each cathode has its own connection for individual control.

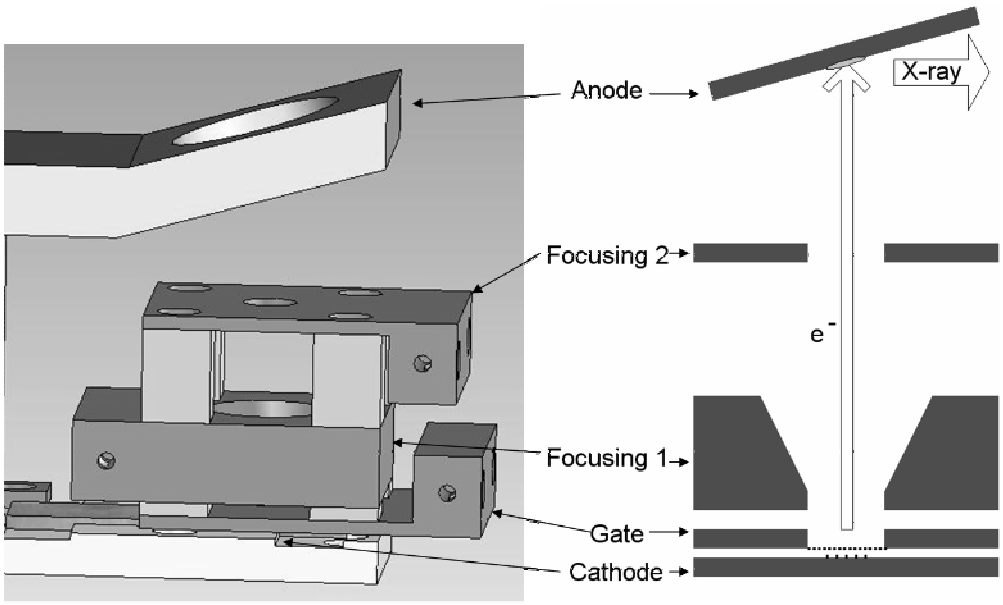

Figure 4-10: CAD drawing of the x-ray source.

4.3.3 System Control Unit and Imaging Software

Argus system requires accurate timing control and synchronization of the detector and the 25 x-ray sources. This is achieved by using a control circuit along with a host computer and an FPGA (field-programmable gate array) data acquisition board (model: NI PCI-7830R).

The timing control circuit (Figure 4-11) is essentially same as the one for the compact 9-beam system. The voltage rating of the MOSFETs (STMicroelectronics, model: STP4N150) in this circuit is 1500V. The gate, focusing 1, focusing 2, and anode electrodes are maintained at constant potentials during imaging acquisition. The drains (D), gates (G),

and sources (S) of 25 MOSFETs are connected to 25 cathodes, 25 TTL trigger signals (provided by the DAQ board), and common ground, respectively. When the TTL trigger signal is at low state, the conduction channel between the source and the drain is closed. This causes the CNT cathode potential floating relative to the common ground, and no electron is emitted from the CNT cathode, therefore no x-ray radiation is generated. When the TTL trigger signal is at high state, the cathode is grounded because of the opened conduction channel. As a result, electrons can be extracted by the electrical filed between gate electrode and cathode, and x-ray radiation is produced. The delay time (between switching of the TTL signal and the conduction channel) of the MOSFET is 35-45 ns, which is negligible considering the tens of milliseconds x-ray exposure period. Although the rating of the MOSFET is 1500V, up to 2200V voltages can be applied on the gate. The reason is that when the cathode voltage is floating, its value is typically less than the gate voltage.

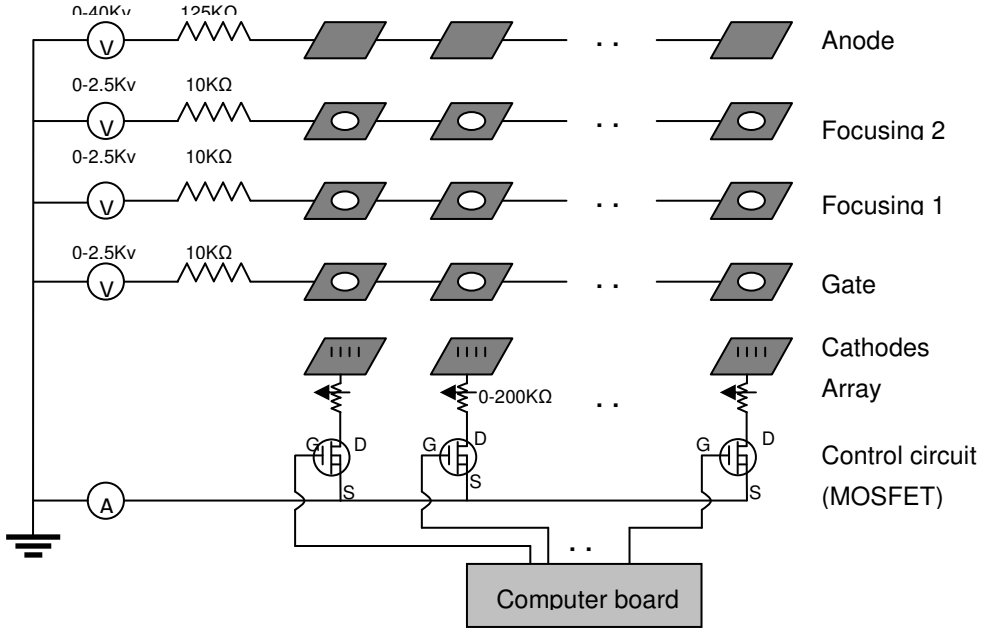

Figure 4-11: The schematic of the timing control circuit.

In user synchronization mode, the x-ray detector (Varian Medical System, PaxScan 2520) requires a continuous TTL signal from the User Sync line. As illustrated in the timing diagram of Figure 4-12, a rising edge of the TTL signal immediately triggers a frame acquisition. The readout time T_r, the period to acquire a whole frame, depends on the acquisition mode. For normal and 2 by 2 binning fluoroscopy modes, the readout time is 128ms and 32ms, respectively. After acquiring a frame, the detector waits until the next rising edge from the User Sync line to start next frame acquisition. The time between the end of a frame acquisition and the beginning of the next frame acquisition is defined as integration window T_{int}. The readout time T_r and the integration time T_{int} constitute one

imaging cycle. In fluoroscopy imaging, x-ray should be turned on within the integration window T_{int} only to reduce artifacts.

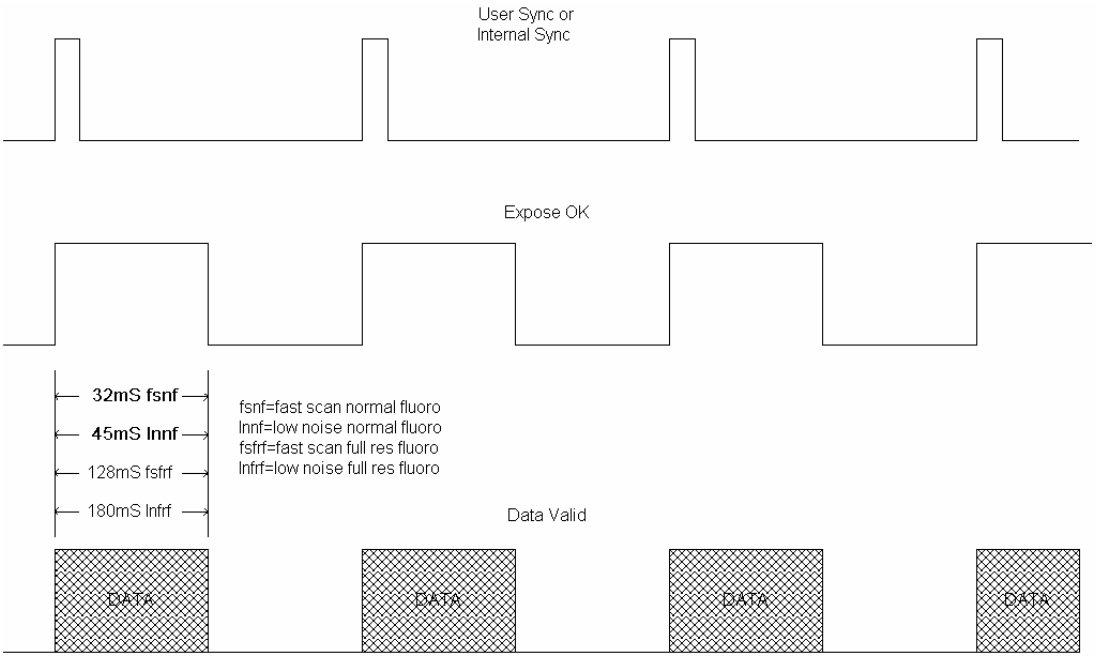

Figure 4-12: Timing diagram of Varian Paxscan 2520 detector.

Source: Paxacan user's manual.

In Argus system, all the trigger signals for the 25 x-ray pixels and the detector are provided by the NI PCI-7830R DAQ board, a user-reconfigurable FPGA (Field Programmable Gated Array) device. This DAQ board can send up to 56 TTL signals simultaneously with 1μs resolution. As shown in Figure 4-13, in one imaging sequence, 26 continuous TTL trigger signals are sent to the detector trigger line and the gates of the 25 MOSFETs. The detector trigger signal is continuous square wave whose frequency is determined by $1/(T_r + T_{int})$, where T_r is the detector readout time and T_{int} is the detector integration window. Each x-ray pixel trigger signal contains only one pulse with the same

width (denoted as T_{exp}), while the pulse T_{exp} of the ith pixel trigger exactly matches the integration window T_{int} of the ith cycle. The total scan time is simply 25*(T_r + T_{int}). If the total dose is 80mAs and the output of the x-ray sources is 10mA (design value), the total imaging time is 8.8s and 11.2s for normal mode and 2 by 2 binning mode, respectively.

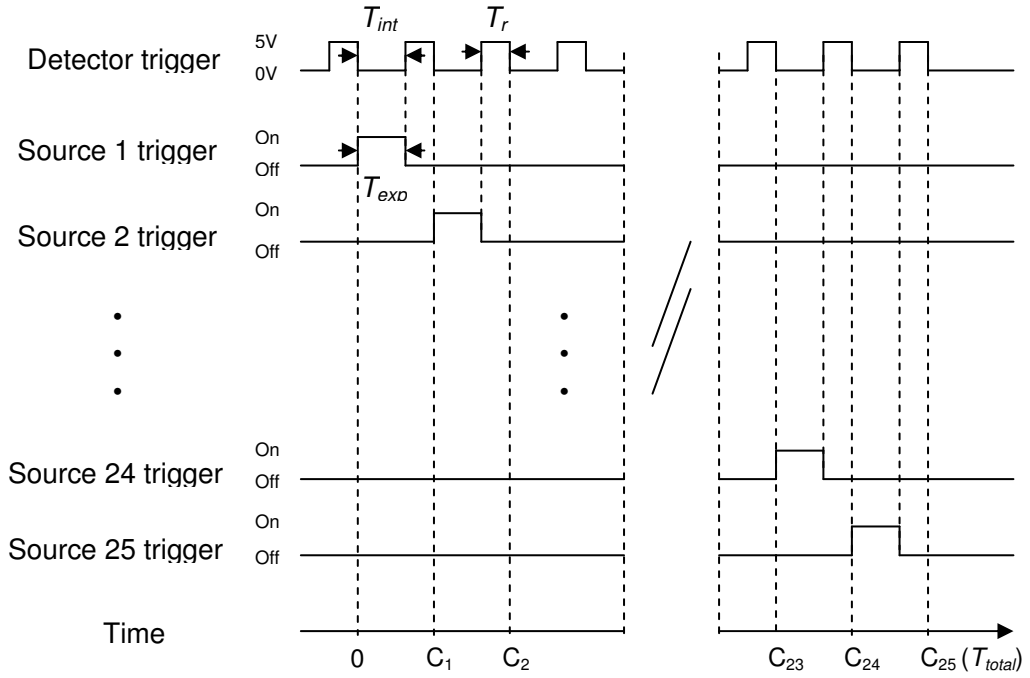

Figure 4-13: Imaging timing diagram of Argus system.

Customized imaging software is developed using LabView program for the control unit and x-ray detector. The screen shot of the software is shown in Figure 4-14. The software triggers both the x-ray sources and the detector, and saves the x-ray images in hard drive. The exposure time of each x-ray source can be adjusted. Currently, the software is designed for sequential imaging protocol.

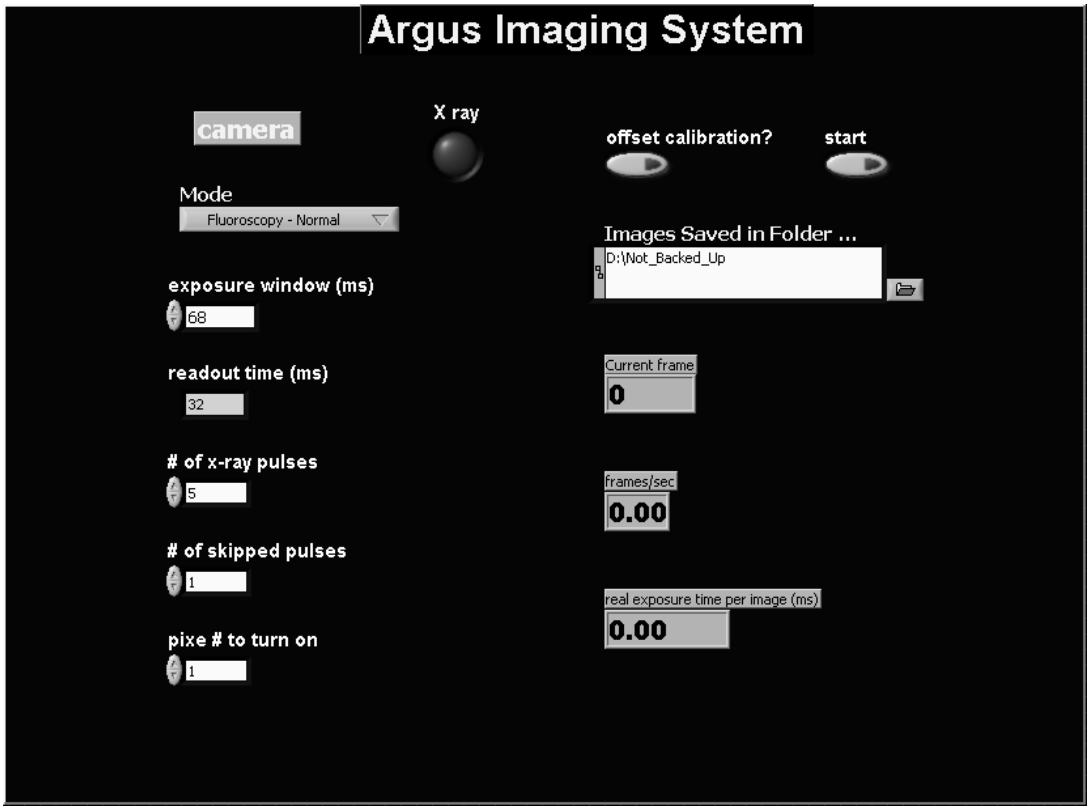

Figure 4-14: Screen shot of the imaging software.

4.3.4 Comparison with Other DBT Systems

Thanks to the unique stationary design, Argus system is superior in several aspects comparing to the conventional DBT systems with rotating gantry. The detailed comparisons are listed in Table 4-1. As no commercial DBT systems are available up to date, the specifications of others systems are from recent scientific publications.

Table 4-1: Comparison between Argus and conventional DBT systems.

	UNC: Argus	GE: Senographe 2000D	Siemens: Mammomat Novation	Hologic: Selenia
kVp, mA	~30kVp, 10mA	25-30kVp, ~130mA	~28kVp, ~180mA	24-39kVp, ~100mA
Focal spot size	200μm	300μm+blur*	300μm+blur*	300μm+blur*
Target/filter	Mo/Mo	Mo/Mo, Rh/Rh	W/Rh	(Mo, W)/(Rh, Al)
Angular coverage	48 degrees	50 degrees	50 degrees	30 degrees
View numbers	25	11	25/49	11
Gantry motion	Stationary	Step and shoot	Continuous rotation	Continuous rotation
Flat-panel Detector	A-silicon	Cs:I a-silicon	Direct converter	Direct converter
Detector size	19.5 x 24.4 cm	18.00 x 23.04 cm	23.9 x 30.5 cm	24 x 29 cm
Pixel pitch	127μm	100μm	85μm	140μm
Readout time	0.128s/0.032s	0.3s	0.6s/0.3s	0.6s
Integration time	0.32s	0.4s	0.2s	1.0s
Exposure time	Same as integration time	0.1s	~0.03s	0.073s
Scan time**	11.2s for 25 views	7s for 11 views	20s for 25 views	18s for 11 views
Total dose	80mAs	45-143mAs	80-133.4mAs	80-160mAs
Reconstruction method	OSC: ordered subsets convex (maximum likelihood)	ML-EM: maximum likelihood expectation maximization	FBP: filtered back projection	FBP: filtered back projection

*: Additional focal spot blur due to the gantry movement during exposure.

**: Scan time = (view number) x (cycle time); cycle time = (readout time) + (integration time).

- The focal spot size of Argus system is 200μm while the values of other systems are larger than 300μm (the enlargement due to gantry movement is about 1mm).
- Stationary design gives less gantry vibration by eliminating the mechanical movement.
- The exposure time matches the detector integration window. In other words, the utilization of the x-ray power and imaging time is more efficient.
- The total scan time (8.8s in binning mode and 11.2s in full-resolution mode, 25 viewing angles) is the shortest among all systems under similar imaging conditions.

4.4 Argus – System Assembly and Test

4.4.1 System Assembly

The Argus system was assembled following the design. The 25 x-ray units are mounted on the base as illustrated in Figure 4-15. All parts are well polished and cleaned before assembly. Mechanical and electrical polishing procedures are applied on the metal parts. The metal parts are also annealed at 400˚C for four hours. The x-ray source array was then put into the customized chamber. The anode is connected through a 30keV feed-through. The gate and two focusing electrodes are connected using BNC feed-throughs. A multi-pin feed-through is used to connect the 25 cathodes. A mechanical pump and a turbo pump are used to maintain the vacuum of the x-ray chamber. The chamber was baked at 70˚C to achieve better vacuum level (the maximum baking temperature of torr seal epoxy is 120˚C). At stable stage, the vacuum of the x-ray chamber is about $1X10^{-7}$ torr.

Figure 4-15: Picture of 25 x-ray units on the mounting base.

A customized stand is machined to hold the x-ray chamber. The x-ray detector is mounted to a translation stage which has two axes parallel to the detector surface. The sample stage is attached to the detector holder. A picture of the assembled Argus system is shown in Figure 4-16.

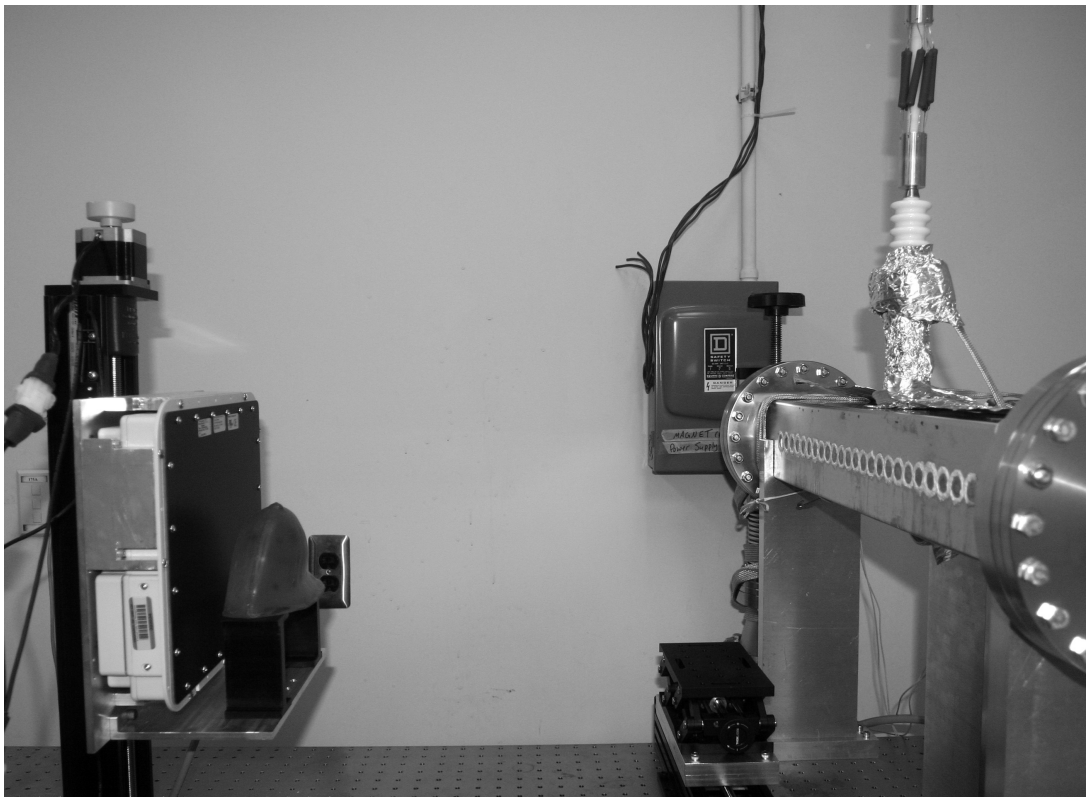

Figure 4-16: Picture of the assembled Argus system.

4.4.2 Focal Spot Calibration

As designed, the x-ray source array should have consistent 200μm focal spot size. For the resolution of the projection x-ray images is mostly determined by the focal spot size, and

the reconstruction tomosynthesis images requires all the projection images, uniform x-ray focal spot size is the ideal case and produces the best reconstruction images. The focal spot size value was measured following the European standard EN12543-5[61]. A customized cross wire phantom is used to measure the focal spot size along two directions simultaneously. The schematic of the phantom and a typical projection image are illustrated in Figure 4-17. Due to the limitation of the current feed-through, gate voltage can not exceed 2000V. At this level, the current of the x-ray source can not reach 10mA, the designed value. The focal spot measurement was done at 0.5mA tube current.

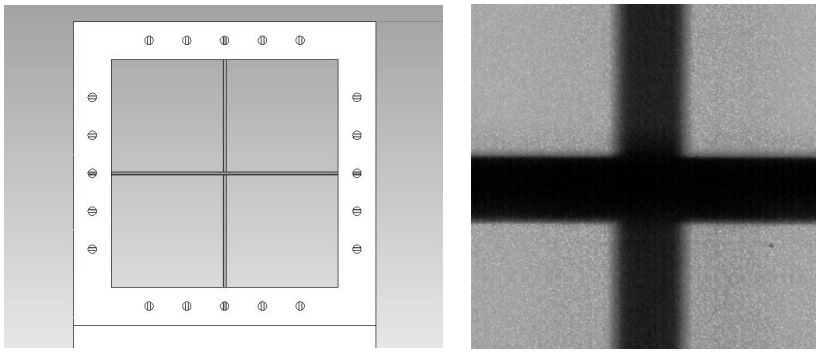

Figure 4-17: Focal spot size measurement.

Left: cross wire phantom for focal spot size measurement. Right: a typical x-ray image of the phantom.

As the focal spot size depends on the two focusing electrodes, the focusing voltages were first optimized. It was found that the smallest focal spot size is achieved when focusing1 = 400V and focusing2 = 1400V. The gate voltage has no visible effect on the focal spot size. The typical focal spot size is 0.20mm by 0.18mm. Measurements from different x-ray sources yield consistent results. As designed, the focal spot along the two directions

should have the same value. The deviation from the design could rise from the fact that the design is based on the simulation results which uses parallel electrodes while the anode take off angle is 16 degrees in the real setup.

4.4.3 Spectrum Calibration

The spectrum of the x-ray source was measured at 28keV using a Si-pin photodiode detector from Amptek (XR-100CR and MCA-8000A). The detector was place in the field of view, and the spectra at different positions and from different x-ray sources were measured. The results show consistent spectra as illustrated in Figure 4-18. As can be seen from the spectra, both high energy (>21keV) and low energy (<7keV) radiation is filtered by the 30μm Mo window. The copper K_α and K_β characteristic peaks are also noticeable on the spectra. The reason for this could be the dark current (the tube current from the emission of the focusing electrode, rather than from the cathode) in the preliminary test. This is confirmed by measuring the background spectrum (Figure 4-19). The copper characteristic peaks can be removed in the future by eliminating the dark current.

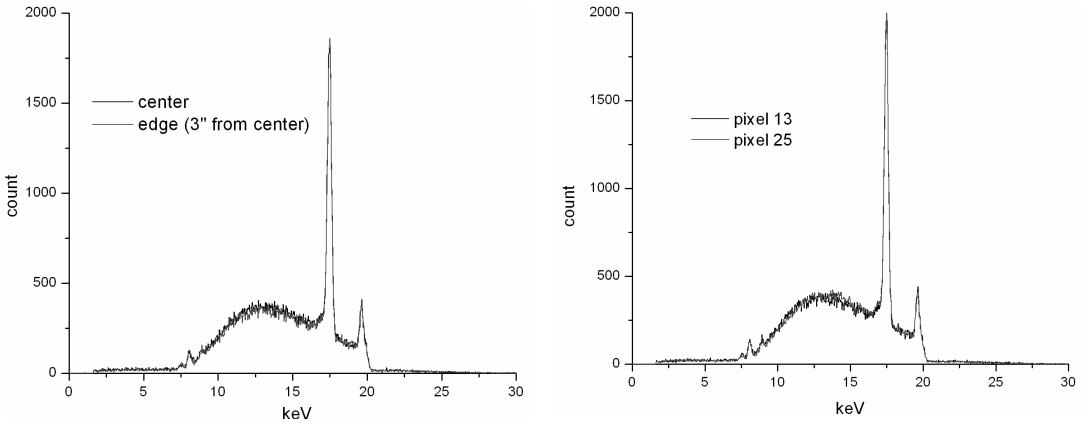

Figure 4-18: Spectra of the Argus system.

Left: spectra at the center and at the edge (3" away from the center) of the field of view. Right: spectra from pixel 13 (center x-ray source) and pixel 25 (edge x-ray source).

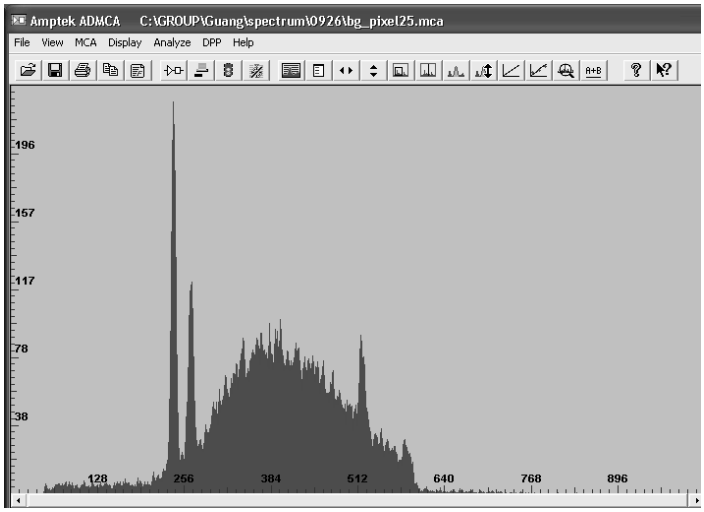

Figure 4-19: Background spectrum of Argus system.

Spectrum was measured when the anode is set at 28keV and all x-ray sources are off.

4.4.4 X-ray Flux Modulation

The x-ray flux of each x-ray source is determined by the gate voltage and the ballast resistor in the control circuit Figure 4-11. As in the Argus system, the gate voltage is the same for all sources, the flux modulation is achieved by adjusting the variable resistors. Figure 4-21 shows the I~V measurement after adjusting the resistor values of 6 x-ray sources. Up to 1500V was applied on the gate, and the maximum value of the variable resistor value is 210KΩ. Compare to the measurement with the same 100KΩ resistor, the current variation is much smaller. Using higher value resistors such as 500 KΩ can further reduce the variation.

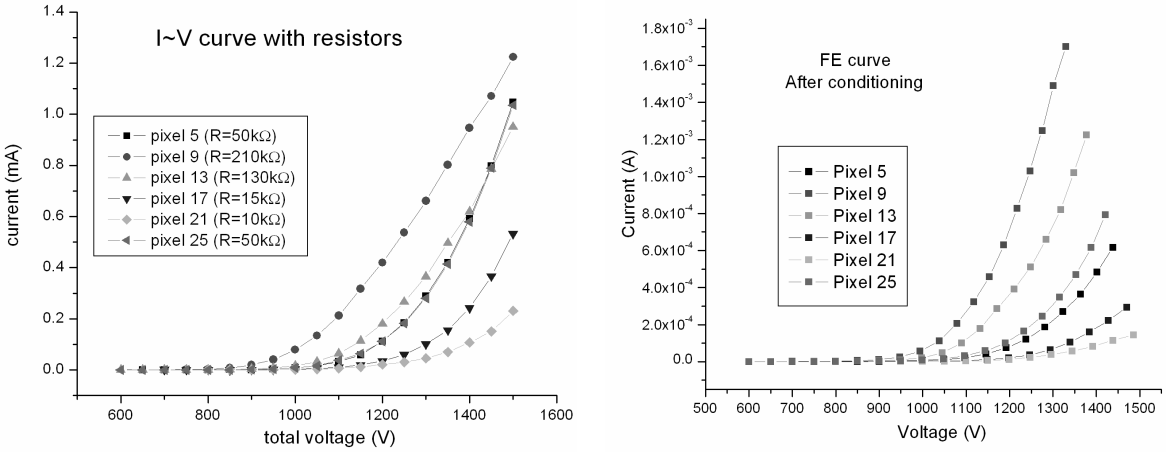

Figure 4-20: X-ray flux modulation.

Top: flux modulation of 6 x-ray sources. Bottom: I~V measurement before adjusting the resistor values.

4.4.5 Geometry Calibration

The tomosynthesis reconstruction requires precise system geometry parameters. We applied an analytic method based on identification of ellipse parameters[84] for the geometry calibration, which was first established for cone-beam CT calibration. A turntable and a two-point phantom are used in this method. There are seven parameters to describe the system: R, D, θ, φ, η, u_0, and v_0, which are defined as follow. R is the distance from the focal spot to the rotation axis. D is the shortest distance from the focal spot to the detector plane. θ, φ, and η determine the offset angles of the detector plane. u_0, and v_0 are the Cartesian coordinates of the orthogonal projection point of the x-ray focal spot onto the detector plane. This method assumes θ to be zero (detector plane is vertical). In Argus system, this condition is verified by using a level to measure the vertical angle offset of the detector.

A phantom with two point objects with known distance is rotated and imaged. These two objects should be neither on the rotation axis nor in the plane of the x-ray focal spot. Each object traces an ellipse in the detector plane (Figure 4-21). To obtain the parameters of the two ellipses, a minimum of six projection images (60-degree rotation in-between) is required. The system parameters can be further calculated based on the two ellipse curves. By using this method, the uncertainties of the system parameters are 2mm for distance measurement and 0.1 degree for angle measurement.

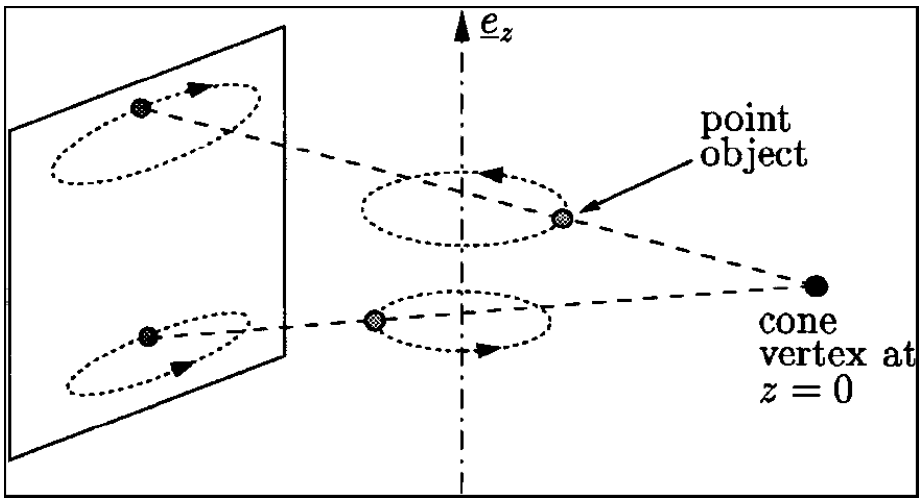

Figure 4-21: Schematic of the two-ball phantom under rotation.

Each object traces an ellipse in the detector plane.

The x-ray sources are calibrated individually as a cone beam imaging system. As Argus system does not require a rotation stage, not all parameters are needed for tomosynthesis reconstruction. Only three parameters are enough to describe the system geometry: D, u_0, and v_0. The calibration results from three representative x-ray sources are listed in Table 4-2. These numbers agree with the designed values.

Table 4-2: Geometry calibration results of three x-ray sources.

	source 5	source 13	source 17
D (cm)	69.1	69.3	69.1
u (cm)	-19.7	-0.3	9.1
v (cm)	0.8	1	1.1

4.5 Discussions

The preliminary result shows that all components of Argus work as designed. The x-ray source array can generate x-ray at 28keV. The x-ray sources can be switched and modulated through the control unit. The imaging software can trigger both the x-ray sources and the detector. The full calibration procedure has been set up. The reconstruction program has been tested using the images obtained from the compact system. However, the x-ray flux at current stage is still less than the designed value (10mA). Better cathode fabrication techniques could solve this problem in the near future.

The focal spot size of Argus system is 200μm. As many clinical experts have pointed out, the total imaging time, rather than the effective focal spot size, is the limiting factor of conventional DBT systems. If the focal spot size of Argus system is relaxed to 500μm or so, the peak radiation current can reach 50mA. In such a case, the total imaging time can be further reduced to 3 seconds. This should be the direction of the next generation of Argus system.

The stationary DBT system using x-ray source array also opens the door for many advanced techniques.

- The multiplexing technique (including frequency domain multiplexing and binary

multiplexing) can further reduces the total imaging time.

- Dual energy imaging can achieve higher temporal resolution with Argus system. Conventional dual energy imaging requires high voltage switching. The anodes of the x-ray source array can be set at different high voltages, so there is no switching delay.
- Quasi-monochromatic imaging is possible using Argus system. By using the filtered quasi-monochromatic x-ray radiation, the image quality can be improved at the same radiation dose. As the filtered radiation flux is only about 10% of the original value, the total imaging time could be longer. However, if both multiplexing technique and the quasi-monochromatic x-ray beam are applied, the total imaging time can be unchanged.

Chapter 5: Conclusion and Future Direction

Since the discovery of carbon nanotubes in 1991, the research focus has gradually shifted from material synthesis and characterization to applications and devices. Due to the unique properties, CNT has found its applications in many areas. Field emission electron source based on CNT is among the most promising ones. This novel electron source can be used in applications such as TEM electron gun, field emission display, and x-ray source.

Field emission x-ray source based on CNT has many advantages compared to the conventional thermionic x-ray source.

- The switching of the field emission x-ray source is controlled by the gate voltage. High temporal resolution up to sub micro second can be achieved.
- High spatial resolution can also be obtained by using electrostatic focusing method.
- The field emission x-ray source based on CNT can be miniaturized easily.

Because of these properties, this novel x-ray source can replace the conventional source in many applications. Both single beam and multi beam x-ray sources based on CNT have been developed. The performances of them have been tested. The single beam x-ray source

has been applied in micro-CT system. The multi beam x-ray source has been used for tomosynthesis imaging.

Argus system is the first stationary digital breast tomosynthesis imaging system. Argus system has geometry comparable to conventional mammography devices. The system has been fully assembled. The control unit, imaging software, and the calibration procedure have been developed. The preliminary test shows that Argus system functions as designed. Compared to conventional systems which require gantry rotation, Argus system has shorter imaging time, better system stability, and higher resolution. Tomosynthesis imaging is believed to the trend of digital radiography. The pioneering study of Argus could fundamentally change the medical tomosynthesis imaging systems.

Although Argus is specifically designed for breast imaging, the concept and design can be extended to other imaging systems which can take advantage of multiple x-ray sources, such as chest tomosynthesis and CT. The multi beam system also opens the door for other advanced techniques including multiplexing and dual energy imaging. More research needs to be done in the future for better understanding of these issues.

References:

1. K. K. Shung, Michael B. Smith, and B. Tsui, *Principles of Medical Imaging.* 1992, San Diego: California: Academic Press, Inc.

2. Ashcroft, N.W. and N.D. Mermin, *Solid State Physics.* 1976.

3. D.J. Helfand, *X-rays from the rest of the universe.* Physics Today, 1995. **11**: p. 58-64.

4. Pisano, E.D., M.J. Yaffe, and C.M. Kuzmiak, *Digital mammography* 2004.

5. M.H.F. Wilkins and J.T. Randall, Biochim. et Biophys. Acta, 1953. **10**: p. 192.

6. Wolbarst, A.B., *Physics of Radiology.* 1993.

7. Selman, J., *the fundamentals of x-ray and radium physics.* 1972.

8. E. Seeram, *X-ray imaging equipment*. 1985: Charles C Thomas.

9. Zejian Liu, G.Y., Yueh Z.Lee, et al., *Carbon nanotube based microfocus field emission x-ray source for microcomputed tomography.* applied physics letters, 2006. **89**(10).

10. Tavora, L.M.N., E.J. Morton, and W.B. Gilboy, *Design considerations for transmission x-ray tubes operated at diagnostic energies.* J. Phys. D: Appl. Phys., 2000. **33**: p. 2497-2507.

11. Jackson, J.D., *Classical Electrodynamics*. 3rd ed. 1998.

12. G. Margaritondo, *Introduction to Synchrotron Radiation*. 1988: Oxford University Press.

13. R. Garrett, *An introduction to synchrotron radiation*. 2004.

14. Pisano, E.D. and M.J. Yaffe, *digital mammography.* radiology, 2005. **234**(2): p. 353-362.

15. Kroto, H.W., et al., Nature, 1985. **318**: p. 162-163.

16. S. Iijima, *Helical Microtubules of Graphitic Carbon.* Nature, 1991. **354**: p. 56-58.

17. S. Iijima and T. Ichihashi, *Single-Shell Carbon Nanotubes of 1-nm Diameter.* Nature, 1993. **361**: p. 603-605.

18. D.S. Bethune, et al., *Cobalt-catalysed growth of carbon nanotubes with single-atomic-layer walls.* Nature, 1993. **363**: p. 605-607.

19. M.S. Dresselhaus, G. Dresselhaus, and P.C. Eklund, *Science of Fullerenes and Carbon Nanotubes*. 1996, New York: Academic Press.

20. Dresselhaus, M.S., G. Dresselhaus, and A. Jorio, *Unusal properties and structure of carbon nanotubes.* Annu. Rev. Mater. Res., 2004. **34**: p. 247-278.

21. Yakobson, B.I. and R.E. Smalley, *Fullerene Nanotubes: C1,000,000 and Beyond.* American Scientist, 1997. **85**: p. 324-337.

22. R. Saito, et al., *Electronic structure of chiral graphene tubules.* Applied Physics Letters, 1992. **60**(18): p. 2204-2206.

23. Mintmire, J., B.I. Dunlap, and C.T. White, *Are fullerene tubules metallic?* Phys. Rev. Lett, 1992(68): p. 631.

24. Hamada, N., S.I. Sawada, and A. Oshiyama, *New one-dimensional conductors: graphitic microtubules.* Phys. Rev. Lett, 1992(68): p. 1579.

25. Filho, A.G.S., et al., *Stokes and anti-stokes Raman spectra of small diameter isolated carbon nanotubes.* Phys. Rev. B, 2004. **69**: p. 1154.

26. Chico, L., et al., *Pure carbon nanoscale devices: nanotube heterojunctions.* Phys. Rev. Lett., 1996. **76**: p. 971.

27. Lu, J.P., *Elastic Properties of Single and Multilayered Nanotubes.* Phys. Rev. Lett., 1997. **79**(7): p. 1297-1300.

28. Treacy, M.M., T.W. Ebbesen, and J.M. Gibson, *Exceptionally high Young's modulus observed for individual carbon nanotubes.* Nature, 1996. **381**: p. 678-680.

29. Wong, E.W., P.E. Sheehan, and C.M. Lieber, *Nanobeam Mechanics: Elasticity, Strength and Toughness of Nanorods and Nanotubes.* Science, 1997. **277**(26): p. 1971-1975.

30. Falvo, M.R., et al., *Bending and Buckling of Carbon Nanotubes under Large Strain.* Nature, 1997. **389**: p. 582-584.

31. Hone, J. and e. al., *Thermal conduciticity of single-walled carbon nanotubes.* Physical Review B, 1999. **59**: p. 2514-2516.

32. Meyyappan, M. and e. al., *Carbon Nanotubes: Science and Applications.* 2005.

33. P.L. McEuen, *Single wall carbon nanotubes.* Physics World, 2000: p. 31-36.

34. Modinos, A., *Field, Thermionic and Secondary Electronemission Spectroscopy*. 1984: Plenum Pub Corp.

35. Bermond, J.M., et al., *Numerical data and experimental proof of the unified theory of electron emission.* Surf. Sci., 1974. **42**: p. 306-323.

36. C.A. Spindt, et al., *Physical properties of thin-film field emission cathodes with molybdenum cones.* Journal of Applied Physics, 1976: p. 5248-5263.

37. P. Schagen, *Alternatives to thermionic emission.* Brit. J. Appl. Phys., 1965. **16**: p. 293-303.

38. Jonge, N.d., et al., *High brightness electron beam from a multi-walled carbon nanotube.* Nature, 2002. **420**: p. 393.

39. J.H. Hafner, C.L.C., and C.M. Lieber, Nature, 1999. **398**: p. 761.

40. J. G. Wen, et al., *Growth and characterization of aligned carbon nanotubes from patterned nickel nanodots and uniform thin films.* Journal of Materials Research, 2001. **16**: p. 3246-3253.

41. Cheung, C.L., et al., Appl. Phys. Lett., 2000. **76**: p. 3136.

42. S.S. Wong, et al., Appl. Phys. Lett., 1998. **73**: p. 3465.

43. S. Akita, et al., *Carbon nanotube tips for a scanning robe microscope: their fabrication and properties.* J. Phys. D: Appl. Phys., 1999. **32**: p. 1044.

44. Milas, M., et al., in *Structural and Electronic Properties of Molecular Nanostructures*. 2002, EBSCO. p. 614.

45. T.B. Jones, *Electromechanics of Particles*. 1995, Cambridge: Cambridge Univ Press.

46. O. D. Velev and E.W. Kaler, *In Situ Assembly of Colloidal Particles into Miniaturized Biosensors.* Langmuir, 1999. **15**(11): p. 3693.

47. W. B. Choi, et al., *Field emission from silicon and molybdenum tips coated with diamond powder by dielectrophoresis.* Appl. Phys. Lett., 1996. **68**: p. 720.

48. J. Tang, et al., *Assembly of 1D nanostructures into sub-micron diameter fibrils with controlled and variable length by dielectrophoresis.* Adv. Mater., 2003. **15**(15): p. 1352.

49. O. Zhou, et al., *Materials Science of Carbon Nanotubes: Fabrication, Integration, and Properties of Macroscopic Structures of Carbon Nanotubes.* Acc. Chem. Res, 2002. **35**: p. 1045-1053.

50. J. Liu, et al., *Fullerene Pipes.* Science, 1998. **280**: p. 1253-1256.

51. C. Bower, et al., *Nucleation and growth of carbon nanotubes by microwave plasma chemical vapor deposition.* Appl. Phys. Lett., 2000. **77**(17).

52. Zhao, G., et al., *Field Emission of electrons from a Cs-doped single carbon nanotube of known chiar indices.* Applied physics letters, 2006. **89**: p. 263113.

53. M. Bissonnette, et al., *Digital breast tomosynthesis using an amorphous selenium flat panel detector.* Proceedings of SPIE, 2005. **5745**: p. 529.

54. Yue, G.Z., et al., *Generation of continuous and pulsed diagnostic imaging X-ray radiation using a carbon-nanotube-based field-emission cathode.* Applied physics letters, 2002. **81**(2): p. 355.

55. Paulus, M.J., et al., Neoplasia, 2000. **2**: p. 62.

56. Ritman, E.L., Annu. Rev. Biomed. Eng., 2004. **6**: p. 185.

57. Ehrenberg, W. and W.E. Spear, Proc. Phys. Soc. London, Sect. B, 1951. **64**: p. 67.

58. Barr, A.E.d. and I. macArthur, Br. J. Appl. Phys., 1950. **1**: p. 305.

59. Arndt, U.W., J.V.P. Long, and P. Cuncumb, J. Appl. Crystallogr., 1998. **31**: p. 936.

60. Riddle, G.H.N., J. Vac. Sci. Technol., 1978. **15**: p. 857.

61. *European Committee for Standardization: EN 12543-5, E. Brussels*. 1999.

62. Flynn, M.J., et al., Nucl. Instrum. Methodes Phys. Res. A, 1994. **353**: p. 312.

63. Badea, C., L.W. hedlund, and G.A. Johnson, Med. Phys., 2004. **31**: p. 3325.

64. W.R. Hendee and E.R. Ritenour, *Medical Imaging Physics*. 4th ed. 2002, New York: Wiley-Liss.

65. J.T. Dobbins III and D.J. Godfrey, *Digital x-ray tomosynthesis: current state of the art and clinical potential.* Phys. Med. Biol., 2003. **48**: p. R65-R106.

66. D.P. Boyd and C. Haugland, *Recent progress in electron beam tomography.* Med. Imag. Tech., 1993. **11**: p. 578-585.

67. P. Bowles, E. Duff, and D.D. Thayer, *Method and apparatus for imaging obscured areas of a test object*. 1997: U.S.A.

68. B.D. Baker, et al., *Automated laminography system for inspection of electronics*. 1990: U.S.A.

69. H.T. Morgan, *Rotating anode x-ray tube with multiple simultaneously emitting focal spots*. 2000: U.S.A.

70. Robb, R.A., et al., *High-speed three dimensional x-ray computed tomography: The Dynamic Spatial Reconstructor.* Proceedings of the IEEE, 1983. **71**(3): p. 308-319.

71. A.V. Oppenheim, A.S. Willsky, and I.T. Young, *Signals and systems*. 1983, Englewood Cliffs: Prentice-Hall.

72. P.J. Treado and M.D. Morris, *The Hadamard transform in chemical analysis and instrumentation.* Anal. Chem. , 1989. **61**: p. 732A.

73. R.N. Zare, F.M. Fernandez, and J.R. Kimmel, *Hadamard transform time-of-flight mass spectrometry: more signal, more of the time.* Angew. Chem. Int. Ed. Engl, 2003. **42**(1): p. 30.

74. R. W. Chang, *Synthesis of band-limited orthogonal signals for multichannel data transmission.* Bell Syst. Tech. J., 1966. **46**: p. 1775-1796.

75. Landis, S., et al., *cancer statistics, 1998.* CA Cancer J Clin, 1998. **48**: p. 6-29.

76. Kopans, D.B., *brease imaging*. 2nd ed. 1997, New York: Lippincott Williams and Wilkins.

77. Feig, S.A., *decreased breast cancer mortality through mammographic screening: results of clinical trials.* radiology, 1988. **167**: p. 659-665.

78. Pisano, E.D. and et al., *Diagnostic performance of digital versus film mammography for breast cancer screening.* N. Engl. J. Med., 2005. **353**: p. 1773-1783.

79. Wu, T., et al., *Tomographic mammography using a limited number of low-dose cone-beam projection images.* Med. Phys., 2003. **30**(3): p. 365-380.

80. Ren, B., et al., *Design and performance of the prototype full field breast tomosynthesis system with selenium based flat panel detector.* proceedings of SPIE, 2005. **5745**: p. 550-561.

81. M.J. Lipton, et al., *Cardiac imaging with a high-speed Cine-CT Scanner: preliminary results.* Radiology, 1984. **152**(3): p. 579-82.

82. M.A. Speidel, et al., *scanning-beam digital x-ray (SBDX) technology for interventional and diagnostic cardiac angiography.* Medical Physics, 2006. **33**(8): p. 2714.

83. T.G. Schmidt, et al., *A prototype table-top inverse-geometry volumetic CT system.* Medical Physics, 2006. **33**(6): p. 1867.

84. Noo, F., et al., *Analytic method based on identification of ellipse parameters for scanner calibration in cone-beam tomography.* Phys. Med. Biol., 2000. **45**: p. 3489-3508.